DESIGN OF A UNIVERSAL INDUCTIVE CHARGING SYSTEM FOR ELECTRIC VEHICLES

A Dissertation
Presented to
The Academic Faculty

by

Nan Liu

In Partial Fulfillment
of the Requirements for the Degree
Doctor of Philosophy in the
School of Electrical and Computer Engineering

Georgia Institute of Technology
May 2016

DESIGN OF A UNIVERSAL INDUCTIVE CHARGING SYSTEM FOR ELECTRIC VEHICLES

Approved by:

Dr. Thomas G. Habetler, Advisor
School of Electrical and Computer Engineering
Georgia Institute of Technology

Dr. Maryam Saeedifard
School of Electrical and Computer Engineering
Georgia Institute of Technology

Dr. J. Rhett Mayor
School of Mechanical Engineering
Georgia Institute of Technology

Dr. Ronald G. Harley
School of Electrical and Computer Engineering
Georgia Institute of Technology

Dr. Lukas Graber
School of Electrical and Computer Engineering
Georgia Institute of Technology

Date Approved: 11/16/2015

To

my father, Lenian Liu,

my mother, Zhanmin Liu,

and

firefighters died in Tianjin explosions, on Aug. 12, 2015.

ACKNOWLEDGEMENTS

The doctoral study at Georgia Tech is a long way. In the past years, I did experience and learn a lot. I cannot imagine whether I could finish the dissertation without inspiration and encouragement from my advisor, friends, partners, and those who helped me.

First of all, I would like to extend my most sincere thanks to my advisor, Dr. Thomas G. Habetler. I came to Georgia Tech as a Master Student. At that time, I could never imagine there was a chance for me to pursue a Ph.D. degree with him. It is an honor to be supervised by such a scholar with high reputation. From then on, Dr. Habetler has given me a lot of instructions and encouragements, especially when I was struggling in some personal issues. His optimism, patience, motivation, and immense knowledge, has been inspiring me in the past 4 years. His patient and careful guidance on solving problems, writing reports and oral communicating with profession rewards my entire research life. Once I was asked what the most valuable thing I learned during Ph.D. research, I said "how to do research and how to solve problems in research". That's the most important skill I acquired from Dr. Habetler. I am deeply grateful for his guidance and support during my Ph. D. life.

I would also like to extend my sincere gratitude to Dr. Ronald G. Harley, Dr. Maryam Saeedifard, Dr. Lukas Graber, and Dr. J. Rhett Mayor for serving as my dissertation committee members. I really appreciate their help in reviewing the drafts and providing my ideas of improvements. They definitely help broaden my horizon and enrich my knowledge.

TABLE OF CONTENTS

LIST OF TABLES

LIST OF FIGURES

xvii

LIST OF ABBREVIATIONS

IPT	Inductive Power Transfer
UIC	Universal Inductive Charger
EV	Electric Vehicle
PFC	Power Factor Correction
S-connected LC	Series-connected LC
P-connected LC	Parallel-connected LC
SPWM	Sinusoidal Pulse Width Modulation
ZVS	Zero Voltage Switching
ZCS	Zero Current Switching
BMS	Battery Management System
SP	Square Pad
CP	Circular Pad
MCU	Microcontroller Unit
BPP	Bipolar Pad
DDQP	Double-D Quadrature Pad

SUMMARY

A promising method for charging batteries of electric vehicles (EV) is inductive power transfer (IPT), also known as inductive charging. IPT, a convenient, safe, and aesthetic method of charging EVs, inductively transfers high-frequency AC power in the transmitting pad, or coil, to the receiving pad, or coil. However, the application of IPT entails several practical limitations. For example, misalignment of the coils and varied charging distance (air gap) between the coils change the magnetic coupling effect between the transmitting and receiving coils. As a result, system stability decreases because the electrical characteristics in different charging cycles vary. Previous research has rarely proposed an adaptive and effective method to solve the problems of varied coupling. Many EV models, however, exist on the market and more will be released in the future. A universal charger suitable for charging various models of EVs will have broad applications, especially in public charging areas. Therefore, we must design a universal inductive charger capable of providing stable charging voltage to various loads, even with influences by varied magnetic coupling. Also important is the design standard of on-board chargers used for universal inductive charging. The design schemes of the universal inductive charger and on-board chargers can be used as references for the future development of the entire EV inductive charging system.

The objective of this thesis is to design a universal IPT system that provides stable and high-efficiency charging power to various models of EVs (Levels 1 and 2 charging), even with the influences by varied magnetic coupling and various designs of EVs (e.g., containing different receiving pads and secondary LC resonant circuits). The proposed

system consists of two main parts. One is a universal inductive charger on the primary side, generating AC power in the transmitting pad, or coil. Another part, an on-board charger on the secondary side, receives power from the primary side by the receiving pad and provides nominal charging voltage and current (V&I) to batteries.

The universal inductive charger (UIC) in the primary side forms the basis of the system. The electrical characteristics of the UIC and relevant control strategy should adapt to varied coupling effects and varied load conditions. In all possible conditions, the proposed charging must be efficient and stable. To achieve universality, high efficiency, and stability, the charging system must have the following features:

1) A series-connected *LC* circuit is an optimal topology that provides a constant or controllable charging voltage and maintains higher efficiency during each charging cycle.

2) An effective and universal control method based on the DC characteristics of resonant circuits is applied to track the optimal AC frequency before charging begins and to adjust the frequency during charging processes.

3) The square pads generating non-polarized flux are more suitable for universal inductive charging because of tighter magnetic coupling and higher power-transfer capability.

For the design of on-board chargers, this thesis analyzes two commonly-used types of resonant topologies on the secondary side: series-connected *LC* circuits and parallel-connected *LC* circuits. Each type of secondary *LC* circuit has its own advantages and specific applications. When the on-board charger applies a series- or parallel-

connected *LC* circuit, two design schemes are separately analyzed, The design of the on-board charger also includes three aspects: the *LC* resonant circuit (by choice), the control strategy used, and the charging pad, or coil. The proposed on-board chargers work in coordination with the previously proposed inductive charger for more accurately tracking the optimal frequency and better charging V&I control.

To validate the proposed universal inductive charging system, theoretical calculations, simulations, and hardware prototypes are used. The efficiency of the system, the accuracy of frequency control, and the stability of the system are comprehensively tested. The results demonstrate that the proposed design schemes are robust and applicable.

CHAPTER 1: INTRODUCTION

1.1.   Problem Statement

Inductive power transfer (IPT), which has been applied in a wide range of applications from portable devices to medical apparatuses, is a promising method for charging electric vehicles (EVs). IPT, or inductive charging, inductively transfers the high-frequency AC power in the transmitting coil to the receiving coil in the load by magnetic coupling [1-5]. Compared with traditional plug-in chargers, inductive chargers are operated in a more convenient, aesthetic, and safer way.

Although IPT technology has significant advantages over the traditional plug-in method, inductive charging of EVs has some serious problems that strongly limit its practical applications. One problem is that the air gap between the transmitting and receiving coils is around 10 ~ 25 cm. A large air gap leads to low coupling between the transmitting and receiving coils. Misalignment (or horizontal offset) between the coils further reduces the coupling effect. To improve magnetic coupling, researchers have proposed several methods. For example, ferrite bars are used to forcibly guide the magnetic flux, and mechanical methods can be applied to shorten the air gap and decrease horizontal misalignment. However, the magnetic coupling coefficient between the transmitting and receiving coils is still much lower than that in traditional transformers. A common range of the coupling coefficient is from 0.1 to 0.25. The low coupling effect directly influences the two most important parameters for evaluating a charging system: efficiency and power-transfer capability. Meanwhile, large leakage inductances of the coils exacerbate control of the system and increase the voltage and

current stress on components. The power factor also decreases when magnetic coupling decreases. Because of lower power factor, the input power source needs to be specifically designed. Electromagnetic radiation is also a problem aggravated by larger air gap.

Another problem of the practical application of IPT is that the horizontal misalignment between the coils varies in different charging cycles because the parking position of a vehicle varies from time to time. The air gap between the coils can also be changed by reduced tire pressure. The varied air gap and horizontal misalignment lead to varied coupling effects between the coils. Thus, the electrical characteristics of the overall system can be seriously changed. For example, the nominal output cannot be maintained when the charged EV is parked in a different position over the transmitting coil. The system efficiency is influenced as well. Therefore, the system needs a comprehensive and adaptive control strategy to provide stable and efficient charging power to the load, even when the coupling effect is changed.

The practical application of IPT is also limited because no universal charger suitable for charging the EVs of various designs is currently available. Nowadays, various EV models exist on the market, and more will be released in the future. Faced with the rapidly growing market of EVs, the design of a universal charger will become more and more important. The current standards of IPT have limited some basic parameters of the IPT system of EVs, such as the AC frequency, the nominal voltage, and three power levels. However, these standards are not enough for designing a universal wireless charger. Thus, a design scheme of the universal charging system is necessary, including the design of the input power source, resonant circuits, the control strategy, communications, and so on.

Finally, coordination between an inductive charger and a charged EV are more difficult to conduct than that in a plug-in charging system because there is no direct wire-connection between the charger and the load. Wireless communication is a typical method used to transmit the transient information for system control, such as feedback voltage and current, and the order information such as start, stop, pause, or error. But, the real "transient" control on the system cannot be achieved by wireless communication because current wireless-communication equipments can hardly transmit transient V&I information of AC power that is around 85 kHz. Thus, a better modulation of the primary charger or the on-board charger is only dependent on the transient voltage and current information of its own side. In other words, the converters on the two sides work in coordination without wireless communication between each other. This also reduces cost and system complexity.

To mitigate the problems caused by low and varied coupling effects between coils and various load designs, a universal inductive charger (UIC) for EVs must be designed. The control of the system should be adaptive, comprehensive, and easy. A design standard of UIC should be analyzed and summarized. A design scheme of the on-board chargers that work in coordination with UIC should contribute to the proposed universal charging.

1.2. Research Objectives

The main goal of the research is to design a universal inductive charging system for multiple models of EVs. According to the traditional structure of an IPT system, the research includes the design of the UIC and the design of on-board chargers working in coordination with the UIC. To achieve the universality of the IPT system, the dissertation

objectives are 1) to propose a UIC that adaptively provides a constant or controllable charging voltage to various EVs, even with a wide range of varied magnetic coupling between the transmitting and receiving coils; 2) to develop a scheme of designing a Series-*LC*-based on-board dual-mode charger which cooperates with the previously proposed UIC for more universal, efficient, and safe EV charging in various coupling and load conditions; 3) to develop a parallel-*LC*-based on-board charger for dealing with a large range of the optimal frequencies and a higher voltage stress on resonant capacitors when a series-connected *LC* circuit is applied. A UIC and two basic types of on-board chargers achieve the "real" universal charging. The detailed analysis of the system focuses on the design of the *LC* resonant circuits, the control strategy of the inverter/converter, and the design of the charging interfaces (charging coils or pads).

Initially, the dissertation presents a design process of a UIC for EVs. The proposed UIC is capable of adaptively providing a constant or controllable charging voltage to various EVs, with a wide range of varied magnetic coupling between the charging coils. With a series-connected *LC* circuit, Zero-Voltage-Switching (ZVS) of the primary DC-AC inverter is universally achieved in every charging cycle. A simple yet effective control method is used to automatically track the optimal frequency in different coupling conditions and adjust the frequency during the charging process. The design of the charging interface is also optimized based on higher efficiency and higher power-transfer capability. Simulations and prototypes validate that the proposed UIC is accurate, robust, and applicable.

Besides improvements of the primary charger, EV manufacturers need a design standard for the power-receiving part for adaptive charging in various conditions. An on-

board charger realizing AC-DC conversion is necessary for power regulation and safety protection, because magnetic coupling between the two coils is easily influenced by the environment. Accordingly, a scheme of designing an on-board charger is also proposed to cooperate with the UIC for more universal and accurate control. The optimal design of the secondary LC circuit is analyzed, including the LC connection (Series-connected secondary LC circuit) and the receiving pad (shape and size). A simple control method based on the dual-mode operation of the on-board DC-DC converter is applied, to coordinate with the UIC for more accurate control on the frequency and voltage. Finally, simulation results and a prototype validate that the proposed on-board charger improves the control accuracy (frequency error < 0.5 kHz) of the UIC and provides a stable charging voltage to batteries (voltage error < 10%). The IPT system with the proposed on-board charger performs better in universal inductive charging.

The series-connected LC and parallel-connected LC circuits are the two basic resonant topologies. To achieve the real universality of the system, a design process of Parallel-LC-based on-board chargers is also proposed, although a Series-connected LC circuit proves to be the optimal resonant topology of the on-board charger. More importantly, the concept of UIC requires high-efficiency and stable charging when the load contains a parallel-connected LC circuit. The advantages of parallel-connected LC circuits over series-connected LC circuits are demonstrated. A parallel-connected LC circuit has a small range (< 2 kHz) of the optimal frequencies vs. magnetic coupling and a much lower voltage stress on the resonant capacitors. For more accurate frequency control and ZVS of the primary charger, a small inductor is added on the parallel-LC

5

(similar to an *LCL* structure). Simulations and hardware experiments are used to test the proposed design.

In summary, the design of a universal inductive charging system consists of a primary UIC and an on-board charger. Design details of the UIC and on-board chargers are optimized according to the definition of universal charging. The *LC* resonant circuit is optimized according to the stable output voltage vs. magnetic coupling. Based on the chosen *LC* circuits, the control strategies are designed to adaptively provide stable output voltage and high-efficiency charging with varied coupling effects and load conditions. The charging interfaces are optimized for the highest coupling vs. horizontal misalignment or air gap, when the coil size is limited.

1.3. Thesis Outline

The outline of the remaining parts of this dissertation is as follows.

Chapter 2 provides background information on the origin of the topic along with presently available technologies that are being used and a brief introduction of the basic working principles of the inductive charging. It also includes comparisons between the plug-in charging and inductive charging technologies, with advantages and current challenges of inductive charging technology. In addition, it provides detailed descriptions of the currently existing topology designs, control methods, and designs of charging interfaces and summarizes and analyzes the cons and pros. Finally, it defines the UIC.

Chapter 3 presents a detailed design process of a UIC for EVs defined in Chapter 1. It includes three main aspects of the design: the design of primary *LC* resonant circuit, the control strategy applied for universal charging, and the design of charging interfaces.

It demonstrates that the series-connected *LC* circuit with a fixed-gain point vs. frequency is the optimal topology with advantages including a stable output voltage vs. coupling and higher efficiency. It applies a control loop based on the frequency-tracking method to choose the AC frequency at fixed-gain point before changing cycle begins and to adjust the AC frequency for increasing power factor and improving system efficiency during the charging processes.

Chapter 4 presents a detailed design process of an on-board charger for EVs, which cooperates with the previously proposed UIC in Chapter 3. It includes three same aspects of the design: the topology of *LC* circuits, the control strategy of the AC-DC converter, and the design of the receiving pad or coil. It analyzes the design scheme of the on-board chargers mainly based on the design details and adaptive operation of UIC. It proves that the series-connected *LC* circuit on the load side is better for universal charging because of a more stable output voltage vs. coupling effects. It proposes the design and optimization of the receiving pad based on the nominal output of the system and size limitation of the receiving pad. It applies a dual-mode modulation of the DC-DC converter for more accurate frequency tracking and charging-voltage control.

Chapter 5 presents an alternative design of on-board chargers used in universal inductive charging. It applies a parallel-connected *LC* circuit that is another basic *LC* topology besides the series-connected *LC* circuit in Chapter 4. Its design and control of the on-board DC-DC converter are different either. It proves that the proposed design has advantages such as a small range of the optimal frequency and significantly lower voltage stress on the resonant capacitor. According to the definition of universal inductive charging, the design with parallel-connected *LC* circuit is the last piece of the jigsaw.

Chapter 6 presents a summary of the hardware prototypes used for validating the proposed design. The hardware system can be classified into three parts: the primary DC-AC inverter and the relevant control system, the DC power supply, and the on-board AC-DC converter and the relevant control system.

Finally, Chapter 7 summarizes the research work, and outlines the results and contributions of this dissertation. Directions of future research are also provided.

Moreover, three appendices are listed at the end of this dissertation. Appendix A presents the theoretical calculations and simulation models used for circuit analysis of the UIC. Appendix B presents the models of magnetic simulation, used for analyzing the charging interfaces. Appendix C presents the laboratory implementation of the UIC and on-board charger, including system schematics, PCB design, DSP codes, bills of materials, etc.

CHAPTER 2: LITERATURE REVIEW

2.1.   Overview

This chapter provides the background information of current research related to the proposed research along with a literature review of the research efforts on these topics. Section 2.2 provides an overview of the basic structure of an inductive charging system, the comparisons between plug-in and inductive charging technologies, and the existing challenges for inductive charging. Section 2.3 summarizes the current research on primary and secondary LC circuits applied in inductive charging. Section 2.4 provides a literature review on the control strategies currently applied in inductive charging. Section 2.5 analyzes the pros and cons of various designs of charging interfaces (pads/coils). Section 2.6 summarizes the existing problems of the previously proposed research.

2.2.   Background of Inductive Charging

2.2.1. Basic Structure

The basic principle of inductive power transfer (IPT) technology is identical to that of well-known closely coupled electromechanical devices such as transformers and induction motors [1-4]. The fundamental structure of a typical inductive charger consists of a power source, magnetic-link, two resonant circuits and a battery charger, shown in Fig. 2.1. First, a power source with the power-factor-correction (PFC) produces AC power in the primary resonant LC circuit, where L is the inductance of the transmitting pad, or coil. Then, the receiving coil gets the AC power via induction (magnetic link) and generates AC power in the secondary LC resonant circuit. Finally, the battery charger in
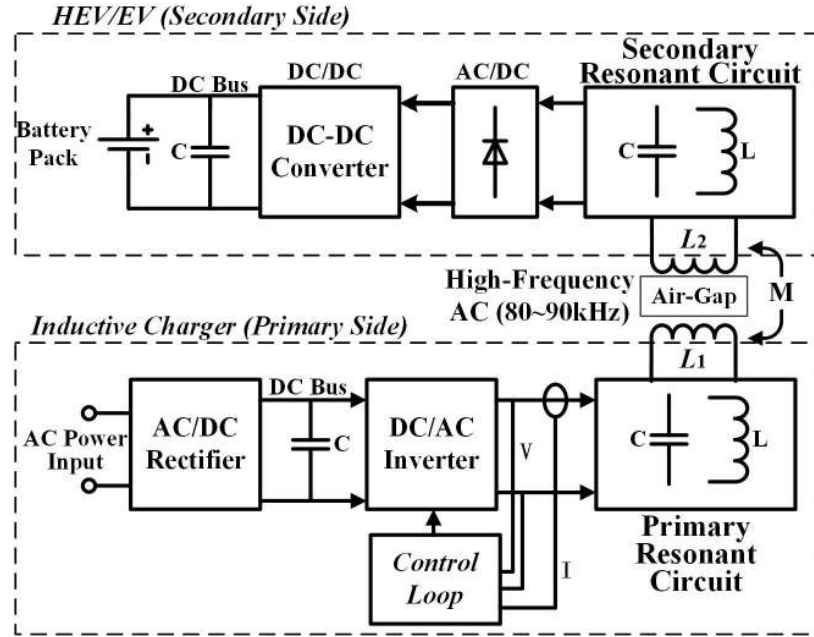
Fig. 2.1. The main structure of an inductive charging system [12].

the load conducts AC to DC conversion, providing charging voltage and current for EV

batteries. The power source and the primary inverter can be treated as an AC input, while

the secondary converter and the batteries work as an equivalent load [6-11]. Different

from the structure shown in Fig. 2.1, the diode-bridge can be replaced with an actively-

controlled converter, which could be more efficient than common diode-bridges. This

means that the diode-bridge and the DC-DC converter can be merged into one structure.

The basic topology of an IPT system is formed by two *LC* resonant circuits: the

primary resonant circuit of the charger on the primary side and the secondary resonant

circuit in the load [13]. There are various kinds of topologies of inductor *L*'s (charging

coil and other inductors) and capacitors *C*'s for a resonant circuit, such as series-

connected or parallel-connected *LC* circuits, *LCC* circuit, and so on. The resonant circuits

are chosen according to the specific application, including voltage and current, the range

of AC frequencies, power levels, and so on.

For the system control, much attention is paid on modulating the primary inverter before the primary resonant circuit [14-17]. Thus, the system can be done by adjusting the input voltage of the primary resonant circuit, the AC frequency, and the power factor from the grid side. Other research has been done on controlling the secondary converter in coordination with the primary inverter. For more accurate control or some safety considerations, wireless communication apparatuses can be installed to transmit relevant information between the two sides.

Non-polarized and polarized charging coils are the two basic structures for the charging interfaces (coil/pad). Each of the two structures owns specific design characteristic such as shapes, sizes and coil turns [18, 19]. A different type of structures derived from transformers is commonly applied in on-line inductive charging (dynamic charging) for EVs. The structure places the parallel connected coils in a row under roads [20]. The design of the coil determines the value of the primary inductance, the coupling effects between coils, and the resonant frequency of the *LC* circuit.

2.2.2. Plug-in Charger vs. Inductive Charger

Nowadays, most of the practical chargers for EVs are plug-in ones –users need to insert a plug into a receptacle on the car to charge the batteries. The electric power is transferred to EVs by the direct wire-connection between the plug and receptacle, or the magnetic coupling between the coils installed in the plug and receptacle. However, several problems limit practical applications of plug-in chargers. First, the cable and connector typically deliver two ~ three times more power than standard plugs at home, and this increases risk of electrocution especially in wet and hostile environments [21, 22]. Second, the long wire poses a trip hazard and is poor in aesthetics. Third, in harsh

11

environment that involves snow and ice, the plug-in charge point may get frozen onto the vehicle. Over the years, alternative charging technologies for EV's have been investigated. One of the most famous solutions is inductive charging. Inductive charging has a lot of advantages over traditional plug-in charging, including:

1) The galvanic isolation between the charger and EV, meaning better security.

2) Requiring less maintenance, because most of the components of the system are protected by the proper encapsulation which decreases the deterioration.

3) Safer and more practical applications in harsh environments.

2.2.3. Challenges of Inductive Charging

Despite the fact that the inductive chargers have several advantages over traditional plug-in chargers, some problems and challenges of inductive charging still limit its practical applications. These problems seriously limit the practical application of the inductive charging. The first and the most serious problem is the varied coupling between the transmitting and receiving coils caused by varied air gap and horizontal misalignment. Because the physical position of a car can hardly be exactly the same in different parking times, the magnetic coupling between the coils will be varied. This variance has distinct influences on the electrical characteristics of the system, such as the impedances, the voltage gain, etc. Secondly, the resonant circuit in the inductive charger is hard to tune, especially when the coupling can be varied. As a matter of fact, most of the current research about controlling inductive chargers focuses on tuning the resonant circuit. Radiation is also a problem, when the charging power of EVs is higher than 1 kW [23]. Finally, more and more EVs are under research and sold on the market, with tons of designs or electrical topologies applied. But, a relevant standard for wireless charging

hasn't been released yet. Therefore, currently proposed inductive chargers are not capable of universally charging various models of EVs. In fact, the IPT can hardly be generally applied, if these problems cannot be solved. The research proposed in the dissertation focuses on solving the charging problems caused by varied magnetic coupling and various load designs, to make the inductive charger be "universal".

2.3. Design of the Resonant Circuits

2.3.1. General Topology Analysis

In a typical IPT system for EVs, there are four basic topologies: Series-Series-connected (SS-connected), Series-Parallel-connected (SP-connected), Parallel-Parallel-connected (PP-connected) and Parallel-Series-connected (PS-connected) LC circuits, shown in Fig. 2.2(a) [24]. Using a mutual-inductance model, the equivalent circuit of the
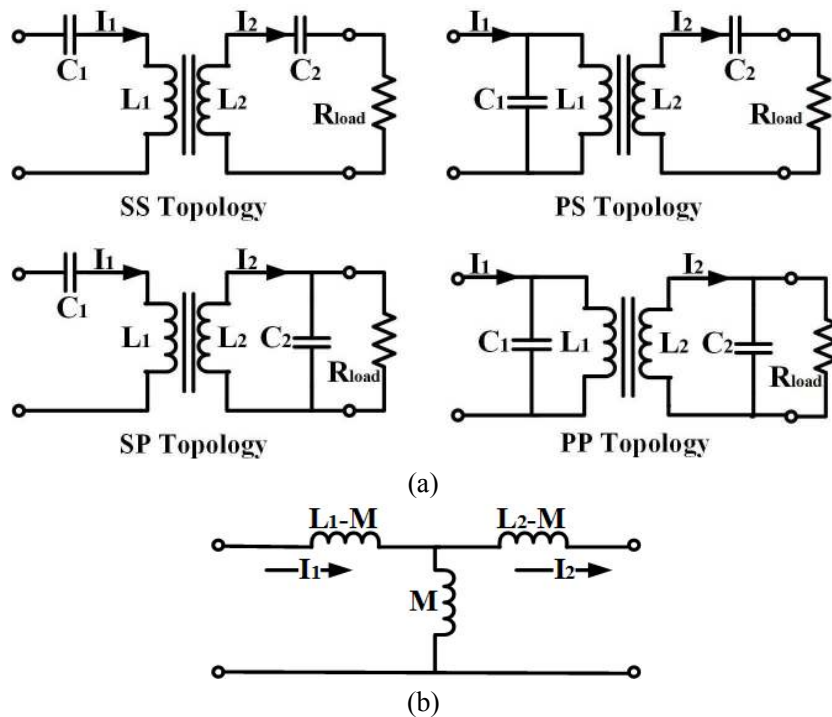
Fig. 2.2. Topologies of the resonant circuits in an IPT system: (a) four basic combinations and (b) the equivalent circuit of the inductances.

resonant inductances is shown in Fig. 2.2(b), where M is the mutual inductance between

the transmitting and receiving coils or pads. The coupling coefficient is

$$k = M / \sqrt{L_1 L_2} \, ,$$

which is one of the most important parameters in wireless charging. In practical

applications of wireless charging of EVs, k typically ranges from 1/10 to 1/4. The circuit

analysis can base on the mutual-inductance model. Another common method of circuit

analysis bases on the reflected impedance. For example, if the secondary LC circuit is S-

connected, the reflected impedance from the secondary side to the primary side is

$$Z_r = \frac{\omega^2 M^2}{j\omega L_2 + \dfrac{1}{j\omega C_2} + R_{load}} , \tag{2.1}$$

and the reflected impedance is

$$Z_r = \frac{\omega^2 M^2}{j\omega L_2 + \dfrac{1}{j\omega C_2} \parallel R_{load}} ,$$

if the secondary LC circuit is P-connected, where ω is the frequency of the AC power.

The total impedance seen from the AC power source is

$$Z_{total} = \frac{1}{j\omega C_1} + j\omega L_1 + Z_r , \tag{2.2}$$

if the primary LC circuit is S-connected. The total impedance is

$$Z_{total} = \frac{1}{j\omega C_1} \| (j\omega L_1 + Z_r), \tag{2.3}$$

if the primary *LC* circuit is P-connected. The resonant frequency is commonly chosen as the AC frequency of the resonant circuit by the equation:

$$\omega_0 = \frac{1}{\sqrt{L_i C_i}}, \ i = 1, 2. \tag{2.4}$$

Normally, the resonant frequencies of both sides are reasonably set to be equal:

$$\omega_0 = \frac{1}{\sqrt{L_1 C_1}} = \frac{1}{\sqrt{L_2 C_2}}. \tag{2.5}$$

The output voltage and current can be calculated based on the impedances. Obviously, the varied mutual inductance *M* (much smaller than common transformers) will seriously influence the charging characteristics – the output voltage and current. The output can also be changed by adjusting the AC frequency in a certain range. However, the influence of *M* and the AC frequency is determined by the *LC* resonant circuit. A well-designed resonant circuit is able to significantly reduce the impact of varied magnetic coupling, leading to a more stable system. Of course, control methods of the wireless-charging system should be applied based on selected resonant circuits. A reliable IPT system must employ an appropriate topology for the *LC* resonant circuit.

2.3.2. Primary LC Circuit

A lot of IPT research focuses on selecting an optimal topology for *LC* resonant circuits [24-29]. Most of the analysis of resonant circuits is based on improving the system stability, increasing the system efficiency, or other specific standards.

For the primary side, a P-connected *LC* has drawbacks such as high turn-off current, and so on. Compared to the P-connected *LC* circuit, the S-connected topology is preferred for the following reasons:

i)   S-connected *LC* resonant circuit is easier to tune, especially in long-track applications [24]. With a long track or a coil with a large number of turns, the coil inductance can be large, leading to a high impedance in high-frequency applications [30]. The impedance of a P-connected *LC* circuit may be too large for the power supply with a limited voltage rating to drive. Thus, the current will be low for EV charging and the system efficiency decreases. Accordingly, a small or even zero series-tuning capacitor is necessary.

ii) An S-connected *LC* resonant circuit leads to a stable optimal resonant capacitance vs. magnetic coupling. In most of traditional IPT systems, the resonant capacitance is selected according to the resonant inductance and the planned AC frequency. As magnetic coupling effect varies, the optimal value of the resonant capacitance changes accordingly. The ideal condition is that the optimal capacitance is relatively stable when magnetic coupling varies. As shown in Fig. 2.3, a S-connected *LC* circuit requires a relatively stable value of capacitance with varied quality factors Q or coupling coefficients k, no matter which topology the secondary side employs [24]. It indicates the ideal and the normalized capacitance with various quality factor Q and the coupling coefficient k. The ideal capacitance maintains constant when the secondary side employs an S-connected *LC* circuit and increases gently when the secondary side is a P-connected circuit. This effect may be more significant in magnetic resonant situation since its Q is large (> 10).

16
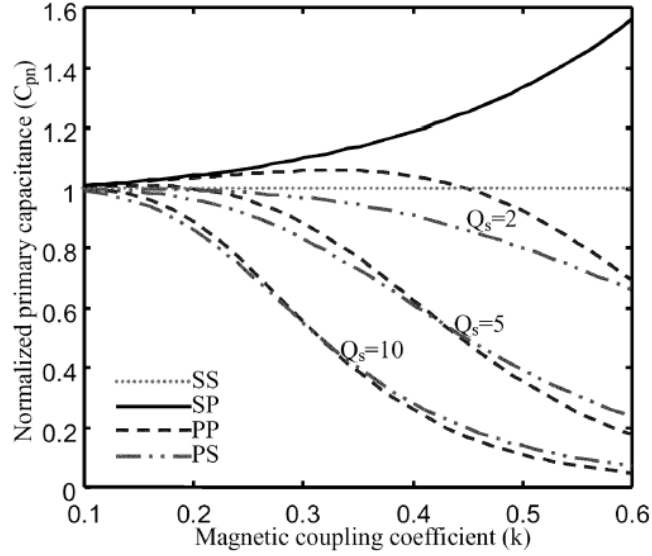
Fig. 2.3. Normalized primary capacitances with various topologies and quality factors (*Q*) [24].

iii) S-connected *LC* circuits perform better in harmonics reduction, with significant parasitic components caused by loosely magnetic coupling [25, 31].

However, an S-connected *LC* circuit also has several shortcomings. For example, the voltage stress on the resonant capacitance is high (> 2000 Vrms) with the resonant frequency [32]. Thus, capacitors with high voltage tolerance are necessary.

Besides S- and P-connected resonant circuits, more developed topologies are also proposed [33-36]. A typical topology applied in the primary side is the T-*LCL* compensated resonant circuit [15, 37-40], shown in Fig. 2.4. The *LCL* circuit combines the advantages of S- and P-connected resonant circuits. With an *LCL* circuit, the Zero-Current-Switching (ZCS) can be achieved through charging processes and the output current is kept as a constant independent of load. However, the constant-current mode is not necessary for the chargers in Levels 1 and 2 because EVs have their own on-board AC-DC converters for regulating the charging current and voltage and protect the system

17
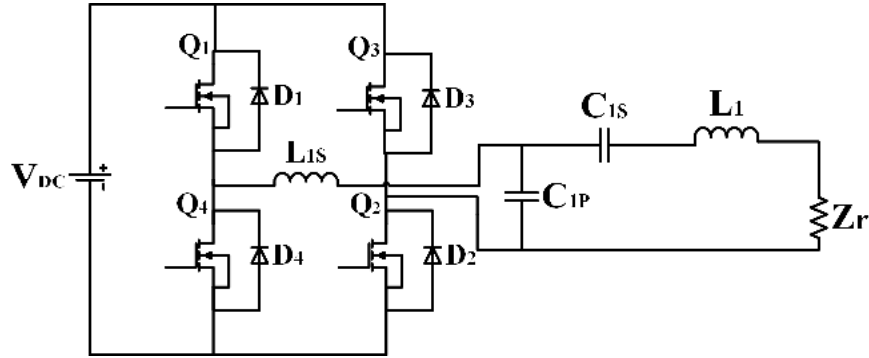
Fig. 2.4. IPT system with *LCC* resonant circuit, where L_{1s} is the added S-connected inductor, C_{1p} is the added P-connected capacitor and the C_{1s} is the resonant capacitor with L_1 [45].

from varied coupling. Thus, the output of the *LC* resonant circuit on the EV is directly connected to the on-board converter that prefers a stable voltage input (a typical range of error < 15 %) [41-43]. Therefore, a constant-voltage mode is more suitable for inductive charging. Moreover, more passive elements in the resonant tank need complex nonlinear control [44], or the output gain of the system is significant varied by magnetic coupling [39]. Meanwhile, much more reactive power stored in the *LCL* circuit generates more power losses caused by parasitic elements in *L*'s and *C*'s. Finally, ZCS operation in the *LCL* circuit is not efficient when the full-bridge inverter is working with high frequency and high input voltage.

Other topologies for resonant circuits have also been proposed by previous research, such as *LLC* and *LCC* circuits [39, 40, 45-49]. More technical comparisons among the various topologies will be made in the next Chapter, based on the output characteristics and soft-switching operations.

2.3.3. Secondary LC Circuit

For the *LC* resonant circuit in the secondary side (load), the P-connected *LC* is preferred by some previous research [5, 38, 50, 51], because the electrical characteristics of a P-connected *LC* circuit are more suitable for charging batteries. A fully tuned (impedance matched) P-connected *LC* circuit acts as pure current source, while a fully tuned S-connected *LC* circuit yields a pure voltage source [38]. So, in practical applications, if the load resistance is too small for series *LC* circuit or too large for P-connected *LC* circuit, the quality factor (*Q*) in the load side will be large (larger *Q* leads to more difficult tuning of *LC* circuits and a system more sensitive to parameter variations) [52]. Moreover, in some papers published in late 1990s, the SP topology was demonstrated to be ideal for the inductive coupling applications because of the presence of a loosely coupled transformer with significant parasitic components. For example, in [5, 51], the fundamental mode analysis (FMA) is applied to show that SP is the best topology with significant parasitic components.

Some research prefers the S-connected *LC* as the secondary resonant circuit, because the total impedance can be purely resistive with an SS-connected resonant circuits, and the normalized primary capacitance will be independent of either the magnetic coupling or the load [53]. However, with an S-connected secondary *LC* circuit, the pure resonance is hard to maintain when *Q* is high. As a result, some of previously proposed designs avoid resonance when designing a WPT system and choose the unity-gain frequency as the frequency of AC power. The capacitance is selected such that sufficient amount of power can be obtained without resonance. Based on the voltage-source model by the S-connected *LC* circuit, a voltage regulator following the secondary *LC* circuit is required to keep the output voltage controllable.

Other topologies have also been proposed for the secondary *LC* circuit. For example, the *LCC* circuit can also be applied as the secondary topology [15]. In [54], an IPT system with one-side capacitor compensation is proposed: the resonant capacitor in the EV side is replaced by the active resonant circuit. The coordination between the two sides is necessary, such as the phase-difference modulation. An IPT system working with multiple frequencies is developed in [33]. The system applies the ladder *LC* Cauer 1 topologies in the EV side to build a multi-resonant receiver.

Right behind the secondary resonant circuit, there will be an AC-DC converter to provide DC power to the following DC-DC converter, as shown in Fig. 2.5. The AC-DC converter can be a diode-bridge without active control or a full-bridge converter built by actively controlled switches. If the switches of the AC-DC converter are actively controlled, the power can be bi-directionally transferred. The direction of the power flow is determined by the phase difference between the input voltage of the primary *LC* circuit and the output voltage of the secondary *LC* circuit. By controlling the duty cycle and the frequency, the amount and the direction of the transferred power can be adjusted [55, 56].

2.4. Review of the Control Methods

As indicated in Fig. 2.1 and Fig. 2.2, an AC source generates the high-frequency
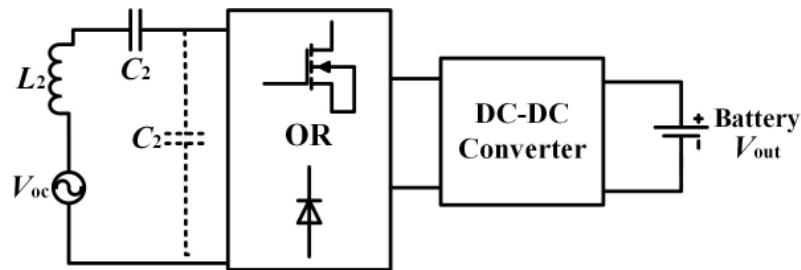
Fig. 2.5. An equivalent structure of the on-board charger in an IPT system.

AC power (normally in the range of 20 kHz ~ 200 kHz in most of the current research) to the primary *LC* resonant circuit. The system converts the AC power from the grid to a stable DC output (AC-DC conversion) and generates a high-frequency AC to the primary *LC* circuit by the certain control methods (DC-AC conversion), summarized as an AC-DC-AC conversion. For system safety, the *LC* connection and values of the resonant inductors and capacitors cannot be adjusted during the charging process. Thus, the electrical characteristics of the AC power are only dependent on the control methods of the AC power source. For example, the frequency and the duty cycle of the switching signals can be modulated to optimize the system operation. On the other hand, a typical application is the bi-directional IPT. The bi-directional power transfer can be achieved only if the on-board AC-DC charger (at the output ports of the secondary *LC* circuit) is built by an actively-controlled full-bridge converter [14]. However, to achieve bi-directional power transfer, the charger on the primary side must acquire the information of load voltage and current. Thus, the system must have wireless-communication apparatuses and a more complex control method [1, 46]. This dissertation focuses on coordination between the two sides without wireless communications. Because the front-end AC-DC part of the charger has been thoroughly analyzed by previous research, this dissertation concentrates on the control of the DC-AC conversion.

2.4.1. Pulse-Width-Modulation of the DC-AC Inverter

A typical DC-AC model in an inductive charger is a full-bridge DC-AC inverter. A DC-AC inverter is commonly controlled by Sinusoidal-Pulse-Width-Modulation (SPWM), which is used to modulate the duty cycle of the switching signal, with an already-known frequency. Two schemes for SPWM – unipolar and bipolar voltage

switching, have been thoroughly studied by previous research. As a result, in most of the current research on IPT, more attention is paid on frequency control and the duty cycle is usually set as 50% (ignoring the dead time). Or, the SPWM usually works as the inner loop of a double-loop control scheme.

For the control of on-board charger for EVs, Pulse-Width-Modulation (PWM) is generally used for DC-DC conversion. The converter with PWM is finally connected to the charged batteries and provides the nominal voltage and current to the batteries. More complex control strategy is necessary if the on-board charger applies a battery-management-system (BMS). But battery management is not the main focus here.

2.4.2. Frequency Control for Uni-directional Power Flow

In most of the control methods of IPT systems with uni-directional power flow, the charger (or the AC source part) needs to choose an optimal AC frequency, based on the voltage gain and load-phase angle of the equivalent impedance looking from the input of the primary LC resonant circuit, as the Z_{total} in Equation (2.2) and (2.3) [4, 28, 57-64]. Since the equivalent impedance is related to the inductances and capacitances on the two sides, the coupling effect, and equivalent resistance of the load, the load-phase angle of Z_{total} can be varied by the coupling effect and charging status of the batteries. The choice of frequency should be done before the charging process begins, because all of the related factors in a charging cycle are different from those of the last cycle, such as the variance of the EV position and energy left in the batteries. The optimum frequency is also varied because of different topologies. In the most common topology, SS-connected LC circuits, two commonly used frequencies are: the resonant frequency and the unity-gain frequency. The resonant frequency is determined by the resonant inductance and

22

capacitance, shown in Equation (2.4). The resonant frequency is not related to the mutual inductance. The unity-gain frequency is the frequency at which the leakage inductance is compensated by its according capacitance. For example, if the IPT system applies series-series connection of the resonant circuit with $L_1 = L_2$ and $C_1 = C_2$, the equivalent circuit is shown in Fig. 2.6(a). The resonant frequency can be calculated by Equation (2.5). The unity-gain frequency of the circuit in Fig. 2.6(a) is:

$$\omega_1 = \frac{1}{\sqrt{(L_1 - M)C_1}} = \frac{1}{\sqrt{(L_2 - M)C_2}}.$$

(2.6)

Fig. 2.6(b) shows the voltage gain V_{out}/V_{in} and the load-phase angle of Z_{total} vs. the AC
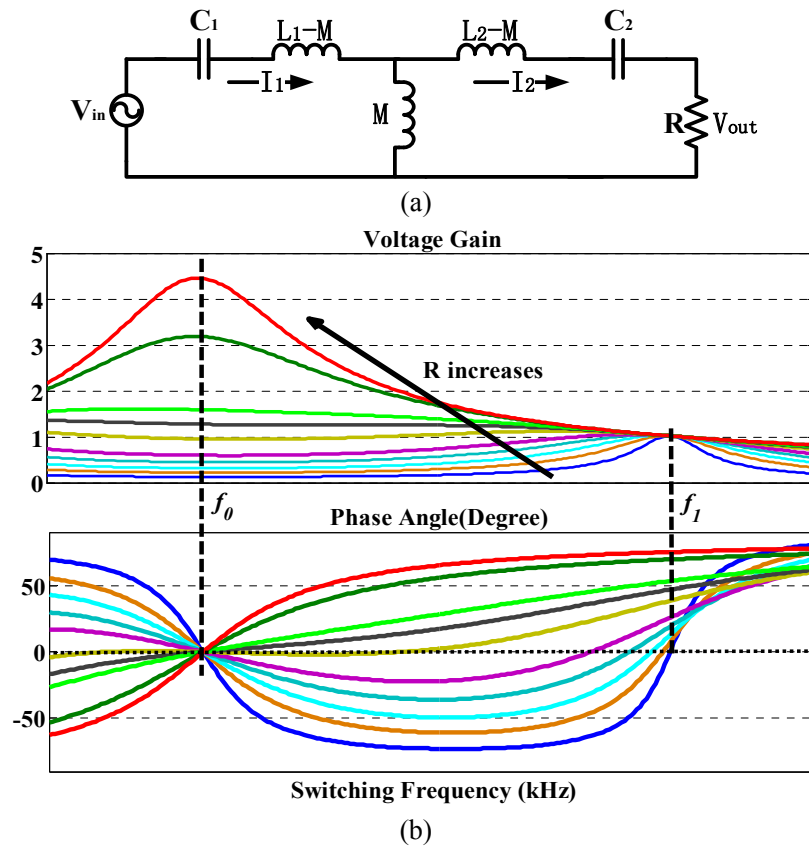
Fig. 2.6. (a) The equivalent circuit of the IPT system with SS-connected LC circuits and, (b) the voltage gain (ratio of the magnitude of output voltage to the magnitude of input voltage) and load-phase angle vs. AC frequency.

frequency, based on the circuit in Fig. 2.6(a). The f_0 is the resonant circuit while the f_1 is the unity-gain frequency. At the resonant frequency f_0, the phase angle of the Z_{total} is always zero (purely resistive). Moreover, the resonant frequency is set by Equation (2.5) before charging and not varied by coupling effect; addition control methods are not necessary. As a result, the resonant frequency is usually chosen as the operation frequency [16, 50, 58, 65]. However, the voltage gain at the resonant frequency is not controllable, generating more challenges to the AC-DC converter in EVs. Meanwhile, the switches of the DC-AC inverter who generates V_{in} cannot achieve soft switching at f_0, leading to lower efficiency. To solve the soft-switching problem, some research also applied the unity-gain frequency as the AC frequency [53]. If the coupling effect keeps constant in a charging process, the unity-gain frequency keeps constant, and the voltage gain from the input of the primary LC circuit to the output of the secondary LC circuit is always unity at the unity-gain frequency. The value of the unity-gain frequency is not influenced by the variance of the equivalent resistance of the batteries, meaning that the f_1 keeps constant during the charging process (M is fixed). Moreover, when the frequency is higher than the unity-frequency, the load impedance looking from the input terminal is always inductive and Zero-Voltage-Switching (ZVS, actually ZVS turn-on here) can be maintained during every charging process.

Some other control methods based on frequency-control are applied in the IPT system with uni-directional power flow. For example, in [14], the system with the SS-connected LC applies a frequency between f_0 and f_1 and works with ZVS. But the system assumed the load and the mutual inductance to be in a limited range, making it possible for the designer to calculate a range of the frequency with ZVS. By similar theories, in

24

[37], an IPT system based on the *LCC* circuit applied a fixed frequency to achieve the Zero-Current-Switching (ZCS). In [33], the system was able to transfer power by multiple frequencies, with a special topology – *L-C-L-C* ladder configuration. In fact, the application of the idea is limited in the frequency range – the AC frequency was set to be a fixed value when designing the system and only the three times frequency can be another appropriate frequency.

2.4.3. Frequency Control for Bi-directional Power Flow

In an IPT system, the bi-directional power flow can be achieved when the AC-DC converter following the secondary *LC* circuit is actively controlled. If the primary and secondary *LC* circuits are tuned to be resonance with the same frequency and equal duty cycles (0.5 as usual), the transferred real power can be regulated via shifting the phase angle between V_{out} and V_{in} [54, 55, 66, 67], as shown in Fig. 2.6(a). Let the phase angle between V_{out} and V_{in} be φ, then the output voltage of the secondary *LC* circuit is $V_{out}\angle\varphi$ while the terminal output of the primary DC-AC inverter (the input of the primary *LC* circuit) is $V_{in}\angle 0$. The real power transferred from the grid to the load is:

$$P_0 = P\sin(\varphi), \qquad (2.7)$$

where P is a constant related to V_{out} and V_{in}, the coupling effect and the frequency. When V_{out} leads V_{in} from 0 to 180 degree, the power is transferred from the primary side to the secondary side, and the power level reaches the maximum value when V_{out} leads V_{in} by 90 degree. On the contrary, the power will flow from the load back to the grid if V_{out} lags V_{in}. When the phase angle is $\pm 90°$, neither converter produces any reactive power.

2.4.4. Other Control methods

In an IPT system, there is no wired transmission between the charger and the load. If both sides want to know about the transient characteristics of each other, sensors and wireless apparatuses may be applied to build the communication routes [46, 64, 68, 69]. However, this made the system more complicated and expensive. It also has limitations on the control rate since the AC frequency is too high for some algorithms and micro-controllers. To avoid the necessity of wireless apparatuses, some other methods have been proposed to allow both the charger and the load to acquire adequate information for control algorithm, just by detecting the voltage and current in their own sides. The most commonly used method is adding some auxiliary parts to help control the converters [53, 55, 70-72]. This method is especially popular for the load-side controlling. For example, as mentioned previously, the load in [55] used an auxiliary winding to sense the primary current and then help the secondary converter to control the direction of the power flow. In [72], the proposed system used a more straightforward way – adding another resonant capacitor in the secondary LC circuit. The connection of the additional capacitance is actively controlled by a switch, based on the value of the charging current. In [53], the load had been added a "dummy resistor" in a specific value to track the unity-gain frequency for the charger (the primary side).

2.4.5. Wireless Communications

Although applying wireless apparatuses makes both the design and control of an IPT system much more complicated, we must use wireless apparatuses if we want a comprehensive control system. For example, if the charger acquires the voltage and current standard of the batteries by wireless communication, the charger is able to

provide a more appropriate output accordingly. This lowers the requirements and even simplifies the operation of the secondary converter. Moreover, the essential information such as operation orders (start. pause, stop, and so on) or system faults (over current, and so on) from the charged EV, need to transmit to the charger wirelessly.

Common wireless communication technologies such as Wi-Fi and Bluetooth are used nowadays. The Wi-Fi is more universally used in current electronic products and can be inter-operated at a basic level of service, making it a promising way for wireless communication used in IPT systems.

2.5. Design of the Charging Interfaces

The design of charging interfaces can be classified into the traditional designs developed from common transformers with the magnet structures of E-core or C-core (U-type), and the plane-core structures with horizontally-placed core, or air core. [18, 65, 73-78]. The plane-core structures are the mainstream of current designs. For an IPT system, a big challenge is the reduced coupling effect caused by a large air gap or horizontal misalignment (offset) between the transmitting and receiving coils. Therefore, a better design of charging interface has higher tolerance (better coupling) with the same air gap and horizontal misalignment [18, 50]. Although the coupling effect is improved by enlarging coils' size or increasing coils' turns, coils are not allowed to be infinitely large because of the strict limitations on the coils' size in practical applications. The performance of a pair of charging coils is commonly assessed by their coupling effect with a certain air gap or horizontal misalignment between the two coils when their sizes are limited.

2.5.1. Traditional Structures

In most of the wireless charging systems proposed in 1990s and early 2000s, the charging interfaces were developed from the conventional transformers. For example, the E- and U-core structures are derived the ones used for building conventional transformers. The design process of the cores for the charging interfaces also follows the standards of building transformers. In order to improve the coupling effect, the cross-sectional area of the core is maximized. However, the coupling effect of transformer-structure cores is susceptible to the horizontal misalignment because the distribution of the vertical coupling flux is strongly limited by the core. The design based on transformer-structure cores has acceptable performances only if the charged vehicle is in positions where the transmitting and receiving coils are strictly aligned [79, 80]. For instance, the *Korea Advanced Institute of Science and Technology* (KAIST) developed an online electric vehicle system for electric buses [74], in which the structures with EE- and UU-cores are applied, as shown in Fig. 2.7. The researchers also increased the system tolerance to air gap by reducing the width of core poles. But the max-allowable horizontal misalignment is still low (lower than a quarter of the length of primary pad). Furthermore, problems of weight and cost limit practical applications of the structures.
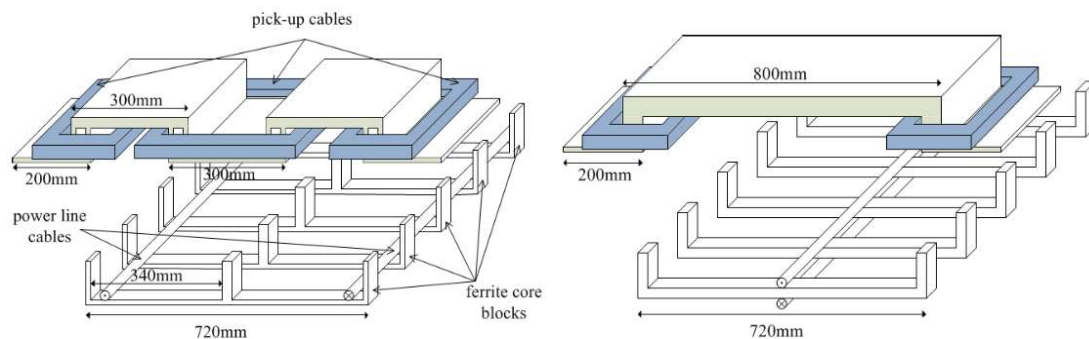
Fig. 2.7. EE- and UU-core structure for wireless charging by KAIST [74].

2.5.2. Plane-core Structures

Most of current research applies plane-core structures for charging interfaces (also known as pads). Plane-core structures are more aesthetic than traditional structures. More importantly, plane-core structures have higher tolerance to horizontal misalignment. As shown in Fig. 2.8, two types of plane-core pads are most commonly used in the inductive charging: the non-polarized pads, such as circular pads (CP) or square pads (SP), and bi-polarized pads (BPP) such as Double-D or Double-D Quadrature pads (DDQP) [8, 50, 65, 75, 81-86]. In Fig. 2.8, the cores of plane-core pads can be formed by ferrite bars (green parts) or air. Litz-wires (purple parts) or printed-circuit-board (PCB) traces can be used to carry AC currents [50, 76]. An aluminum plate (blue parts) can be used to stop flux from
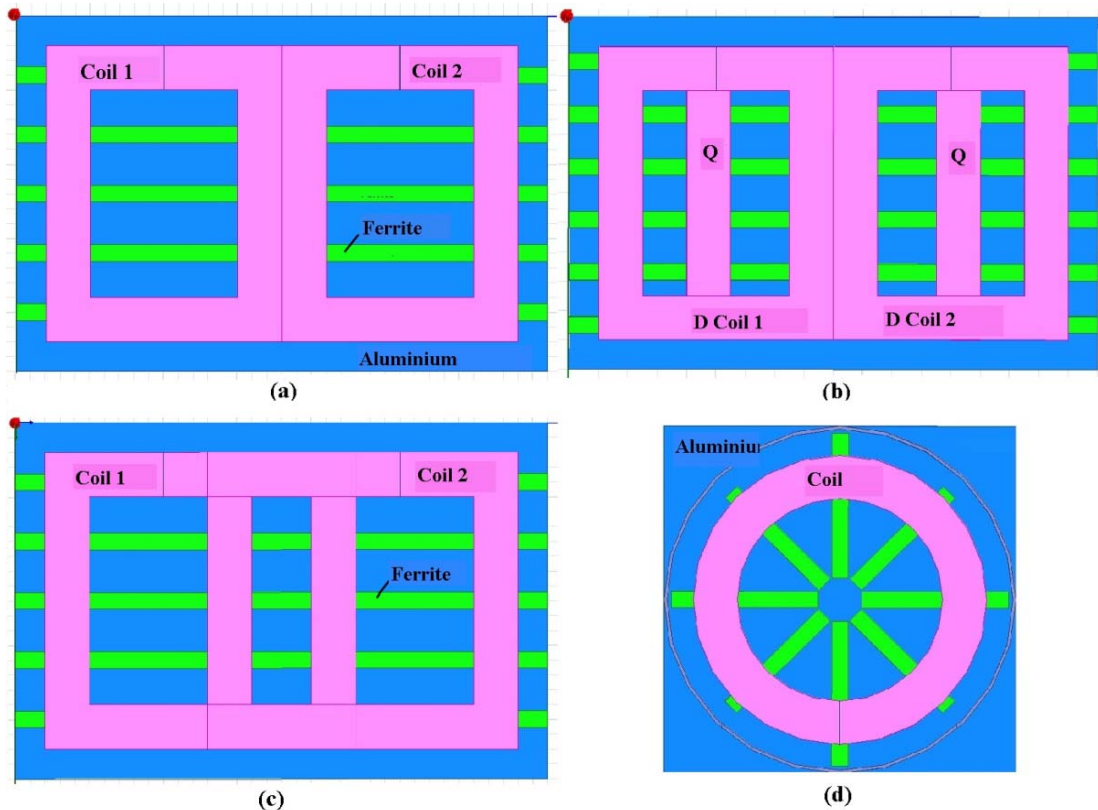
Fig. 2.8. Models of (a) Double-D Pad (DDP), (b) Double-D Quadrature Pad (DDQP), (c) Bipolar Pad (BPP) and (d) Circular Pad (CP).

passing through the pad and influencing the system behind the pad.

Non-polarized designs, such as CPs or SPs, are derived from pot cores and by far the most commonly used structures in EV charging. The basic structure of a CP consists of an Al-plate, a coil, a coil former, ferrite bars and a metallic ring surrounding the pad. This structure generates a single-sided flux path. The ferrite bars force the flux under coils to flow along the radius. Additionally, the metallic ring surrounding the pad reduces the leakage flux. The structure of SPs is similar to that of CPs. Thus, a non-polarized pad generates a symmetrical magnetic field around the pad center. The symmetrical flux distribution limits its practical applications. Because a uniform magnetic field cannot be maintained when the horizontal misalignment between two non-polarized pads increases, the power-transfer capability and efficiency of the system are reduced. Research has demonstrated that tolerance to air gaps and horizontal misalignments between non-polarized pads can be improved by enlarging the size of coils and the number of turns.

For polarized pads, a BPP consists of two identical, partially overlapped, and mutually decoupled coils with one side of the coils sitting next to a ferrite structure and the other side facing the coupled pad. The structure of a DDP is the same as that of the BPP, except that the two coils are placed next to each other rather than overlapping. Each coil of a polarized pad couples with a coil of another polarized pad. The generated magnetic field on a pad flows along the longer edge of the pad. In a DDQP, an extra coil called Quadrature coil (Q-coil) is added to a DDP to achieve higher tolerance to horizontal misalignments. DDQPs have independent tuning and control of the series-connected DD coils and the Q-coil. Research proves that DD coils have a higher power-transfer capability and a wider horizontal charging range. The added Q-coil can be turned

on to couple with another pad when the horizontal displacement increases to be large enough [87]. However, some problems limit practical applications of a typical polarized pad. In polarized pads, the proposed higher tolerance to horizontal misalignments only exists along the long edge of the pads. No improvement of tolerance to horizontal misalignments is achieved along the short edge of the pads. More seriously, magnetic simulations show that the flux in one coil of the receiving pad will be seriously impacted when the wrong coil with the inverse polarity is moved to a position where the transmitting pad partly faces the receiving pad.

2.5.3. Design Considerations

To design a charging pad for inductive charging, comparisons of the characteristics among different types of structures are made. The tolerance to the horizontal misalignments and air gaps between the coupled pads is the most important factor to evaluate. A better design of charging pads generate a better coupling effect with the same misalignment and air gap. On the other hand, the nominal voltages and currents of an IPT system require a specific voltage vs. the frequency and the duty cycle, which is determined by the self-inductances of the pads. Thus, the self-inductances are designed according to the nominal voltage gain. In pads' design, coil turns, shape, dimensions, and core materials determine the self- and mutual inductances (coupling effect) of pads. The self-inductances of charging pads should be limited because a larger inductance leads to a higher voltage on the resonant capacitors. Therefore, the maximum allowed self-inductance of a pad limits the turn number of the coil and the application of ferrite bars. With the plane-core structure, the self-inductance of a pad can be reduced by placing multiple layers of parallel-connected coils. The design specifications of the proposed

31

pads can be estimated by theoretical calculations and magnetic simulations before building the hardware.

Besides optimizing the design of charging interfaces, some other methodologies for improving magnetic coupling between pads are proposed. A mechanical method can be applied to reduce the air gap between coils. For example, in [88], the system includes a primary coil and a wheel chock structure. The proposed system raises the primary coil automatically to align with the secondary coil when a tire enters the wheel chock. A practical application containing a pair of orthogonally placed primary and secondary coil arrays is shown in Fig. 2.9 [89]. In Fig. 2.9, the charging system selects two individual coils from each of the coil arrays separately, and the chosen two coils face directly to each other. Thus, the optimal magnetic coupling can be maintained. However, these methods need a system to track coil positions and conduct mechanical control. The overall cost is dramatically increased.
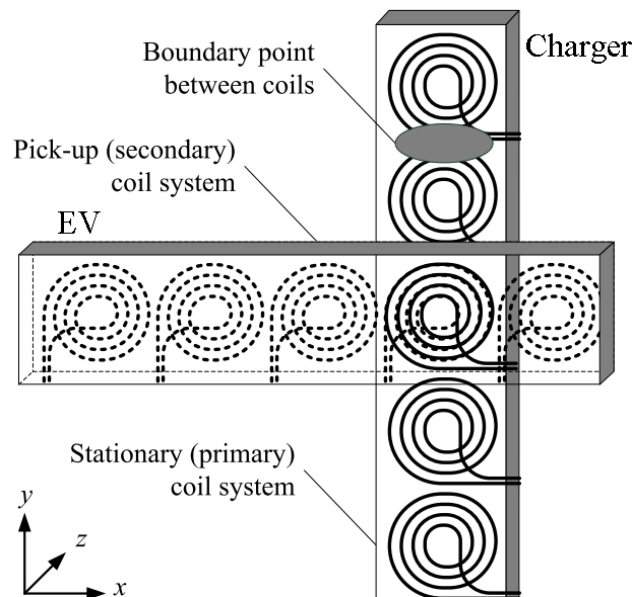
Fig. 2.9. Schematic of coils arrangement of a system with two orthogonal coil arrays.

2.6. Design of On-board Chargers

Nowadays, Levels 1 and Level 2 EV charging systems are most commonly used. In Level 1 and Level 2 charging standards, an on-board charger is required. The chargers on the primary side acquire power from home-used outlets and on-board chargers generate the charging voltage and current (V&I) to EV batteries [1, 41, 90-94]. For wireless charging applied in EVs, the electrical characteristics are more susceptible to the impact of the environment. Therefore, on-board equipments should be installed on EVs for regulating the charging V&I.

In most of the current research on wireless charging for EVs, the proposed on-board charger consists of a diode-rectifier and a low-pass filter for initial AC-DC conversion, and a DC-DC converter regulating charging V&I to EV batteries. The on-board charger should be designed so that the on-board charger is capable of providing stable charging V&I to the EV battery system and coordinating with the primary charger for more adaptive and efficient charging. Similar to the research of UIC, the relevant research of on-board chargers focuses on the design of *LC* circuits, the control method, receiving pads, and so on. Based on the concept of universal charging, on-board chargers with both series-connected and parallel-connected *LC* circuits are analyzed. The DC characteristics of the two types of *LC* combinations should be suitable for the control of the proposed UIC. In addition, the control method of the proposed on-board chargers should cooperate with the primary charger even there is no wireless communication between the two sides. The proposed control of on-board chargers is related to the control of the UIC and electrical characteristics of the system. The charging interfaces of the proposed on-board chargers should have the same structures as that of the UIC. A

33

comprehensive design process should be summarized as a standard of on-board chargers used in universal inductive charging.

2.7. Single-Phase vs. Three-Phase Systems

Most of current research on inductive charging employs single-phase structures. The main reason for choosing single-phase structures is from the power levels of the inductive-charging applications. According to the limitations on the efficiency and the power-transfer capability of an inductive charging system, the power level of inductive charging is commonly limited in 20 kW. However, some researchers proposed the concepts of three-phase inductive charging systems [84, 95-98]. The basic structure of a three-phase WPT system is shown in Fig. 2.10. According to the applications of

(a)

(b)
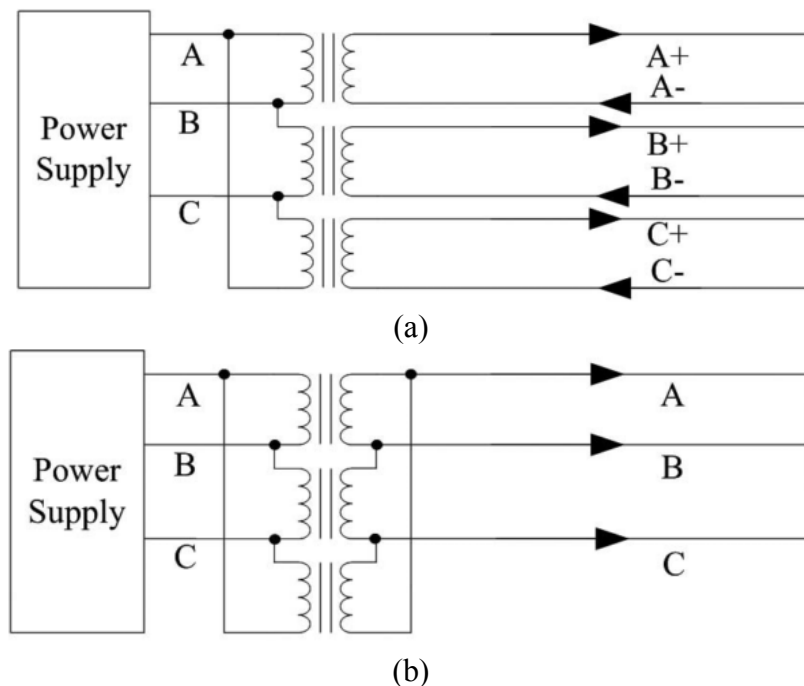
Fig. 2.10. (a) Bipolar three-phase system with an open-delta output transformer and (b unipolar three-phase system with a closed-delta output transformer.

conventional high-frequency transformers, three-phase transformers are a good alternative in a higher power range (> 100 kW) because of a smaller core size and great electromagnetic-compatibility (EMC) benefits. By theoretical analysis, three-phase inductive charging owns some specific advantages. For example, in [84], a three-phase inductive charging system is employed in roadway-charging applications because of a wider power delivery zone and its capability of continuous power transfer without on-board batteries. In [96], a three-phase system is proposed for reduced total harmonic distortions (THD) in resonant circuits and lower electromagnetic force (EMF) of leakage flux, which is harmful to animals nearby.

To the best knowledge of the author, all of the current three-phase inductive charging systems are only theoretically analyzed and there are still some serious problems limiting the practical applications. Horizontal misalignments between the coils on the two sides seriously influence the magnetic field and unbalance the currents in the three coils of the receiving pad. The unbalanced currents in the coils require an extremely complicate control method to help stabilize the output, because the mutual coupling among a coil on one side and three coils on another side varies randomly. The low coupling among the coils aggravates the imbalances. In fact, undesirable system performance will be caused by a small difference between any two coils on the same side, let alone the different magnetic coupling effects among the coils [84]. On the other hand, when the size of a charging pad is limited, the optimal design of a coil is a single and largest coil because the highest coupling effect can be achieved. The analysis is similar as the comparisons between a polarized pad and a non-polarized pad. Finally, the household power (mains electric power) is single-phase electric power in many countries, including

USA. The universal applications of single-phase power require a three-phase DC-AC inverter generate the AC power, which increases system cost a lot. As a result, this dissertation focuses on analyzing a single-phase inductive charging system.

2.8. Power Losses and Efficiency Analysis

Efficiency is one of the most important parameters for evaluating the performance of an IPT system. Previous research performs a comprehensive analysis on power losses of an IPT system. As shown in Fig. 2.11, .the calculations of power losses and efficiency analysis are conducted from the first-stage DC power supply to the final DC output that feeds to EV batteries. The power losses of an IPT system are mainly consumed by the full- or half-bridge DC-AC inverter on the primary side, the parasitic components of coils, the undesired magnetic coupling effect, the on-board AC-DC converter, and the control systems of the inverters and converters.

The power losses of the DC-AC inverter and on-board AC-DC converter have been thoroughly analyzed by previous research [67, 99, 100]. The switching losses and conduction losses by diodes and switches (MOSFETs or IGBTs) are the main power losses. Soft-switching operation (ZVS and ZCS) can be applied to improve the system efficiency by eliminating the switching loss [43, 52, 101]. The emerging wide-band-gap devices such as SiC diodes and MOSFETs can be applied to reduce the power losses in high-frequency applications [102, 103].

Current research focuses on analyzing the power losses caused by coils [52, 104, 105]. As shown in Fig. 2.11, resistance r_1 and r_2 are the equivalent resistances to represent the power losses caused by the parasitic resistances of the coils and the
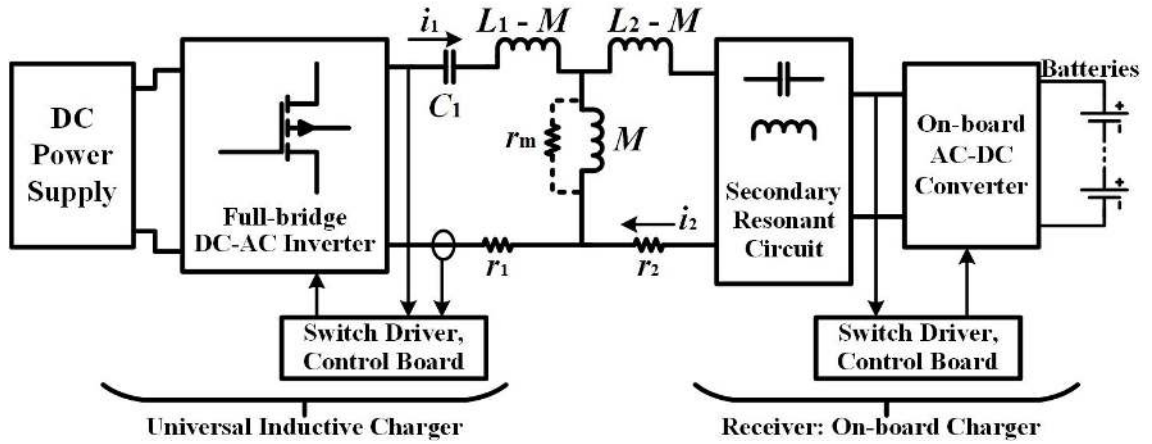
Fig. 2.11. IPT system structure used for analyzing power losses.

magnetic core losses. To reduce the power losses by r_1 and r_2, litz wires are commonly

used because the skin effect in high-frequency operation is significantly mitigated.

Moreover, a tighter coupling effect between the coils helps reduce the power losses by r_1

and r_2. When the input current i_1 is constant, a higher mutual inductance reflects higher

impedance from the secondary side to the primary side. Therefore, less percentages of the

input power can be consumed by r_1. In another aspect, the equivalent resistance r_m

represents the power loss caused by undesirable magnetic coupling. For example, the

primary coil can be coupled with the metallic elements in the hardware on the secondary

side or some other objects in the surrounding areas. The value of r_m is difficult to

accurately evaluate. Some research uses a model with series-connected r_m and M, in

which case the equivalent resistance r_1 and r_2 are changed to ($r_1 - r_m$) and ($r_2 - r_m$). An

important parameter to evaluate the performance of a coil is the quality factor:

$$Q_{coil} = \omega L / r ,\qquad(2.8)$$

where ω is the AC frequency, L is the self-inductance, and r is the parasitic resistance of

the coil. Obviously, a higher quality factor Q_{coil} means higher percentage of the power is

37

stored in the inductor but not consumed by the resistance. Thus, a higher Q_{coil} leads to a higher efficiency when the current is the same. Q_{coil} is also determined by ω. The efficiency can be increased by employing higher AC frequencies. The efficiency improvement by increasing the frequency is obvious when the coupling effect is very low ($k < 0.1$). However, increasing the AC frequency may decrease the power factor of the entire system and increase the parasitic resistances of the coils.

The power consumed by the control system should be considered during efficiency test, although it is just a tiny part ($< 0.5\%$) of the overall power loss. In practical applications, batteries' heating is also a kind of power loss.

2.9. Summary of Current Research

In summary, the current research on IPT systems includes the design of the primary and secondary resonant circuits, the charging interfaces, and the control strategies. The previously proposed systems have applied various designs and control methods to solve the common problems existing in the inductive charging such as the varied magnetic coupling between the charging pads. Various circuit topologies with different L and C connections and combinations, such as *LC*, *LCL* and *LCC* resonant circuits, have been analyzed for their pros/cons and specific applications. The systems with different resonant circuits applied control strategies that are determined by the electrical characteristics of the *LC* circuits, for which the PWM and variable-frequency control are the most commonly used schemes. The design of resonant circuits and the applied control strategy are optimized based on a stable output, high efficiency, and the functions for the specific applications. For the design of charging interfaces, most of the recently proposed IPT systems apply the plane-core structure. Although the polarized

interfaces have certain advantages, the non-polarized pads are more commonly used in practical applications.

However, previous research does not propose an effective or adaptive method to solve the practical problems of the system instability caused by varied magnetic coupling. Instead, most of previous research focuses on optimizing the system based on the charging conditions with a small range of coupling effects or a relatively fixed load, No previous research analyzes a universal inductive charger that is capable of charging different EVs with various designs of receiving pads and secondary *LC* circuits. Moreover, additional wireless communications applied by previous research increase the complexity and cost of the system. As a conclusion, the literature of the previous research on the IPT systems indicates that the design of a universal inductive charging system has not been achieved yet.

In the dissertation, the proposed universal IPT system consists two parts: the proposed UIC on the primary side and the on-board charger on the secondary side. System designs are analyzed three aspects and the analysis mainly aims at realizing the universality of the charging system. The main challenges for designing a universal inductive charging system are varied magnetic coupling between the charging pads in practical applications and various designs of secondary *LC* circuits and receiving pads. A universal inductive charging system is proposed to solve these practical problems. Comprehensive descriptions of the proposed system are present in the following Chapters.

CHAPTER 3: DESIGN OF A UNIVERSAL INDUCTIVE CHARGER

3.1. Overview

In this Chapter, the design process of a universal inductive charger (UIC) for EVs is proposed. The proposed UIC is capable of adaptively providing a constant or controllable charging voltage to various EV models with different *LC* circuits and a wide range of varied magnetic coupling between the transmitting and receiving pads. The charging efficiency is maintained high in various conditions.

According to the basic structure of an inductive charger and the definition of universal inductive charging, three aspects of the design are analyzed, including the topologies of resonant circuits, the control method for the DC-AC inverters in the inductive charger, and the design of the charging interfaces. When the inductive charger is designed with an S-connected *LC* circuit and the AC frequency is varied to be at the fixed-gain point, a stable output voltage vs. magnetic coupling effects or load conditions can be achieved. Meanwhile, ZVS of the primary DC-AC inverter is universally achieved in every charging cycle with different coupling effects. Based on the DC characteristics of the Series-connected *LC* circuit, a simple yet effective control method based on frequency variations is used to automatically track the optimal frequency in different coupling conditions and adjust the frequency during the charging process. The design of the charging interfaces is also optimized with a higher efficiency and a higher power-transfer capability. Simulations and prototypes validate that the proposed UIC is accurate, robust, and applicable.

Section 3.2 compares different resonant circuits with each other and proves that the S-connected *LC* is the optimal topology because of a constant charging voltage vs. the load and maintains higher efficiency during every charging cycle. Section 3.3 proposes an effective and universal control method to track the optimal AC frequency and adjust the frequency during the charging process; wireless communication is not necessary. Section 3.4 analyzes different structures of the charging pads and demonstrates that a square pad with perpendicular flux has a better coupling effect and a higher efficiency when the overall size of the pad is limited in practical applications. In Section 3.5, experiment results by a prototype are used to test the applicability of the proposed UIC design. Finally, Section 3.6 summarizes the proposed design of the UIC and its contributions.

3.2. Resonant Circuits of the Universal Inductive Charger

By circuit analysis, the only connection between the primary side (the charger) and the secondary side (the charged EV) is the mutual inductance between the primary and secondary inductances. However, the mutual inductance is varied by the air gap and horizontal misalignment between the transmitting and receiving coils. For a UIC, the first aim is to provide stable and controllable power to the load through the two *LC* resonant circuits, even with a wide range of varied mutual inductance. Another challenge for the UIC is from the different design characteristics in various models of EVs, including coils (inductances), resonant capacitances, and so on. A UIC should be capable of charging in various EVs with various secondary circuits. As a result, an optimal topology of the primary *LC* circuit should be selected, to make sure that any load gets a constant voltage during each charging cycle, even the mutual inductance is varied in different charging

cycles, or the secondary *LC* circuits in various loads are series or parallel connected, or the secondary inductances are different.

3.2.1. S- or P-Connected LC Circuits

In a typical IPT system, there are four common topologies of resonant circuits. The characteristics of S- and P-connected *LC* circuits have been analyzed in [13, 24]. The resonant frequency is commonly chosen as the optimal AC frequency by a lot of previous research. In practical applications, the charger with a P-connected *LC* circuit has some disadvantages, such as high turn-off currents and a non-zero load reactance. These problems decrease the efficiency and influence the tuning of the *LC* circuits [13, 24, 75]. The S-connected circuit is preferred, for its easier tuning in long-track applications, a relatively fixed value of resonant capacitance vs. various mutual inductances, and good harmonics reduction in loosely-coupling conditions [24, 25]. Moreover, the adaptive control method based on electrical characteristics of resonant circuits is also required to achieve universal charging. The tuning of a P-connected *LC* circuit depends on both the magnetic coupling effect and the load. An S-connected *LC* circuit works as a constant-voltage source in every charging cycle, without influence from the load. In practical applications of Levels 1 and 2 charging, EVs have on-board AC-DC converters to control the charging voltage and current [1]. Moreover, common on-board converters prefer a constant voltage input. Thus, a model of constant-voltage source is a better choice for the combination of the primary and secondary *LC* circuits.

The circuit analysis of the IPT system is based on the mutual-inductance model shown in Fig. 3.1, where L_1 and C_1 are the primary inductance and capacitance, L_2 and C_2 are the secondary inductance and capacitance, M is the mutual inductance between L_1 and

L_2, R_{load} is the equivalent resistance of the load, and r' is an equivalent resistor simulating the power loss caused by flux leakage or undesired coupling. The DC characteristics of the resonant circuits, including the voltage gain and the equivalent load-phase angle vs. the AC frequency, can be calculated. The defined voltage gain is

$$G = \left| V_{out} / V_{in} \right|,$$

where V_{in} is the input voltage of the primary LC circuit and V_{out} is the output voltage of the secondary LC circuit. The equivalent load-phase angle is the phase angle of the equivalent impedance looking from the input of the primary LC circuit. In the SS topology, the equivalent impedance is

$$Z_{total} = 1/(j\omega C_1) + j\omega L_1 + \omega^2 M^2 / (j\omega L_2 + 1/(j\omega C_2) + R_{load}). \tag{3.1}$$

In the SP topology, the equivalent impedance is

$$Z_{total} = \frac{1}{j\omega C_1} + j\omega L_1 + \omega^2 M^2 \Big/ (j\omega L_2 + (\frac{1}{j\omega C_2} \| R_{load})). \tag{3.2}$$

Assume the resonant frequencies of both sides are equal, as

$$\frac{1}{\sqrt{L_1 C_1}} = \omega_0 = \frac{1}{\sqrt{L_2 C_2}},$$
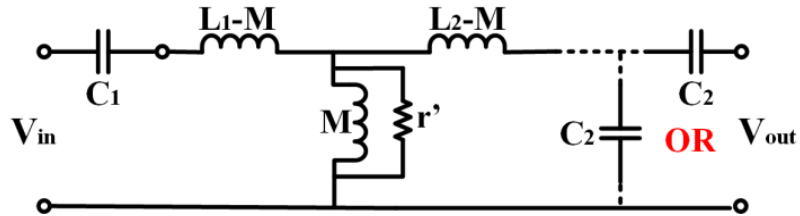
Fig. 3.1. The equivalent topology with an S-connected primary LC circuit.

When the load contains an S-connected *LC* circuit, the simulated DC characteristics (by Simulink) of the SS topology in a single charging cycle is shown in Fig. 3.2(a). The parameters used in simulations are listed in Table 3.1. The following conclusions can be drawn.

1) The voltage gain is not fixed at the resonant frequency f_0 in various load conditions and can be extremely high with a light load.

2) When M is fixed, the curves of the voltage gain in varied load conditions (R_{load} varies) go through a fixed-gain point (the unity-gain point when $L_1 = L_2$) at the frequency f_1. Z_{total} is inductive beyond f_1 (the input voltage leads the input current), leading to the ZVS operation (turn on) of the primary DC-AC inverter. The existence of the fixed-gain point is not influenced by "bifurcation". Although Z_{total} is kept purely resistive at the resonant frequency f_0, the system with the frequency f_1 provides a much more stable output voltage: a constant voltage gain not influenced by varied load resistance. This also means that the transferred real power is not influenced by mutual inductance M when the AC frequency is f_1, according to $P = V^2/R$.

Table 3.1. Parameters in Simulations of LC Circuits

Parameters	Values
Primary L_1	199.5 µH
Primary C_1	20.87 nF
Secondary L_2	200.8 µH
Secondary C_2	20.73 nF
Mutual M	40 µH
Load R_{load}	10, 15, 20, 25, 30, 35, 40, 50, 60, 80, 120 Ω
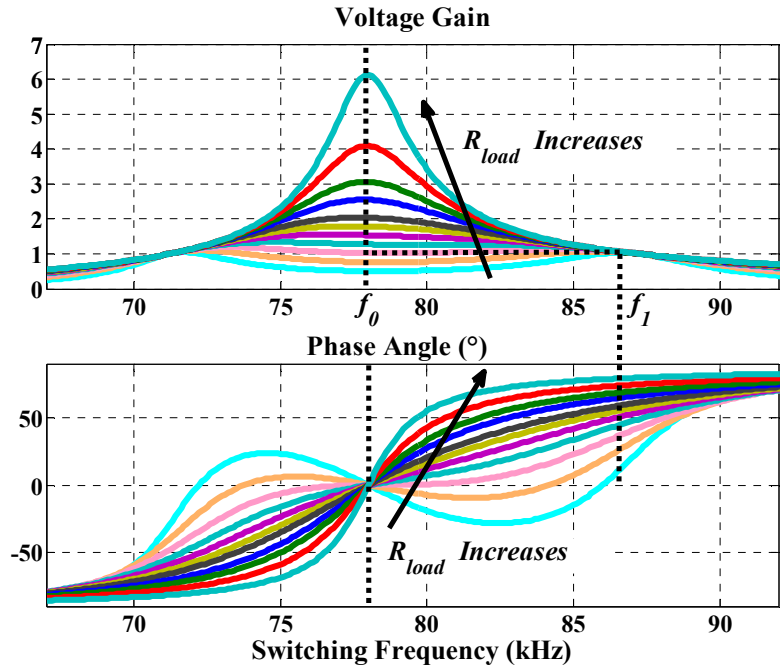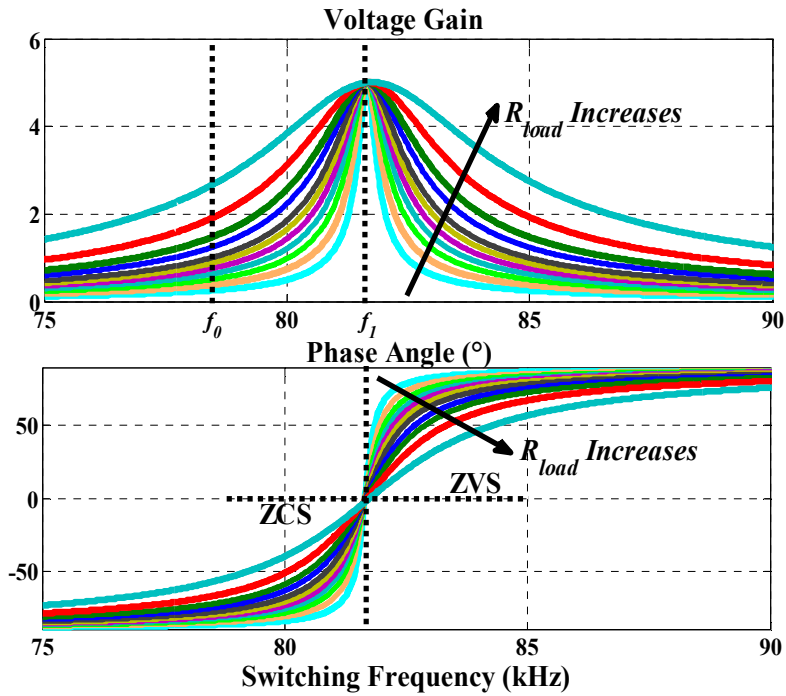
Fig. 3.2. Simulated DC characteristics: the voltage gain and load-phase angle vs. the AC frequency in (a) the SS-connected and (b) the SP-connected *LC*, based on the simulation parameters listed in Table 3.1.

45

3) The voltage gain at the fixed-gain point is determined by the values of the primary and secondary inductances, as

$$G = \sqrt{L_2 / L_1} \; . \tag{3.3}$$

4) The frequency at the fixed-gain point f_1 is influenced by the mutual inductance and can be calculated by

$$f_1 = \sqrt{\frac{\sqrt{L_2}}{C_1(L_1\sqrt{L_2} - M\sqrt{L_1})}} \Big/ 2\pi = \sqrt{\frac{1}{(1-k)}} \cdot f_0 \; . \tag{3.4}$$

From the condition that R_{load} becomes $+\infty$ and the curve of voltage gain still passes through the fixed-gain point:

$$G = \sqrt{\frac{L_2}{L_1}} = \frac{j\omega_1 M}{j\omega_1 M + j\omega_1(L_1 - M) + \dfrac{1}{j\omega_1 C_1}} \; .$$

5) For each curve of the load-phase angle with any load level, there is one zero-crossing point between the resonant frequency and the fixed-gain point.

Thus, if the frequency is set to be f_1, the primary inverter will keep working with ZVS during the charging process. The voltage gain G will be maintained constant during the charging process, which is much easier for the on-board AC-DC converter to regulate the charging voltage, current and power. The value of f_1, higher than the resonant frequency f_0, can be tracked by measuring the zero-crossing point of the load-phase angle vs. frequency. Note that the analysis is based on the assumption that the resonant frequencies determined by the L's and C's of the primary and secondary resonant circuits

are the equal or close to each other. A reasonable idea for EV manufacturers is setting the secondary *LC* circuits with the equal resonant frequency as the inductive charger. EV manufacturers can select an appropriate value of the self-inductance of the receiving coil first, and choose *C* accordingly, by (1). Because an under-research standard (SAE J2954) limits the AC frequency used in wireless charging of EVs (81.38 ~ 90 kHz), each EV is proposed to work with the AC frequency in the specific range. The standard also requires the proximity of the resonant circuits on EVs to the primary resonant circuit of the charger, in the frequency settings. Also note that the preset resonant frequencies of the charger and EVs are not necessary to be in the standard range, but their working frequency is. The assumptions for the simulations in Fig. 3.2 are reasonable, as the resonant frequencies of the *LC* circuits on both sides are of the same value and the AC frequency is limited in the standard range. As the voltage gain with f_1 is determined by the self-inductances of the transmitting and receiving pads, EV manufacturers should set the value of L_2 according to the specific voltage requirements of their EVs.

When the load contains a P-connected *LC* circuit, the simulated DC characteristics of the SP topology are shown in Fig. 3.2(b). Similar to the SS-connected *LC* circuits, a fixed-gain point exists at the frequency f_1. All of the voltage-gain curves pass through the fixed-gain point at f_1, no matter what the value of R_{load} is. As shown in Fig. 3.2, the voltage gain at the fixed-gain point can be calculated by

$$G = L_2 / M .\qquad(3.5)$$

The according value of f_1 at the fixed-gain point is also determined by the mutual inductance *M*, as

$$f_1 = \sqrt{\frac{L_1}{C_2(L_1L_2 - M^2)}} \Big/ 2\pi = \sqrt{\frac{1}{(1-k^2)}} \cdot f_0 . \tag{3.6}$$

The zero-crossing point of each load-phase-angle curve is slightly higher than f_1. If the frequency is f_1, Z_{total} will be capacitive during the whole charging process, because the load-phase angle is slightly lower than 0. If the frequency is slightly higher than f_1, ZVS can be achieved. From the curves of the voltage gain, the voltage gain is sensitive to the frequency variance (the slope $\Delta G/\Delta f$ can be higher than 6/V). Because of the limitation on the voltage gain, the frequency must be carefully controlled.

Hence, compared with P-connected LC circuit, the S-connected LC circuit is much more suitable for universal charging. The S-connected LC circuit is capable of charging different types of EVs with a higher efficiency, a stable output voltage, and easier operations, for the following four reasons.

1) For the primary inverter with an S-connected LC circuit, the voltage gain G at the fixed-gain point is maintained constant during the charging process, performing as an ideal input for the on-board AC-DC converter.

2) For the primary inverter with an S-connected LC circuit, if the frequency is set as the fixed-gain point f_1, ZVS is continuously maintained during the charging process.

3) The fixed-gain point always exists, if the resonant frequencies determined by LC circuits of the charger and the charged EV are equal or nearly equal. Meanwhile, the optimal frequency is fixed during a specific charging cycle and can be found by detecting the load-phase angle, although the frequency f_1 is varied by the mutual inductance.

48

4) For each curve of the load-phase angle, there is one zero-crossing point beyond f_0. The single zero-crossing point means that the fixed-gain point can be easily tracked by seeking from f_0 to higher values until the load-phase angle becomes 0. Thus, the control the inductive charger can be done without wireless communications between the two sides.

3.2.2. Series-Connected LC or LCC Circuits

Another popular topology applied in inductive charging is the *LCC* circuit, as shown in Fig. 3.3, where L_{1s} is the added S-connected inductor, C_{1p} is the additional parallel connected capacitor, the C_{1s} is the resonant capacitor with L_1, and Z_r is the reflected impedance from the secondary side to the primary side. Combining advantages of S- and P-connected *LC* circuits, an *LCC* circuit has a constant output current independent of load and a narrow switching frequency range [15, 38, 45]. But an *LCC* circuit has to work in the ZCS mode to acquire the ideal output, because the ZVS can only be realized at the negative slope of the curve of the voltage gain vs. the frequency, meaning an unreasonably large range of the optimal frequency vs. the load. However, in a high-frequency inverter using MOSFETs, the ZVS (ZVS turn on) mode is more efficient and safer than ZCS for lower turn-on losses and avoiding high current stress, especially when the input voltage is high [29, 106]. Moreover, for universal applications, system may adjust the frequency to acquire the voltage gain in a typical range, like 0.5~2. In this condition, an S-connected *LC* circuit only needs to vary the frequency in a smaller range than the *LCC* circuit. On the other hand, more resonant components used in the *LCC* circuit lead to more energy stored in the inductors and capacitors. This generates more power loss by parasitic elements in the resonant components. In summary, the *LCC*
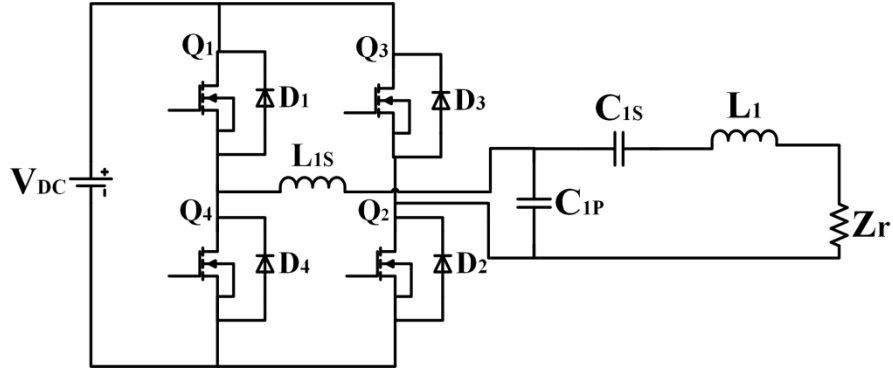
Fig. 3.3. Equivalent model of an inductive charger with *LCC* circuit.

circuit can rarely achieve the stable output and a higher efficiency in ZVS mode at the same time.

3.2.3. Existing Problems with a Series-Connected LC Circuit

For the UIC with an S-connected *LC* circuit, some problems need to be solved before realizing "real" universality. A problem is the high percentage of reactive power in a light load (low power factor), when the load contains an S-compensated *LC* circuit and the frequency is set to be f_1. High percentage of reactive power usually leads a lower efficiency. Meanwhile, a strict requirement of the power-factor-correction is put on the DC converter in front of the primary DC-AC inverter. Accordingly, the UIC could adjust the frequency to a lower value to reduce the reactive power. Note that the reduction cannot be too large because of the limitation on the AC frequency.

Another problem is about the detection of f_1. Because the variances of the AC frequency have an obvious influence on the output voltage and the load-phase angle, a small error of the frequency generates an undesirable variance of the output. Thus, an accurate control method is required for tracking f_1. An effective algorithm to distinguish the topology of the secondary *LC* circuit is also helpful.

50

3.3. Design of the Universal Control Loop

There is an AC source generating the high-frequency AC power (normally in the range of 20~200 kHz) to the primary LC resonant circuit. The main function of the AC source includes converting the AC from the grid to a stable DC output while doing PFC, and then generating a high-frequency AC to the following LC circuit by the designed control methods, summarized as the AC-DC-AC conversion. This paper concentrates on the control of the primary AC power source and the coordination between the inductive charger and the load. The AC source in an inductive charger is a full-bridge DC-AC inverter, which is commonly controlled by the Sinusoidal-Pulse-Width-Modulation (SPWM). SPWM is applied to modulate the duty cycle of the switching signals with a fixed frequency. However, SPWM is not the focus here. SPWM can be used as the auxiliary method. In fact, when the AC frequency is higher than 80 kHz, the V&I sensing on the LC circuits is difficult because of the speed limitation of sensors or analog-to-digital converters (ADC). This strongly limits PWM application in modulating the resonant circuits. Therefore, the variable-frequency control would be preferred. The PWM (with PFC) can be operated in the AC-DC converters on the primary side to regulate the input voltage or on the secondary side to control the charging current. As a result, the default duty-cycle is set to be 50% in this paper.

The main focus of this section is the variable-frequency control for universal charging. In a typical charging process, the UIC automatically tracks the optimal frequency before the charging process begins and adjusts the AC frequency during the charging process if necessary. According to the previous analysis, the frequency at the fixed-gain point f_1 is chosen as the optimal AC frequency.

51

3.3.1. Control Process

A few methods have been proposed on searching for f_1. For example, a typical method proposed in [53] searches from a pre-set higher frequency f_2 to the resonant frequency f_0 to acquire f_1. However, all of these methods need auxiliary components and wireless-communication devices [16, 46, 53].

For universal charging, an easier and faster method of tracking f_1 is proposed, as shown in Fig. 3.4. The method is based on the curves of the DC characteristics shown in Fig. 3.2. At the beginning of charging, the AC-DC rectifier in the UIC provides a low input DC voltage V_{start} to the DC-AC inverter (lower than the full-input voltage). The UIC adjusts the AC frequency from f_0 to higher values step by step (increasing step = Δf) while measuring the load-phase angle θ between the input voltage and current. According to the load-phase-angle curves shown in Fig. 3.2, the fixed-gain point (f_1) is tracked when
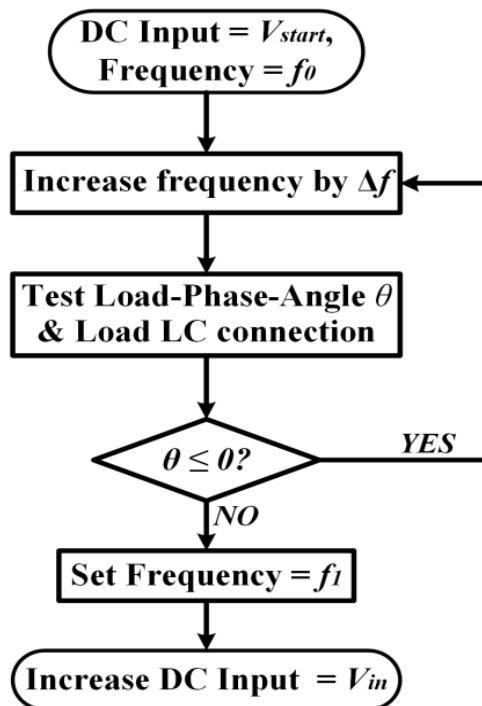
Fig. 3.4. Flow-chart of the proposed control method for tracking f_1.

the angle θ is above zero. Finally, the UIC sets the AC frequency to be f_1 and increases the input DC voltage to the nominal input voltage V_{in}. Thus, the output voltage of the secondary LC circuit (or the input voltage of the on-board AC-DC converter) is maintained constant during the whole charging process, according to the specific ratio of V_{out} to V_{in} at the fixed-gain point. In practical operation, the variance of the AC frequency during the charging process influences the power distribution in LC circuits and the power flow between the two sides. Unreasonably fast variance of the frequency generates instability and power emissions in high-power applications. Thus, each step of frequency variance must be of a small value and the interval between every two steps must be long enough for the system to reach stability.

The control system determines the LC connection in the load by a similar method, without using wireless communication between the charger and EVs. When the frequency is the resonant frequency f_0, the load-phase angle θ of the system with an S-connected LC circuit in the load is different from the system with a P-connected LC circuit in the load. The angle θ is zero at f_0 when the load contains an S-connected LC circuit, while θ is apparently lower than zero when the load contains a P-connected LC circuit. If the series connection of the LC circuit in the load is detected, the UIC can further adjust the frequency during the charging process to achieve higher efficiency and better charging quality. From the curves of load-phase angle of the SS topology, the power factor (P/S, where P is the real power and S is the apparent power of the system) of the system decreases when the equivalent resistance R_{load} increases. Accordingly, the UIC can decrease the AC frequency to a lower value than f_1, as

$$f = f_0 + (f_1 - f_0)/\eta \ \ (\eta > 1),\tag{3.7}$$

53

when the load-phase angle is large enough (the load becomes light enough). Thus, the power factor increases and the power loss generated by parasitic resistors decreases. Because of the limitations on the input voltage of the on-board DC-DC converter and the standard of the AC frequency, the reduced AC frequency should have a lowest boundary.

3.3.2. Hardware Requirements

To achieve the frequency control, the system should acquire at least the phase angle between the input voltage and current. Hall-effect or other sensors are normally used to detect the voltage and current. However, the standard AC frequency in an IPT system of EVs (higher than 80 kHz) is too high for common hall-effect sensors (commonly lower than 40 kHz) to catch up with the signals in the resonant circuits. Hence, the proposed control system captures the input voltage and current by shunt resistors and applies logic circuits to transfer the phase angle to a constant voltage output, as shown in Fig. 3.5. The way to sense the input voltage and current is shown in Fig. 3.5(a). The sensed voltage signal V_{sense} is acquired by resistive voltage ratio and the current I_{sense} is got by the voltage of the shunt-resistor. The specific structure of the control system for tracking the fixed-gain point (f_1) is shown in Fig. 3.5(b). First, an amplifier and a comparator are used to transfer the sensed voltage or current (V_{sense} or I_{sense}) to a square wave ($V_{V,sense}$ or $V_{I,sense}$) with the same frequency and the same zero-crossing point. Secondly, let the square waves $V_{V,sense}$ and $V_{I,sense}$ go through a logic circuit. The logic circuit generates another square wave V_{XOR} with the width equal to the delay between the $V_{V,sense}$ and $V_{I,sense}$. Thirdly, the RC circuit at the output of the logic circuit transfers V_{XOR} to an average voltage V_{phase} that is proportional to the phase angle. Finally, the control system calculates the phase angle by measuring V_{phase}. According to

the speed limitation of common ADC models, the proposed control system is more practical. It does not need fast measurement to get a certain amount of the voltage or current points in a period [107-109]. The frequency has no influence on the result. There is no mandatory rule on the specific measuring moments.

For more accurate measurement, a voltage offset is placed on the comparator in the branch of I_{sense}. The voltage offset is used to counteract the undesirable phase shift

(a)

(b)
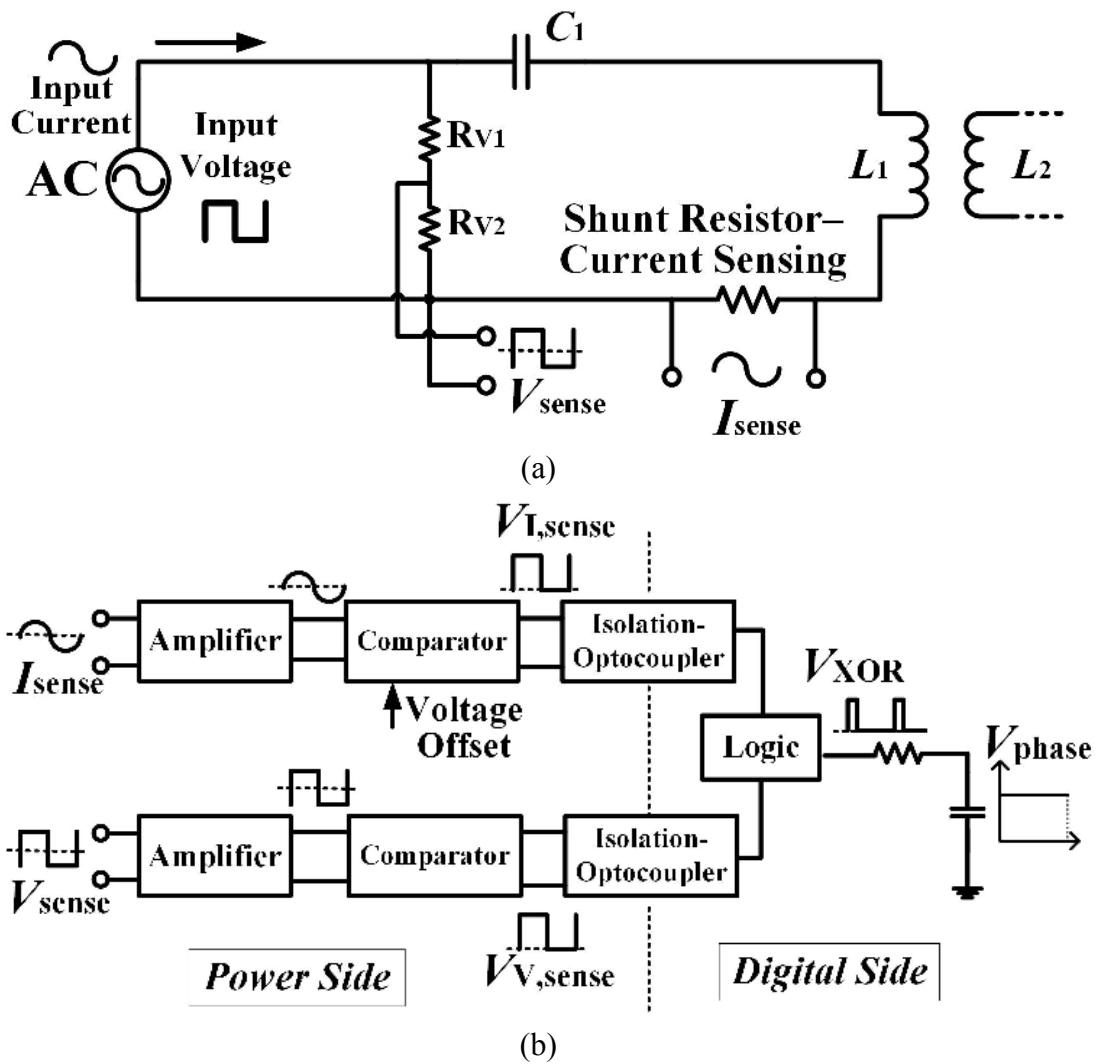
Fig. 3.5. (a) The schematic of sensing the input voltage and current and (b) the schematic of the control system for measuring the load-phase angle.

caused by the parasitic inductances of resistors around the amplifiers (the phase shift leads to inaccuracy of V_{XOR}). To determine the voltage offset, let the input voltage and current be in phase with a standard frequency (85 kHz). Adjust the voltage offset until the detected phase difference V_{XOR} is zero. The error caused by the undesired phase shift can also be rectified in the DSP by adjusting the relevant codes.

3.3.3. Frequency Control in Extreme Cases

For a more comprehensive control strategy, one situation must be taken into consideration that the mutual inductance between coils is of an extremely high or low value. In previous analysis, the frequency f_1 at the fixed-gain point is determined by the mutual inductance, as indicated by (6) and (9). A larger mutual inductance M leads to a higher f_1. Hence, the calculated frequency f_1 may be out of the standard range of the AC frequency, when the mutual inductance between coils is extremely high or low. For example, in the simulation results shown in Fig. 3.2(a), the theoretical value of f_1 shifts out of the SAE standard of frequency range: 81.38 kHz ~ 90 kHz, when the mutual inductance M is lower than 10 μH or higher than 57 μH ($M = 21 \sim 55$ μH when the air gap ranging from 20 cm to 10 cm). As a result, if the optimal frequency f_1 is out of the standard range, the frequency will be forcibly set as the boundary values 90 kHz (M is too high) or 81.5 kHz (M is too low). Similar to the voltage gain after varying the frequency during the charging process, the voltage gain is not fixed when the frequency is set to be the boundary values. But, compared with other frequencies, the boundary values are still the best choices in the extreme cases, because the variance of the voltage gain through the charging process is much smaller than the variance of the voltage gain when the frequency is of other values.

3.3.4. Frequency Control with Non-ideal LC Circuits

The simulations in Fig. 3.2 are based on the fact that the resonant frequency of the

primary *LC* is the same as the resonant frequency of the secondary *LC* circuit. However,

it is possible that the resonant components in *LC* circuits are not ideal because of

components aging or the influence from metallic objects in the surrounding space. The

non-ideal devices may move the range of the practical f_1 to a lower or higher section,

when the range of varied *M* is fixed. For example, when the secondary capacitance in the

simulation of Fig. 3.2(a) increases from 20.7 nF to 21.7 nF, the resonant frequency of the

secondary *LC* varies from 78 kHz to 76.2 kHz. The non-ideal curves of the DC

characteristics are shown in Fig. 3.6. The fix-gain point is moved to a lower value by 0.2
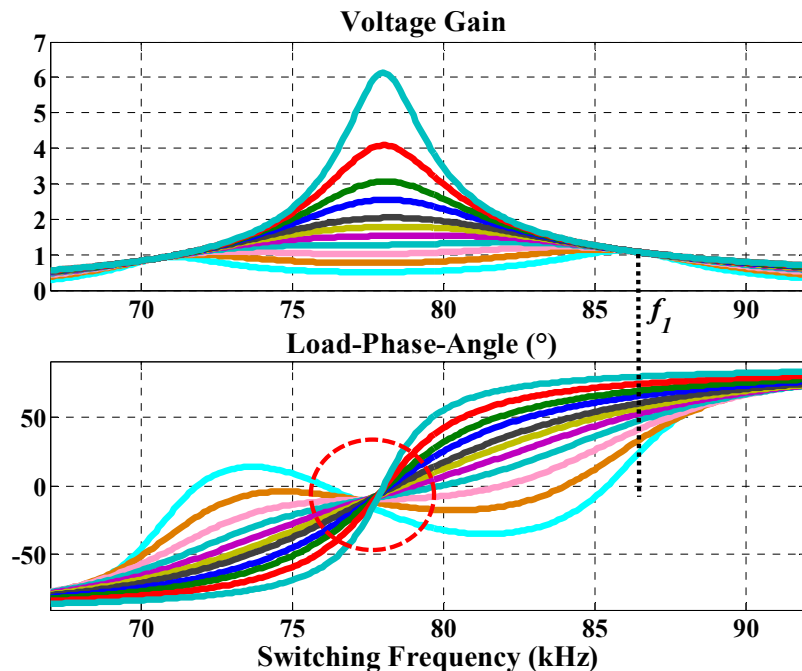
Fig. 3.6. Simulated DC characteristics: the voltage gain and load-phase angle versus the AC frequency in the SS-connected *LC*, where non-ideal C_2 increases from theoretical value in Fig. 3.2: 20.7 nF to 21.7 nF.

kHz and there is a small variance of the voltage gain the fixed-gain point. The load-phase angle at the ideal resonant frequency is not fixed at 0, as the part surrounded by the red circle. But there is still one zero-crossing point higher than f_0 for each load-phase-angle curve, meaning the control method works well. It is also possible that two zero-crossing points exist beyond the ideal f_0 on a single load-phase-angle curve. Then the system needs to measure the load-phase angle by a certain amount of times beyond the first tracked zero-crossing point, until the highest zero-crossing point is found. As the fixed-gain point locates right beyond the highest zero-crossing point of the load-phase angle, the fixed-gain point can be still determined by the proposed method.

3.3.5. Application of LLC Topology

Under the circumstances with strict limitations on the AC frequency (the SAE standard) or requiring a relatively fixed working frequency, an additional inductor is connected in series with the primary LC circuit to reduce the influence of varied magnetic coupling on f_1 [110]. As indicated by the Equations (3.4) and (3.6), the influence of M on f_1 is reduced if the value of L_1 increases. For example, if the added inductor is

$$L_1^{'} = \alpha L_1 ,$$

a larger α leads to a smaller range of f_1, considering all possible values of k. With a high enough α, the optimal frequency f_1 will be nearly constant in most of possible charging conditions. However, offsets exist when choosing α, including the decreased power-transfer capability and efficiency. With an additional inductor, the resonant frequency of the primary LC circuit is kept the same as the resonant frequency without L_1'. Thus, the primary resonant capacitance C_1 is adjusted accordingly based on the sum of the

inductance of the transmitting coil and the added inductance L_1'. The voltage gain of an S-connected load with an additional inductor is reduced to

$$G = \sqrt{L_2 / (L_1 + L_1')} \,. \tag{3.8}$$

Meanwhile, the power factor with light loads becomes lower. The voltage stress on the primary resonant capacitors is increased, meaning that the charger needs capacitors with higher voltage tolerance.

3.4. Design of the Universal Charging Interfaces

In an IPT system, a better charging pad generates better coupling, with the same air gap and horizontal misalignment. Better coupling leads to a higher power-transfer capability and better adaptability against air gap or misalignment. To the best of our knowledge, two types of pads are most commonly used in current research the inductive charging: the non-polarized pads, such as circular pads (CP) or square pads (SP), and polarized pads such as bipolar pads (BPP), Double-D or Double-D Quadrature pads (DDQP) [8, 65, 81, 111, 112].

Polarized pads are proven to have higher tolerance to horizontal misalignments because of the horizontally directed (parallel) flux on the surface of the pads. For example, a BPP is capable of operating with a polarized pad and providing perpendicular fluxes when another coil is non-polarized. For a more developed pad DDQP, a polarized DDP is combined with a Quadrature coil (Q coil). The Q coil can be used for coupling with the receiving pad when horizontal misalignment reaches a point with no net flux through DD coils [81]. To operate the charger with polarized pads, the system needs location sensors and employs complicated control methods on the currents in different

59

coils of the polarized pad. On the other hand, for a typical polarized pad, the higher tolerance of misalignment only exists in the lateral direction of the pads. This feature strongly limits the advantage of polarized pads. In the contrast, a non-polarized pad has the same tolerance on the misalignment in each direction. Non-polarized pads are much easier to operate. When a polarized pad and a non-polarized pad have an equal overall size, the size of one coil in a polarized pad (containing 2 coils) is smaller than the only coil of a non-polarized pad, leading to a lower magnetic coupling coefficient ($k = M / \sqrt{L_1 L_2}$) [81, 111, 113]. This is an important advantage of non-polarized pad, because the size of charging pads is usually limited in practical applications. More seriously, the flux in one coil of the receiving polarized pad is seriously influenced when the wrong coil (with inverse polar) of the transmitting pad moved to partly face this receiving coil, as shown in Fig. 3.7. Magnetic simulations are used to prove the advantages of non-polarized pads, as shown in Fig. 3.8. In Fig. 3.8, the DDPs and SPs have the same overall size (40cm×40cm), the same number of coil turns (20 turns by 2-parallel-connected wires), and the same air gap between the transmitting and receiving pads. In the simulations, the reasonable coupling coefficients k_{13} and k_{24} of the DDP-DDP pair (in Fig. 3.7) are lower than the coupling coefficient k between the SPs. Meanwhile, the undesired coupling coefficient k_{23} between the coil 2 and 3 is increased by the lateral misalignments, seriously influencing the equivalent coupling effect of the overall pad. The BPPs have similar trends of the magnetic coupling vs. lateral misalignment. Obviously, with limitations on pads' size, a SP performs much better. The popularity of the non-polarized pad in the current research is also an advantage for its practical application. As a result, the non-polarized pad is chosen as the charging interface for the proposed UIC.
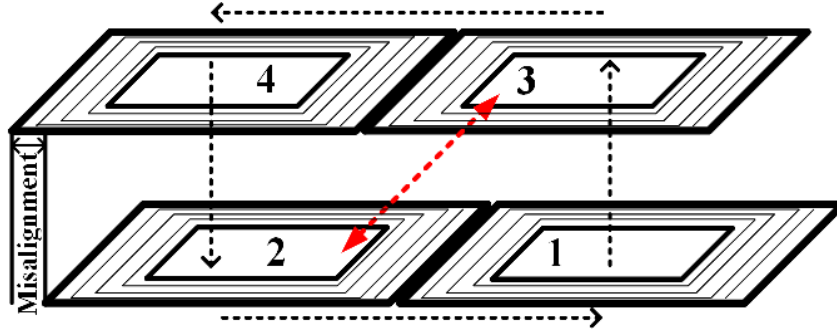
Fig. 3.7. Paths of magnetic flux generated by polarized pads: the black lines represent normal flux and the red line represents the undesirable coupling.

From another view, size limitation is also a basis for coil design. In practical applications, the size limitation on the charging pads is commonly on the diameter (CP), the edge-length (SP), or width & length (rectangular pad) of the coil. This means that the
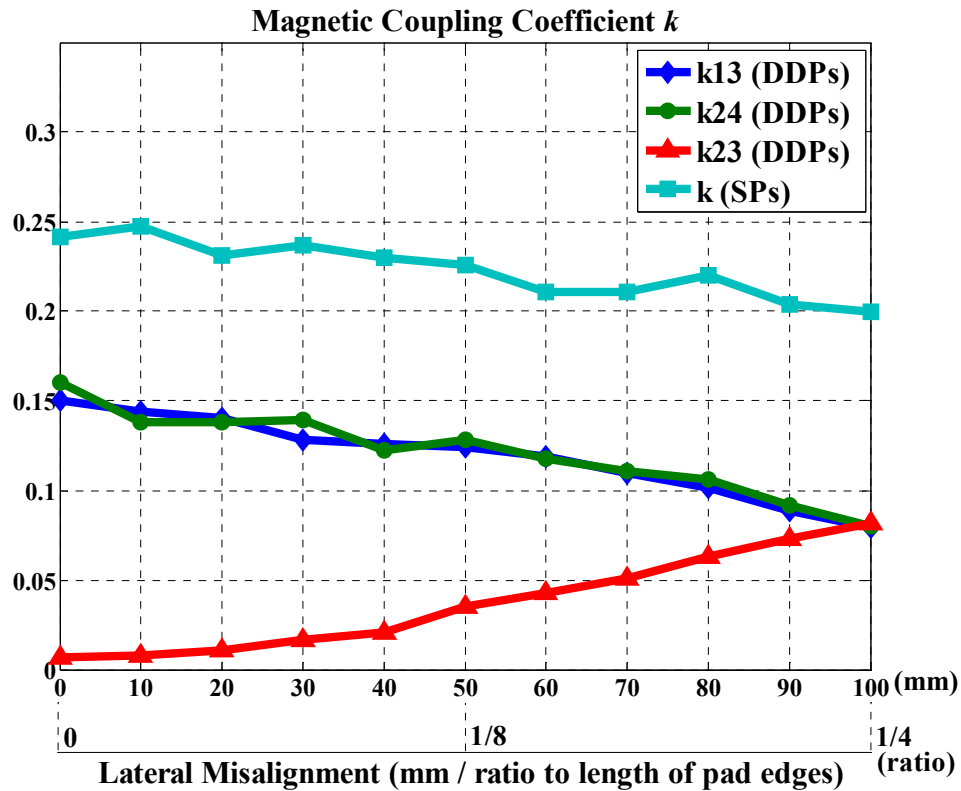
Fig. 3.8. Simulated coupling coefficients between coils 1&3 (k_{13}), 2&4 (k_{24}) and 2&3 (k_{23}) of the DDPs in Fig. 7, comparing to the coupling coefficient (k) between the coils of SPs, with the same air gap 12cm, and various lateral misalignments 0 ~ 100 mm.

maximum coupling coefficient can be achieved by SPs with the longest edges, because the area of a SP is higher than a CP when the edge of the SP is equal to the diameter of the CP [81]. The specific shape of charging pads depends on the parameter M^2/L_2, which determines the power-transfer capability [5]. Magnetic simulations are built with SPs and CPs with the same length of the outer and inner edge or diameter: the SP with the inner edge of 28 cm, the outer edge of 40 cm, and 20 turns 2-parallel-connected wires; the CP with the inner diameter of 28 cm, the outer diameter of 40 cm, and 20 turns 2-parallel-connected wires. By comparing M^2/L_2 of various pads' combinations, including CP&CP, CP&SP, SP&SP, with various air gaps (1/4 ~ 1/2 of the outer edge or diameter of the pad) and horizontal misalignments (0 ~ 3/8 of the outer edge or diameter of the pad), the pair of SPs has the highest M^2/L_2, as shown in Fig. 3.9. The coupling coefficients of the three combinations vary in the similar trend. Thus, SPs are the optimal design of the universal charging pad in the proposed system.

The specific parameters of the charging interfaces are determined by the planned voltage and current of the IPT system, such as the number of the coil turns, the dimensions, and the application of ferrite bars. The first matter coming to mind is the voltage gain determined by the self-inductances of the coils, according to Equations (3.3) and (3.5). Moreover, with the same current level, a coil with larger self-inductance generates a higher voltage stress on the resonant capacitors. The voltage stress must be limited because of the voltage tolerance of the resonant capacitors. In some applications, the coil-wires are parallel connected and placed by two layers, to reduce the self-inductance.
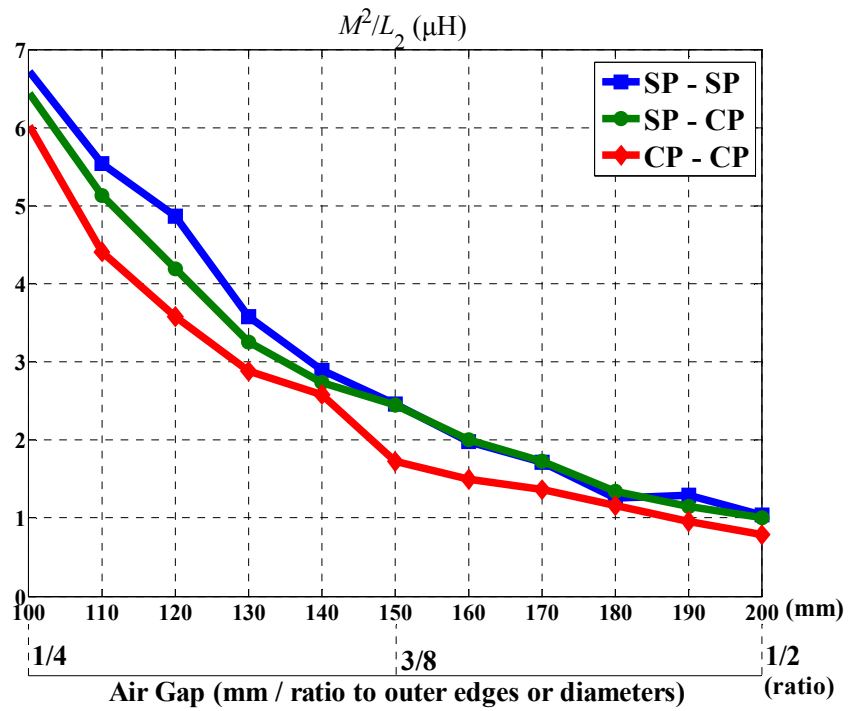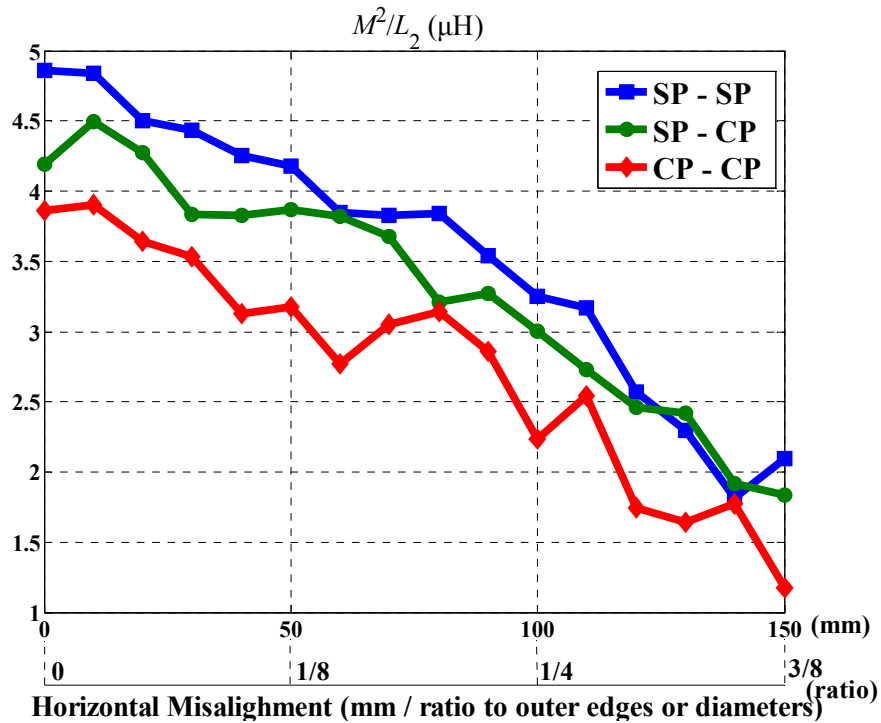
Fig. 3.9. Simulated parameter M^2/L_2 versus (a) air gaps (100 ~ 200 mm, 0 horizontal misalignment), and (b) horizontal misalignments (0 ~ 150 mm, 120 mm air gap), with three different pad combinations.

63

3.5. Experimental Validation

A 5 kW (maximum power) prototype is built to test the applicability of the proposed system. Two types of receiving coils, an SP (Coil 1) and a CP (Coil 2) are used for testing. The parameters of each coil and resonant capacitance are listed in Table 3.2. Note that the SPs in experiments are the same as those used in magnetic simulations. A full-bridge inverter is used to generate AC power for wireless charging. A control system built by DSP and FPGA focuses on switch-signal calculations, measurements of voltages and currents, and generating gate-drive signals. A frequency-tracking module made by analog devices and logic circuits is used to detect f_1, based on the structure in Fig. 3.5.

Table 3.2. Parameters of Transmitting and Receiving Coils

Parameters	Transmitting coil	Receiving Coil 1	Receiving Coil 2
Dimensions	Inner length 28 cm, Outer length 40 cm.	Inner length 28 cm, Outer length 40 cm.	Inner diameter 20 cm, Outer diameter 28 cm.
Self-Inductance	199.5 µH	200.8 µH	89.8 µH
Resonant Capacitance	20.9 nF	20.7 nF	46.6 nF
Turn NO.	20	20	15
Threads/Turn	2	2	1
Others		4 Ferrite Bars on Back	4 Ferrite Bars on Back

3.5.1. Experimental Results by Receiving Coil 1

When the receiving coil is the coil 1, the efficiency and the voltage gain G vs. R_{load} are measured, with various air gaps, as shown in Fig. 3.10.
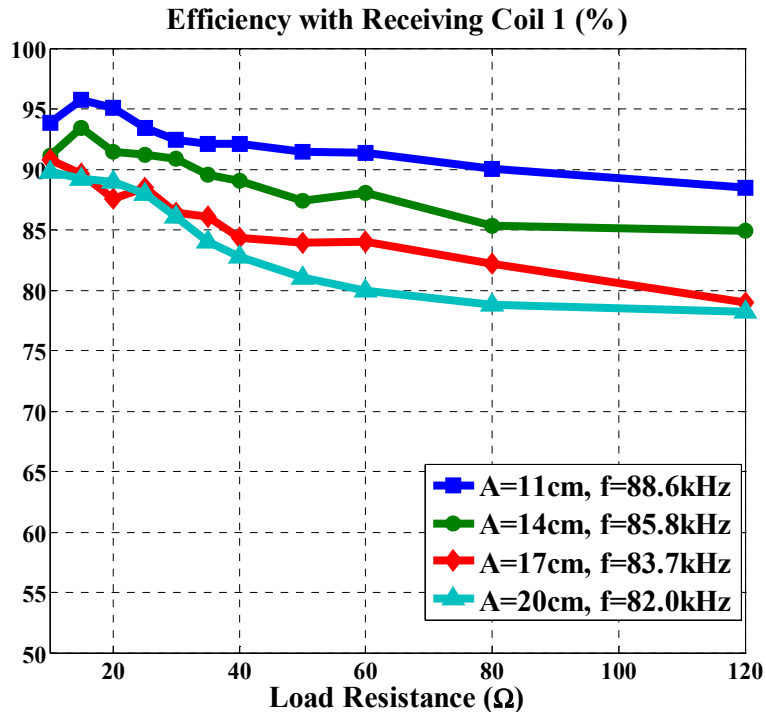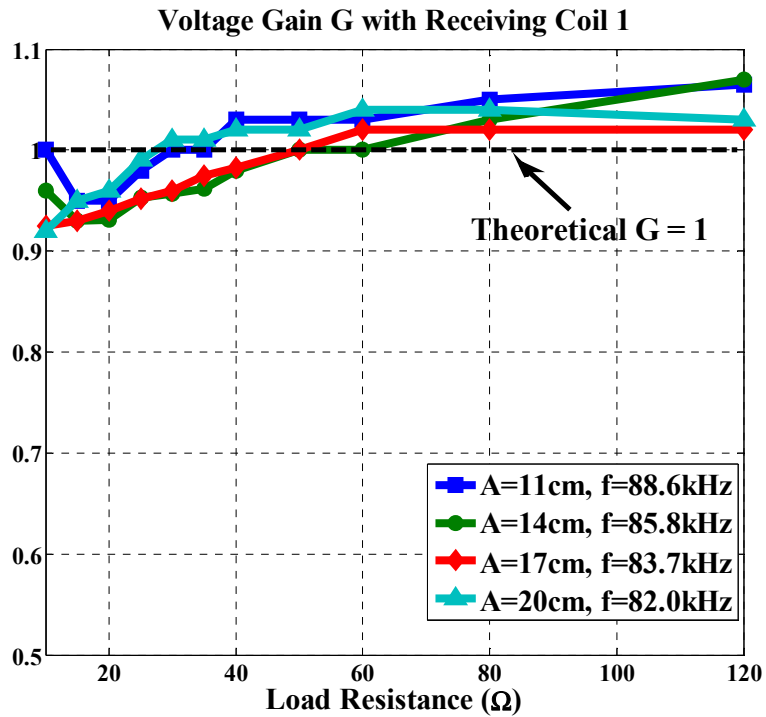
Fig. 3.10. (a) System efficiency and (b) the voltage gain vs. R_{load} (=10, 15, 20, 25, 30, 35, 40, 50, 60, 80, 120 Ω), with different air gaps A, when the load contains the coil 1.

The frequency tracking with different air gaps is achieved by the control system. The ZVS is maintained by the system in all four coupling conditions. The control system tracks the optimal frequency with the lowest R_{load} (full load) and keeps the frequency constant during the charging process. According to the curves of the efficiency and the voltage gain, the following results are acquired:

1) The tracked optimal frequency f_1 becomes lower when the mutual coupling is reduced.

2) The efficiency of the system decreases when the air gap increases.

3) With a fixed frequency during the charging process, the efficiency of the system generally reduces as R_{load} increases (the load becomes light).

4) The voltage gain is maintained around the theoretical value $G = 1$ (error < 8%), but the specific trend of each curve depends on the value of the air gap.

By analysis, the larger the mutual inductance is, the more influence the secondary side has on the primary side, since a larger impedance is reflected to the primary side. As a result, the fixed-gain point will be shifted to be a larger value from the resonant frequency when the mutual coupling increases. This phenomenon is also demonstrated by simulations in Fig. 3.2. As shown in Fig. 3.2, the phase angle increases (> 0) and the power factor reduces, when the frequency is maintained constant at the fixed-gain point and R_{load} increases. The efficiency reduces when the power factor of the entire system is reduced, because more power is consumed by the parasitic resistances of the coils. However, when the air gap A is 11 cm or 14 cm, the efficiency firstly increases and then reduces. The main reason for this trend is the higher current level with heavier loads. With a heavy load, the power loss by undesirable coupling with surrounding objects is

more apparent and occupies the main part of the loss. In the circuit model, there is an equivalent resistance r' connected with M, simulating the power consumption caused by flux leakage or undesired coupling. When the magnetic coupling reduces, the power consumed by r' becomes relatively stable (although varies) during charging. The power loss caused by resonant components becomes the main reason of the efficiency variance. In other words, when the coupling between the coils is tighter, the influence of the current level (influenced by load variance) is more serious, since more percentage of the power is consumed by parasitic resistances vs. overall power. The variance of the voltage gain with different air gaps has a similar trend. With tighter coupling (air gap is 11 cm or 14 cm), G firstly decreases and then increases, as R_{load} increases. For the voltage-gain curves of $A = 17$ cm and $A = 20$ cm, G increases as the load becomes light. Although the voltage gain is not strictly maintained to be the ideal value, the practical range of G from 0.92 to 1.07 is still much smaller than the range from 0.3 to 6 when the AC frequency is the resonant frequency (shown in Fig. 3.2). In fact, another reason for the inaccurate output is that the frequency tracked the system is not exactly the theoretical f_1. The theoretical f_1 is tracked by the zero-phase angles with an extremely small R_{load}. The practical f_1 is acquired at the heaviest load, meaning that the frequency is a still lower than f_1, although ZVS is achieved. Thus, there is a small error between the practically tracked frequency and the theoretical fixed-gain frequency.

3.5.2. Experimental Results by Receiving Coil 2

With the receiving coil 2, the system efficiency and the voltage gain vs. R_{load} are shown in Fig. 3.11.
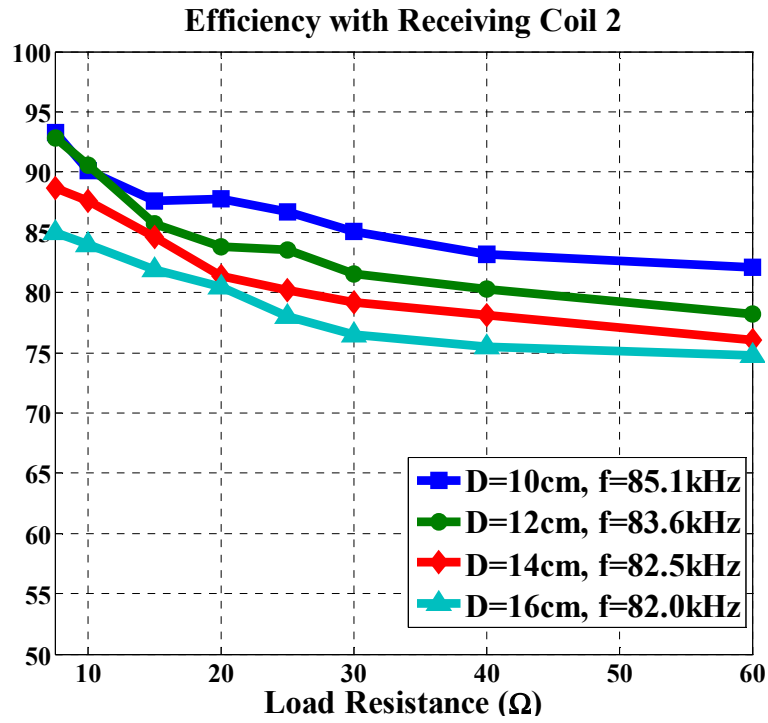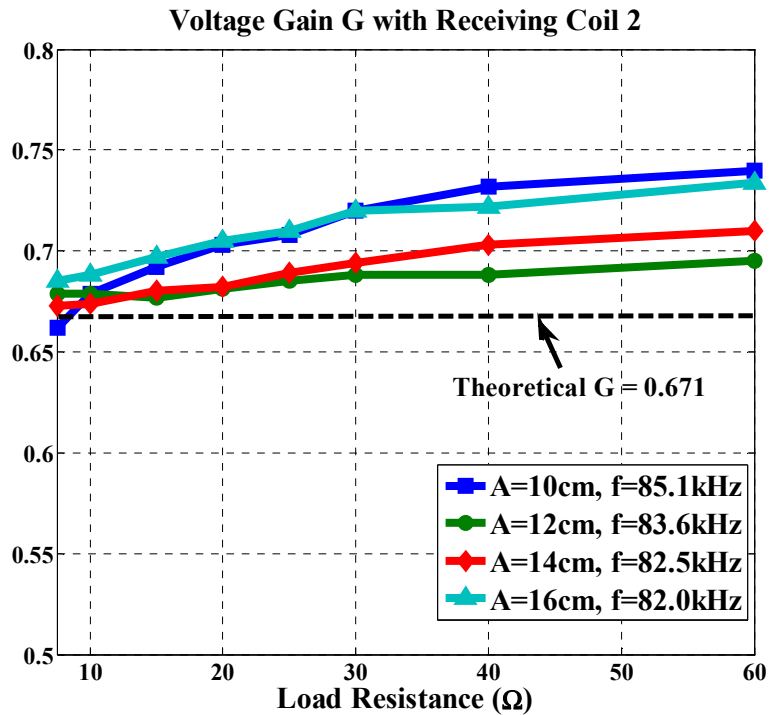
Fig. 3.11. (a) The system efficiency and (b) the voltage gain vs. R_{load} (=7.5, 10, 15, 20, 25, 30, 40, 60 Ω), with different air gaps A, when the load contains the coil 2.

Still, a larger air gap leads to a lower optimal frequency. With a fixed air gap, the efficiency keeps reducing as the load becomes light. Here, the variances of the system efficiency and the voltage gain vs. A or R_{load} are similar to the curves of A = 17 cm and A = 20 cm in Fig. 3.10 (with the coil 1), because of relatively loose coupling.

Obviously, the system efficiency with the coil 2 is lower than the efficiency with the coil 1. The main reason for the lower efficiency is the looser coupling between the transmitting and receiving coils. As the receiving coil 2 is much smaller than the transmitting coil, more flux leakage is generated. This is also the reason why a square coil is preferred: a larger charging area with a better coupling effect [111]. By magnetic simulations, a reasonable combination of the charging interfaces requires two coils to have similar sizes.

3.5.3. Variable-Frequency Control

The variable-frequency control is applied in the hardware experiments, with the receiving coil 1. Based on Equation (3.7), the phase-angle threshold for frequency variance is set to be 40 degrees and the coefficient of frequency variance η is 1/5. Then, the experiment results are:

1) A = 11cm, the frequency is adjusted from 88.6 kHz to be 87.2 kHz, when R_{load} = 30 Ω.

2) A = 14cm, the frequency is adjusted from 85.5 kHz to be 84.6 kHz, when R_{load} = 25 Ω.

3) A = 17cm, the frequency is adjusted from 83.7 kHz to be 83.3 kHz, when R_{load} = 20 Ω.

4) A = 20cm, the frequency is maintained as 82.0 kHz, because the lowest bound for the standard AC frequency is 81.38 kHz.

Note that the variances of frequency are increased by multiple small steps, as 0.1 ~ 0.16 kHz for each step in these experiments. In hardware experiments, the interval between each two steps of frequency variances is 10 seconds.

3.5.4. Accuracy of Tracked f_1

As previously mentioned, there is a small error between the theoretical f_1 and the practical f_1 tracked by the proposed control method, leading to a non-constant charging voltage V_{out} during the charging process, as shown in Fig. 3.10(b) and Fig. 3.11(b). Based on the various coupling effects in Fig. 3.10 and Fig. 3.11, comparisons are made between the practical f_1 acquired in experiments and the theoretical values, as shown Fig. 3.12. The theoretical values of f_1 are accurately measured by the oscilloscope and the relevant voltage-gain analysis.
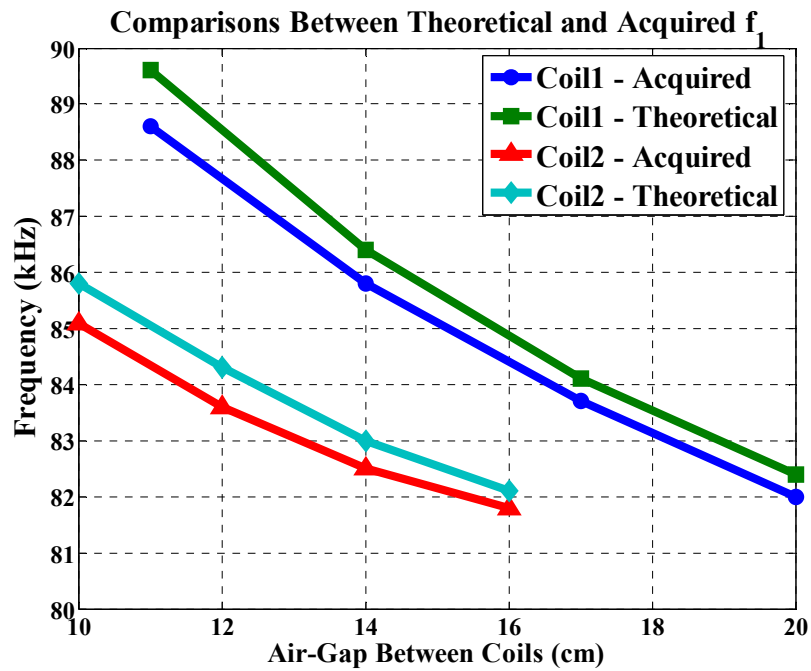
Fig. 3.12. Theoretical f_1 and practically tracked f_1 by the proposed control method, with two different coils and various air gaps.

In Fig. 3.12, the theoretical values of f_1 are consistently higher than the acquired values by experiments. The error ranges from 0.3 to 0.8 kHz and increases when the coupling effect increases (a smaller air gap). The main reason for the error is from the equivalent resistance R_{load}. In fact, the practical f_1 is tracked when the load is the heaviest R_{load}, but the theoretical value of f_1 must be tracked with the extremely small R_{load}. The accuracy is acceptable, because the variance of the voltage gain caused by the frequency errors is limited in a small range. More accurate frequency tracking can be achieved by the specific control of the on-board chargers during frequency tracking.

3.5.5. ZVS of the Primary DC-AC Inverter

Based on the proposed frequency control, ZVS (turn-on) has been universally achieved in all charging conditions with the coil 1 and 2. For example, a set of waveforms for typical ZVS operation is shown in Fig. 3.13. In Fig. 3.13, the overall equivalent load for the primary DC-AC inverter is inductive, as the input current of the primary LC circuits lags the input voltage. During Δt, the current flows through the body diode of the measured MOSFET that has not been turned on yet. The Drain-to-Source voltage V_{DS} of the MOSFET is maintained nearly zero at the moment. After Δt, the gate-driving signal turns on the MOSFET with zero V_{DS} and ZVS is achieved. As a result, an inductive equivalent load leads to ZVS turn-on of the DC-AC inverter in the primary side. According to the load-phase-angle curves in Fig. 3.2, the phase difference between the input voltage and current is increased when the load becomes light. This means that the equivalent impedance will be inductive during the whole charging process if the equivalent impedance with the heaviest load is inductive (ZVS). Because the optimal

71
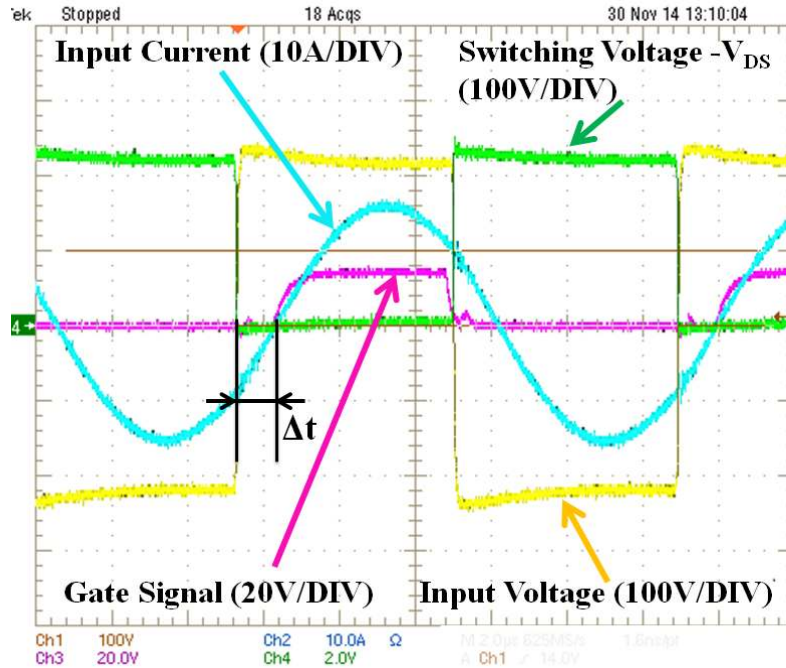
Fig. 3.13. The input voltage and current of the primary *LC* circuit and the gate-driving signal and drain-to-source voltage V_{DS} of the MOSFET Q_1 in Fig. 3.3, when the load contains the coil 1, A = 14 cm, R_{load} = 30 Ω, the input DC voltage = 200 V, and the frequency = 85.8 kHz.

frequency is tracked at the beginning of each charging cycle with a different coupling effect, ZVS can be universally achieved.

3.6.　Chapter Summary

In this Chapter, a UIC is proposed to provide the stable and controllable charging voltage to loads with different designs via a wide range of magnetic coupling effects between the transmitting and receiving coils. Based on circuit and magnetic analysis, a specific standard of designing the UIC for EVs is also provided. The S-connected *LC* circuit proves to be the optimal topology for primary resonant circuit. A control method is applied to track the optimal frequency, based on the load-phase angle. A non-polarized coil in square shape is preferred as the charging interface. Hardware experiments have

72

demonstrated the high efficiency and universality of the proposed system, with the following advantages.

1) Universal Application: faced with the market with more and more EV models, the proposed system provides stable and controllable charging voltage (the error of voltage gain < 10% with a typical range of the coupling coefficients varying from 0.1 to 0.25) to various EVs with different receiving coils, connections of LC circuits, and load ranges.

2) Adaptive Frequency Control: with a wide range of the varied mutual inductances, the proposed system provides a stable charging voltage by adjusting the AC frequency to be an optimal value automatically. Moreover, the AC frequency can be further adjusted during the charging process to increase the power factor and efficiency.

3) Effective V&I Sensing: The proposed control system has no requirement on the speed of sensing and A/D conversion. The control method is also capable of detecting the LC connection.

4) High Efficiency (the highest efficiency 96%): in the proposed system, the ZVS is maintained during the charging process, leading to lower power loss. With the same air gap and misalignment between coils, the square coil generates tighter coupling and less leakage flux, meaning less power losses.

However, the current design still has some defects. For example, if the load condition is light ($R_{load} > 40\ \Omega$) at the beginning of the charging process, the tracked AC frequency may have a significant error from the optimal frequency: the fixed-gain point. The shift from the optimal frequency will generate a larger range of the output voltage

around the ideal voltage gain. The error becomes more serious when the practical values of inductances and capacitances are different from the theoretical values. From the view of the entire system, the system is more comprehensive when there is a design scheme of the on-board charger. For example, if the transmitting pad of the UIC is fixed, the receiving pad shouldn't be too larger or smaller than the transmitting coil. In common sense, the coupling effect is optimal when the sizes of the two pads are similar to each other. As the output voltage of the secondary LC circuit is related to the self-inductances of the two coils, the receiving pad should also be designed based on the transmitting pad. As a result, a design scheme of the on-board charger is necessary, including a receiving pad and a specially designed AC-DC converter. A design scheme of the on-board charger used for universal inductive charging will be proposed in the next Chapter.

CHAPTER 4: DESIGN OF ON-BOARD CHARGERS WITH S-CONNECTED LC CIRCUITS

4.1. Overview

A UIC is proposed in Chapter Three, which provides stable and high-efficiency charging to different EV models even with the influence of various receiving coils and varied magnetic coupling effects. From the view of the entire system, an on-board charger working in coordinating with the proposed UIC is another essential piece of the picture of universal inductive charging.

In this Chapter, a scheme of designing the on-board charger used for universal inductive charging of EVs is proposed. The main structure of the proposed on-board charger is shown in Fig. 4.1. The design and control of the on-board charger is based on the concept of universal inductive charging: adaptive, efficient and safe EV charging, in various coupling and load conditions. The S-connected LC circuit is preferred as the resonant circuit of the receiver, for a stable output voltage at the fixed-gain point vs. mutual inductance. A detailed design process of the receiving pad is also provided, according to a higher coupling coefficient and power-transfer capability. An easy control
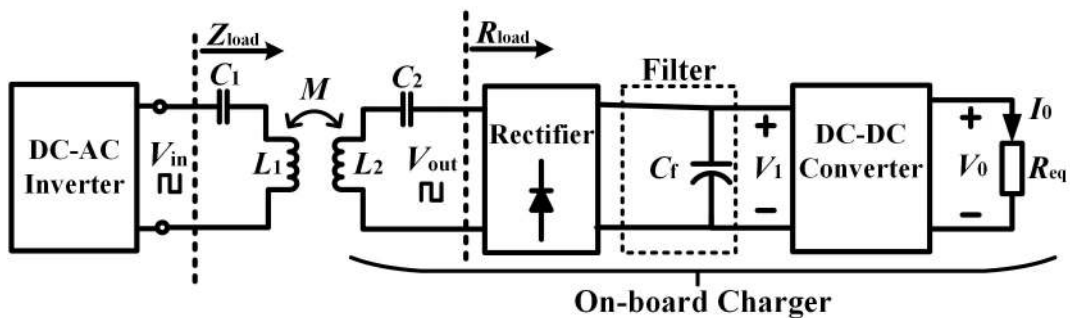
Fig. 4.1. The basic structure of the on-board charger applied in an IPT system, with SS-connected LC circuits.

method based on the dual-mode modulation of the DC-DC converter is applied to coordinate with the UIC for more accurate frequency tracking.

4.2. Existing Problems of the UIC

Although the proposed UIC proves to be robust and efficient, some problems influence the accuracy of tracking the optimal frequency f_1. The proposed on-board charger should help improve the accuracy of frequency tracking. Moreover, the output of the secondary LC circuit should not be connected to the EV batteries directly, because any influence from the surrounding environment could suddenly change the electrical characteristics and damage batteries [1, 114]. Thus, a charging system needs an on-board charger to regulate the charging voltage and current.

In Fig. 4.1, R_{load} is the equivalent resistance reflected to the secondary LC circuit. R_{eq} is the equivalent resistance representing the power consumptions of EV batteries combined with the BMS. As indicated in Fig. 3.2, when the reflected resistance R_{load} is smaller, the zero-crossing point of the load-phase angle is closer to the fixed-gain point f_1. This means that the f_1 is more accurately tracked when the load is heavier. The theoretical value of f_1 is acquired at the zero-crossing point of the load-phase angle when R_{load} is infinitely small. To coordinate with the UIC, the on-board charger should be specifically designed to make sure R_{load} is small enough, even if the charging cycle begins with a medium or light load. In other words, the reflected R_{load} should be small enough (by the on-board DC-DC converter), although the equivalent resistance R_{eq} is large.

Another problem exists in the load containing a P-connected secondary LC circuit. With a P-connected LC circuit, the voltage gain is related to the value of the mutual

inductance between the coils. Therefore, the voltage gains in different charging cycles are different from each other because of the varied mutual inductances. A stable voltage gain needs more complicated modulation of the on-board DC-DC converter. The problems of P-connected secondary *LC* circuit will be solved in Chapter 5.

In this Chapter, the design of the on-board charger can be divided into three aspects: the design of the secondary *LC* circuit, the design of the receiving pad and the design and operation of the on-board DC-DC converter. Usually, the secondary *LC* circuit is not adjustable in a high-power application. Thus, the DC-DC converter is the only adjustable part. Thus, operation of the on-board AC-DC converter is done by modulating the DC-DC converter.

4.3. Design of the Secondary LC Circuit

For common analysis of an S-connected and a P-connected secondary LC circuits, an S-connected *LC* circuit is easier to tune and performs better in reducing harmonics, while a P-connected *LC* circuit acts as a current source and has a low voltage stress on the resonant capacitance. Previously published papers select series- or parallel-connected *LC* circuit according to more specific issues [24]. However, some problems exist in systems with a P-connected primary *LC* circuit, such as high turn-off current and non-zero load reactance. The problems reduce the efficiency and influence the tuning of the *LC* circuits [5, 26].

More importantly, the S-connected secondary *LC* circuit is more suitable for universal inductive charging, according to the DC characteristics of the SS- and SP-connected *LC* circuits in Fig. 3.2. First, by Equation (1), the voltage gain at the fixed-gain

point is not related to the mutual coupling, when the *LC* topology is SS-connected. However, if the load (EV) has a P-connected *LC* circuit, the voltage gain at the fixed-gain point is varied by mutual inductance, although the voltage gain is fixed in a certain charging cycle. The range of the possible voltage gain is large (for example, *G* ranges from 4 to 10) because of the large range of possible mutual inductances. Thus, a P-connected LC circuit needs more complex modulation on the on-board DC-DC converter. Universality of the inductive charging system is then weakened. Secondly, if the load has a P-connected *LC* circuit, the AC frequency generated by the UIC should be slightly higher than f_1 to achieve ZVS of the primary DC-AC inverter. However, as indicated in Fig. 3.2(b), the voltage gain with a heavy load descends sharply when the frequency is increased to be higher than f_1. Thus, a small error between the practical AC frequency and theoretical f_1 leads to significant variance of the output voltage. The frequency that simultaneously realizes both ZVS and a relatively constant voltage gain is difficult to detect. By the two reasons, an S-connected *LC* circuit performs better as the secondary resonant circuit, because of a more stable V_{out} and the minimum requirement on system control. In fact, the constant-current model of a P-connected *LC* is unnecessary, if the on-board back-end converter is capable of further controlling charging voltage and current. Some previously proposed designs apply P-connected secondary *LC* with an AC-DC converter with controllable DC current output. Because of the characteristics of P-connected *LC*, the proposed operation of usually lacks of universality for either varied coupling or varied load condition. For example, the on-board charger in [20] applies P-connected *LC* circuit and a Class-D rectifier: the primary DC-AC inverter cannot operate

78

at optimum condition when load is decreased and the air gap is limited in a small range. The soft-switching operation of converters cannot be adaptively achieved.

Previous research proposes some designs applying more complex resonant circuits, such as the *LCL* compensation network, which is proposed in [115]. The *LCL* circuit is developed from a P-connected *LC* circuit and minimizes the reactive current and reflected VAR. However, when the mutual inductance varies in a wide range, the proposed system with an *LCL* cannot be adjusted accordingly. Moreover, more resonant components used in the resonant circuit usually lead to lower efficiency because more power is consumed by the parasitic resistance in *L*'s and *C*'s.

For design of *LC* circuits, another important parameter is the resonant frequency. In Fig. 3.2, the DC characteristics are simulated by an IPT system with the equal resonant frequency of the primary and secondary *LC* circuits. If the resonant frequencies of the primary and secondary *LC* circuits are different, the curves of the DC characteristics are moved, especially the position of f_1 and the relevant voltage gain. The fixed-gain point will disappear when the difference is large enough [4]. Therefore, the resonant frequencies of both sides should be equal or close to (small error exists in practical conditions) each other. The requirement on the identical resonant frequencies of both sides is reasonable by common sense. Moreover, there is a standard (SAE J2954) limiting the AC frequency used in wireless charging of EVs (81.38 kHz ~ 90 kHz). The standard requires the proximity in the frequency setting of the *LC* circuit on EV to the *LC* circuit of the primary charger, because the applied AC frequency is determined by *LC* circuits and it must be in the standard range. It is very easy to equalize the resonant frequencies of

the two sides: with a determined self-inductance of the receiving coil, EV manufacturers set C_2 based on the resonant frequency.

In summary, the S-connected *LC* circuit is a better choice for the secondary LC circuit, and the resonant frequencies of both *LC* circuits must be equal to each other.

4.4. Design of the Receiving Pad

In the proposed UIC, a square non-polarized transmitting pad proves to be better in magnetic coupling, when the pad size is limited. Similar to the design of the transmitting pad, if the length and width of the receiving pad is limited, a non-polarized receiving pad has the best coupling, because the single coil is the largest while a larger receiving coil commonly leads to better magnetic coupling.

However, coupling effect is not linearly related to the coil size. The coupling effect cannot be improved obviously by increasing the coil size, when the receiving coil is too large. To show this phenomenon, magnetic simulations are made by MAXWELL, with a fixed transmitting pad and different receiving pads. Fig. 4.2 shows the two receiving pads coupled with the same transmitting pad. The square transmitting pad is
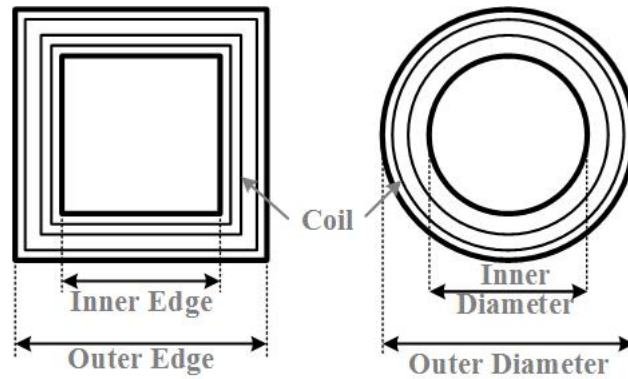
Fig. 4.2. In magnetic simulations, the configurations of the two receiving pads that are coupled with the same transmitting pad as [4].

with the inner/outer edge 280mm/400mm and 20 coil turns (same as [4]). The inner edge or diameter of the receiving pads is increased from 220mm to 340mm, with fixed 20 coil turns. Two values are commonly used for evaluating the coupling effect of the two coils: the mutual coupling coefficient k and M^2/L_2. The value of k is directly related to the coupling effect, while M^2/L_2 determines the power-transfer capability of the IPT system [5]. As shown in Fig. 4.3(b) and Fig. 4.3(c), the simulated values of k and M^2/L_2 increase with the inner edge (of a square pad, SP) or inner diameter (of a circular pad, CP) of the receiving coil. The variation trends of k and M^2/L_2 are also related to the air gap between the coils. In practical applications, the air gap is usually limited in a range from 1/4 to 1/2 of the outer length or diameter of the coils. In this range, the two parameters k and M^2/L_2 are maintained relatively stable when the size of the receiving coil is increased to be larger than the transmitting coil. So, the effect of increasing the coil size on improving coupling effect is limited. This result is also demonstrated by theoretical analysis in [18, 81]. By theoretical analysis, a larger inner part (area surrounding by coil) of a receiving pad collects more flux, when the transmitting pad is fixed. As a conclusion, the larger the receiving pad is, the better the coupling effect will be. A good option for saving space is to design the receiving pad as the one with the same or similar shape and size as the transmitting pad.

Design of the receiving pad is also related to the voltage and current level of the on-board AC-DC converter. According to (1), the square root of the ratio of L_1 to L_2 is equal to the ratio of the nominal voltage input of the on-board AC-DC converter (or output voltage of the secondary LC circuit, V_{out}) to the nominal voltage input (V_{in}) of primary LC circuit.
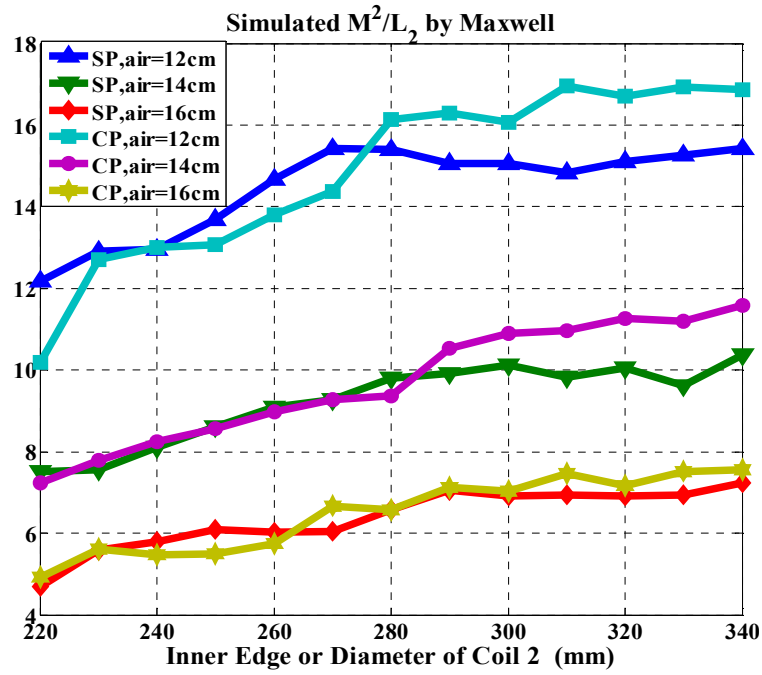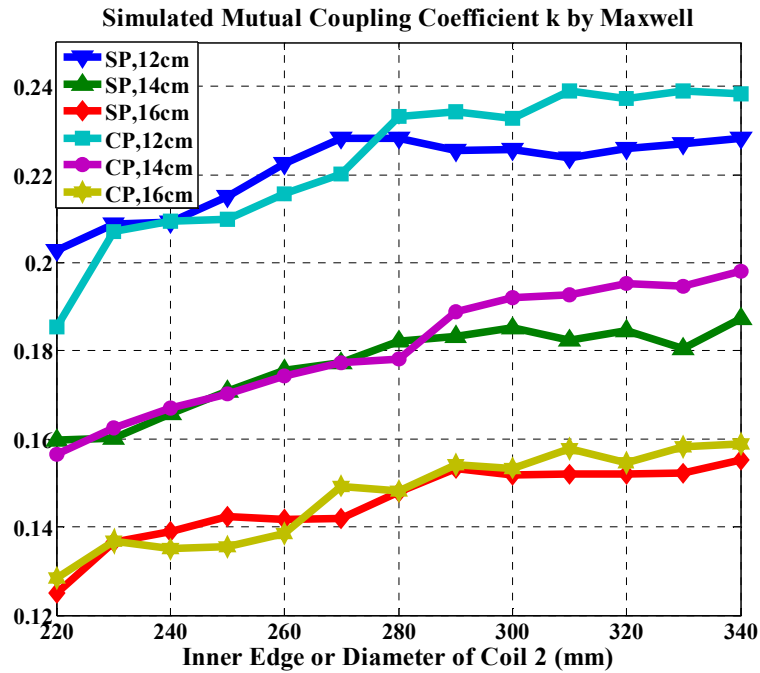
Fig. 4.3. The simulated (a) M^2/L_2 and (b) k of two pads with different air gaps, when the transmitting coil is in a square shape with the inner edge 280 mm and the outer edge 400 mm, and the receiving pad (Coil 2) is a SP or a CP, with different values of inner edge or diameter but fixed coil turn number and wire connection.

In summary, to design a receiving pad, the size limitation and the nominal voltage gain are the most important parameters. First, under the size limitation, designers should set the receiving pad as large as possible. The inner edge or diameter can be designed as a certain ratio of the largest inner edge or diameter (spare space left for coils). Then, by magnetic simulations or theoretical calculations [18, 81, 116], designers can estimate the number of coil turn that leads to a L_2 satisfying the requirement of the nominal voltage gain. Finally, if the final coil size is still smaller than the limitation or designers want to improve coupling effect by adding ferrite bars, coils' inner edge or diameter and coil turn can be further adjusted by simulations or theoretical calculations. The specific shape of the receiving pad is chosen by practical requirements.

4.5. Design of DC-DC converter

4.5.1. Voltage Step-up DC-DC Converter

According to the existing problems of the UIC, f_1 is accurately tracked when the reflected resistance is R_{load} small. In Fig. 4.1, a smaller reflected resistance R_{load} by the on-board DC-DC converter leads to a more accurate f_1. In practical operations, R_{load} is reduced by the modulating the duty cycle of the switch signal used in the DC-DC converter, during the frequency-tracking process. Therefore, a voltage step-up DC-DC converter contributes to a more accurately frequency control, because a step-up converter reflects a smaller R_{load} from equivalent resistance of batteries R_{eq} to the secondary LC circuit. For example, a boost converter is applied to regulate the charging voltage and current. If the duty cycle of the switch signal is D, and the boost converter works in the continuous-conduction mode (CCM), the relationship between R_{load} and R_{eq} is

$$R_{load} = (\frac{8}{\pi^2}) \bullet (1-D)^2 R_{eq}. \tag{4.1}$$

Note that the value of $8/\pi^2$ is used for transfer the resistance at the DC output ports to the AC output of the secondary LC circuit when the boost converter has a PFC function for improving the AC current of the secondary LC circuit. Besides accurate frequency control, a step-up converter is more suitable for the on-board DC-DC converter, because of the nominal voltage gain of an SS-connected topology and the nominal charging voltage of EV batteries. First, the commonly-used outlet voltage of the charger is usually lower than the nominal charging voltage ($> 300V$) of EV batteries. For instance, charging voltage of Nissan Leaf batteries is between 300 V and 420V during the charging process, but the electrical sockets (outlets) in the USA usually supply electricity at between 110 and 120 volts AC. Meanwhile, the primary inductance L_1 is usually larger than the secondary inductance L_2 because of the limitation of the size of the receiving coil. Therefore, the output voltage of the secondary LC circuit V_{out} is usually lower than V_{in}, according to Equation (1). Therefore, a step-up voltage converter is necessary to provide the nominal charging voltage to EV batteries.

4.5.2. Operation of DC-DC Converter

To achieve universal charging, a dual-mode scheme of modulation on the on-board charger is proposed to interact with the UIC. The main difference between the two modes is from the modulation of the back-end DC-DC converter in Fig. 4.1, because the DC-DC converter is the only controllable part of the on-board charger. The 1st-mode modulation is applied to more accurately track f_1 before charging cycle begins. The 2nd

mode provides nominal charging V_o & I_o to EV batteries, as the traditional operation of a DC-DC converter. The detailed operation process is shown in Fig. 4.4.

In the Mode 1, the modulation of the DC-DC converter is different from the traditional PWM. According to the existing problems of the UIC, f_1 can be accurately tracked when R_{load} is small. The DC-DC converter must be modulated to reflect a smaller R_{load}, with a specific duty-cycle D_1. According to (3), R_{load} is reduced by increasing D_1. On the other hand, V_o is increased. However, the EV batteries have specific charging profiles and the maximum charging V_o&I_o allowed. The modulation of the DC-DC converter need to avoid the higher V_o or current I_o beyond the limits, although the initial input voltage V_{start} of the charger is of a much lower value than the nominal value. For example, if the DC-DC converter is a typical boost converter, the reflected resistance R_{load} is reduced by increasing the duty cycle D. However, the charging voltage V_o will be increased to be higher than the limit if D is too large. As a result, D_1 depends on the load condition at the beginning of the charging cycle. The on-board charger can keep measuring the transient voltage and current and further adjust the duty cycle for safe charging. Detection of batteries' state at the beginning of Mode 1 operation is also necessary, since the V&I limits are related to the residual capacity of batteries.

When f_1 is tracked by UIC, the input voltage of the DC-DC converter V_1 is increased to the nominal value, as

$$V_1 = V_{in} \cdot G. \tag{4.2}$$

Then, the DC-DC converter starts the Mode 2: the typical charging process. The start of the Mode 2 is detected by the on-board charger if the input voltage of the DC-DC

converter V_1 is higher than a threshold value V_c, because the input voltage of the on-board charger has been increased step by step towards its nominal value, according to the increased input voltage of the primary LC circuit after tracking the frequency. The charging process of the EV batteries is commonly divided into two stages: constant current charge and saturation charge. The charging cycle may be started at either the first or second stage. This requires a comprehensive detection of the batteries' status when modulating the DC-DC converter in Mode 2.
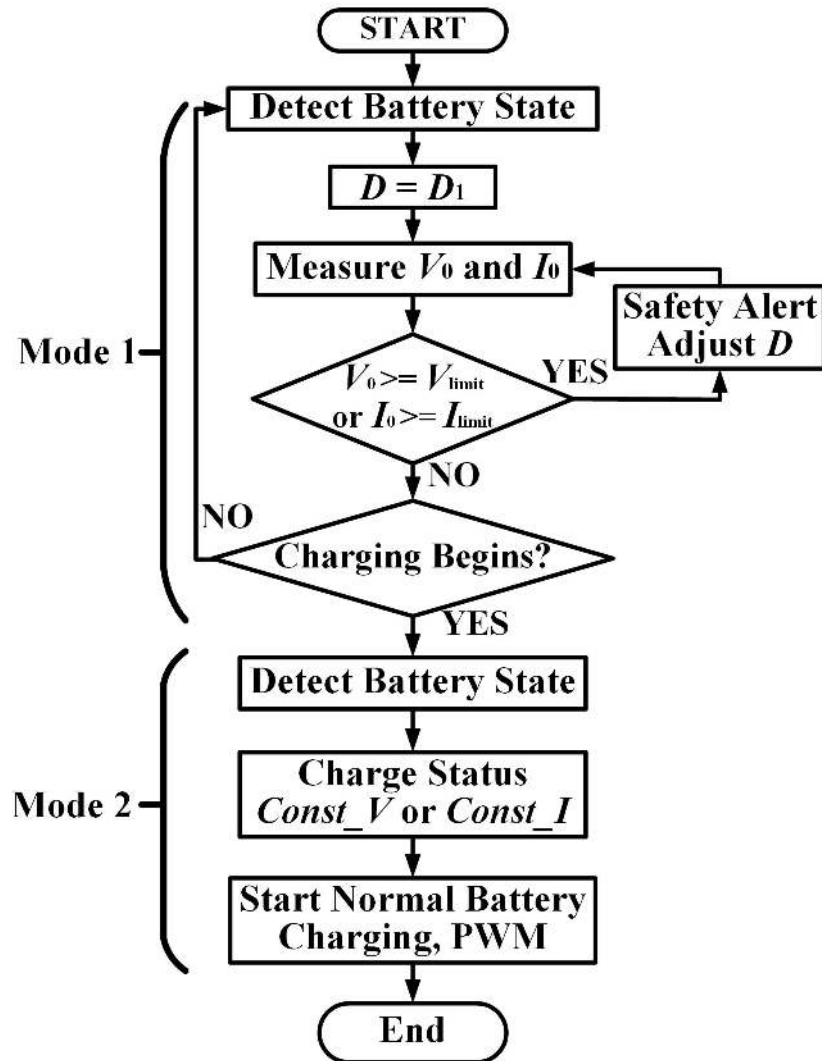
Fig. 4.4. The dual-mode operation of the DC-DC converter.

4.6. Design Process of On-board Chargers

An overview of the design process of the on-board charger for a universal inductive charging system is shown in Fig. 4.5. First, the S-connected LC is the optimal topology of the secondary resonant circuit. Designers need to estimate the value of the secondary inductance and capacitance. Based on the standard input voltage of the primary charger and the nominal output voltage of the secondary LC circuit, the value of L_2 can be calculated according to Eq. (1) and C_2 can be calculated based on the resonant frequency. The voltage tolerance of C_2 must be higher than the voltage stress on C_2 when the load is the heaviest. Secondly, the specific parameters of the receiving pad are determined, such as size and number of coil turn. A ferrite framework or isolation plate can be added to isolate the magnetic radiation from the receiving coils to the EV chassis. After finishing the initial design, the designer needs to accurately calculate L_2 again by simulations and further adjust the design, making sure that L_2 and C_2 satisfy all the requirements. Thirdly, the standard design of the DC-DC step-up converter (Mode 2) is the same as the common process of designing a step-up converter. The design parameters mainly include a nominal V_{out} for the secondary LC circuit, possible load range, and the standard charging characteristics of the EV batteries. Fourthly, the Mode 1 operation is determined. The duty cycle D_1 is calculated by the possible input voltage of the DC-DC converter and the limited charging voltage and current of the batteries, as

$$V_o = V_{1,\text{mode}\_1} \cdot G_{DC-DC,D_1} < V_{\text{limit}}, \tag{4.3}$$

where V_{1,mode_1} is the input voltage of the DC-DC converter during the frequency tracking calculated by Equation (4), $G_{\text{DC-DC,D1}}$ is the voltage gain of the DC-DC converter when

the duty cycle is D_1, and V_{limit} is the highest voltage allowed for batteries. Finally, the threshold value V_c must be higher than the highest possible V_1 during the frequency tracking.

```
                    ┌─────────┐
                    │  Start  │
                    └────┬────┘
                         │
         ┌───────────────▼──────────┐      ╱ L₁, C₁, V&I levels, f₀,
         │  Estimate L₂ and C₂      │◄──────  voltage tolerance of C₂
         └──────────┬───────────────┘
                    │
         ┌──────────▼───────────────┐
     ┌──►│  Coil design: shape,     │◄──────  Size limitation on coil
     │   │  size, turn N.O.,        │
     │   │  parallel wires, etc     │
     │   └──────────┬───────────────┘
     │              │
     │   ┌──────────▼───────────────┐
     │   │  Ferrite Framework       │◄──────  Radiation Isolation
     │   └──────────┬───────────────┘
     │              │
     │   ┌──────────▼───────────────┐
     │   │  Calculate L₂ and C₂     │
     │   └──────────┬───────────────┘
     │              │
     │   NO    ╱◄───▼────╲
     └────────  L₂ and C₂ ╲
              ╲ satisfied ╱
               ╲────┬────╱
                    │ YES
         ┌──────────▼───────────────┐
         │  DC-DC converter         │◄──────  Standard V₀, I₀, P₀, G
         │  design, Mode 2          │
         └──────────┬───────────────┘
                    │
         ┌──────────▼───────────────┐      Possible G, Vstart,
         │  Calculate D₁, Mode 1    │◄──── Limitations on V₀, I₀, P₀
         └──────────┬───────────────┘
                    │
                ┌───▼───┐
                │  END  │
                └───────┘
```
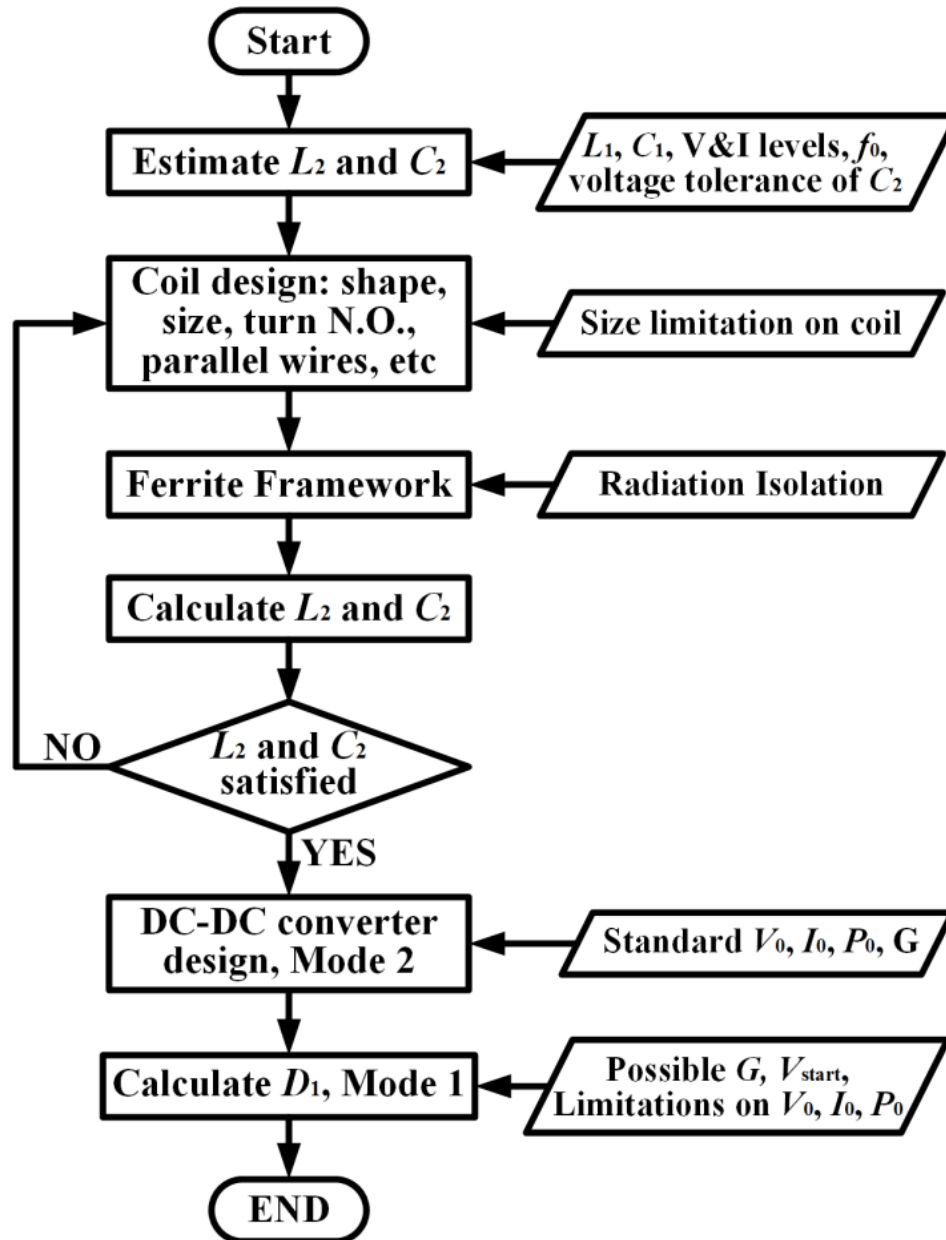
Fig. 4.5. The proposed design process of the on-board charger (AC-DC converter) used for universal inductive charging.

4.7.   Improvements by the Proposed Design

A dual-mode on-board charger is simulated by Simulink to test the applicability of the proposed system. The structure of the on-board charger used for simulations is identical to Fig. 4.1. The example parameters are the same as Fig. 3.2 (SS-connected topology). A dual-loop-controlled (feedback of the input current and the output voltage) boost converter is used as the DC-DC converter, with a nominal input voltage of 200V. Based on charging characteristics of batteries in Nissan Leaf, the equivalent resistance of the batteries R_{eq} ranges from 30 Ω to 400 Ω (from the heaviest to the lightest load). The charging voltage V_o starts from 300 V at the constant-current stage to 400 V at the saturation stage [29]. As a result, the duty cycle used in normal charging process ranges from 1/3 to 0.5. The input AC voltage during frequency tracking is V_{start} = 40 V. The theoretical f_1, f_1 tracked by the original UIC without the proposed the on-board converter, and f_1 tracked by the UIC with the dual-mode converter, are shown in Fig. 4.6. As proven in Fig. 4.6, the tracked f_1 with the dual-mode converter is more accurate than the value acquired without the proposed scheme. The reason for inaccuracy is that larger R_{eq} moves the zero-crossing point of the load-phase angle to a lower value away from the theoretical f_1, until the zero-crossing point is move to the resonant frequency. More importantly, f_1 cannot be tracked by the original UIC when the starting R_{eq} is too high. For example, the green line shows that f_1 cannot be tracked by the original UIC with the starting R_{eq} =200 Ω when M = 40 μH. The proposed on-board converter allows the system to track f_1 even though the starting R_{eq} is high, as R_{eq} is higher than 200 Ω when M = 40 μH (blue line), or R_{eq} is higher than 150 Ω when M = 30 μH (red line).
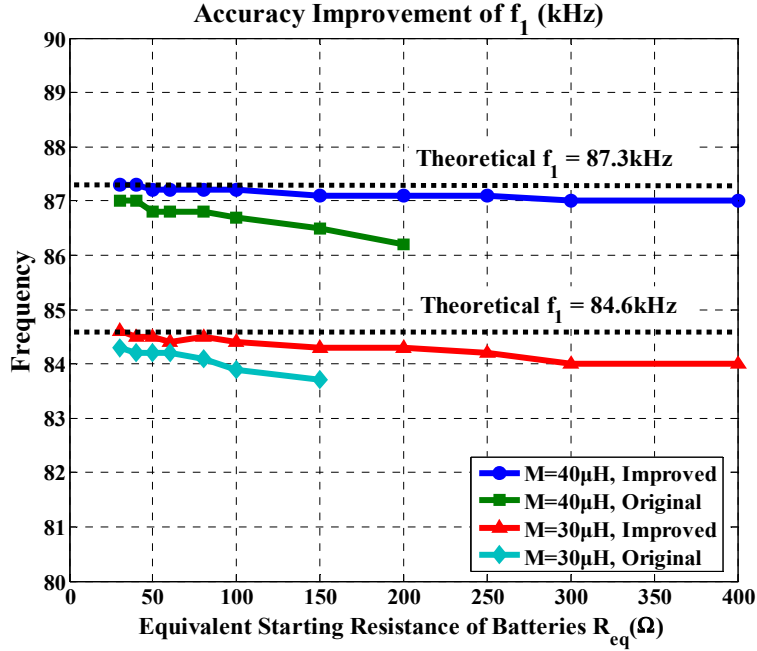
Fig. 4.6. Comparisons among f_1 tracked by the original UIC, and f_1 tracked by the UIC with the proposed converter, when the charging process starts with various R_{eq}'s and mutual inductances.

4.8. Experimental Validation

Based on the inductive charger (5 kW maximum power, variable-frequency control) used in [4], two different on-board chargers (AC-DC converters) are built, to test improvements of the proposed design scheme of on-board chargers. The two on-board chargers are used for charging batteries with different charging profiles. Hence, the receiving coils, resonant capacitors, the voltage and current levels of the back-end DC-DC converter, are different from each other, as listed in Table 4.1. The primary inductive charger used in the experiments is the same as the UIC in Chapter 3, with the same parameters in the simulations in Fig. 3.2. A boost converter is used as the back-end DC-DC converter on the load [99]. The boost converter is capable of working with the two resonant circuits. The input voltage ranges from 180 V to 280V and the highest input

Table 4.1. Parameters of the Two On-board Chargers

Parameters	Charger 1	Charger 2
Dimensions of Receiving Coil	SP, inner length 28 cm, outer length 40 cm.	CP, inner diameter 20 cm, outer diameter 42 cm.
Turn NO.	20 (2 threads)	27
Resonant Inductance	200.8 μH	315.5 μH
Resonant Capacitance	20.7 nF	13.2 nF
Nominal Input DC Voltage V_1	200 V	250 V
Output DC Voltage V_0	300 ~ 400 V	400 ~ 540 V
Equivalent R_{eq}	40 ~ 400 Ω	50 ~ 450 Ω
Threshold Voltage V_c	120 V	150 V

current is higher than 25 A rms. In experiments, both resonant circuits are combined with the boost converter separately, but the modulation is different, according to their own charging profiles. A control system is built based on DSP and FPGA for modulating the DC-DC converter. The DSP focuses on switch-signal calculations and FPGA does voltage and current measurement and generating gate-drive signals.

According to the equation of the voltage gain, the voltage gain G of the resonant circuits is approximately 1 with the charger 1, and approximately 1.25 with the charger 2. As a result, the nominal input voltage V_1 of the DC-DC converter is 200V in charger 1 and 250 V in charger 2. The threshold voltage V_c between the Mode 1 and the Mode 2 is set as 4 times V_{start} multiplied by the voltage gain at the fixed-gain point.

4.8.1. Experimental Results with Charger 1

When the load contains the Charger 1, the voltage gain of the resonant circuits vs. the equivalent resistance R_{eq}, is measured in experiments, as shown in Fig. 4.7(a). In the frequency-tracking process (Mode 1), the duty cycle of the DC-DC converter D_1 is from 0.7 to 0.8, depending on starting R_{eq}. By practical measurements, the error of G is maintained in a range of ±8% with various air gaps. With a fixed air gap, G is stable during charging cycles: the range of the voltage variances vs. R_{eq} is maintained in ±5%. In experiments, the tracked f_1 is different when the charging process starts with a heavy (R_{eq} = 40 Ω), medium (R_{eq} = 100 Ω) or light (R_{eq} = 200 Ω) load. As proven in Part B, Chapter II, the heavier the starting load is (starting R_{load} is smaller), the more accurate the tracked f_1 will be. In Fig. 4.7(a), a larger starting R_{eq} leads to a lower f_1, meaning that the zero-crossing point of the DC-characteristics curve is shifted from the theoretical f_1 to lower values. The smaller range of the voltage gain vs. varied R_{eq} with a lower starting R_{eq}, also proves that f_1 is more accurate when the charging process starts from a heavier load. Therefore, the experimental results match the simulation results well. Meanwhile, the value of f_1 is reduced when the air gap is increased to be Air 2. This phenomenon is also proven by the simulation results in Fig. 3.2: a lower M leads to lower f_1. Moreover, the increased air gap also influences the accuracy of the tracked f_1: with the same starting R_{eq}, the range of the voltage gain vs. R_{eq} becomes larger when the air gap increases.
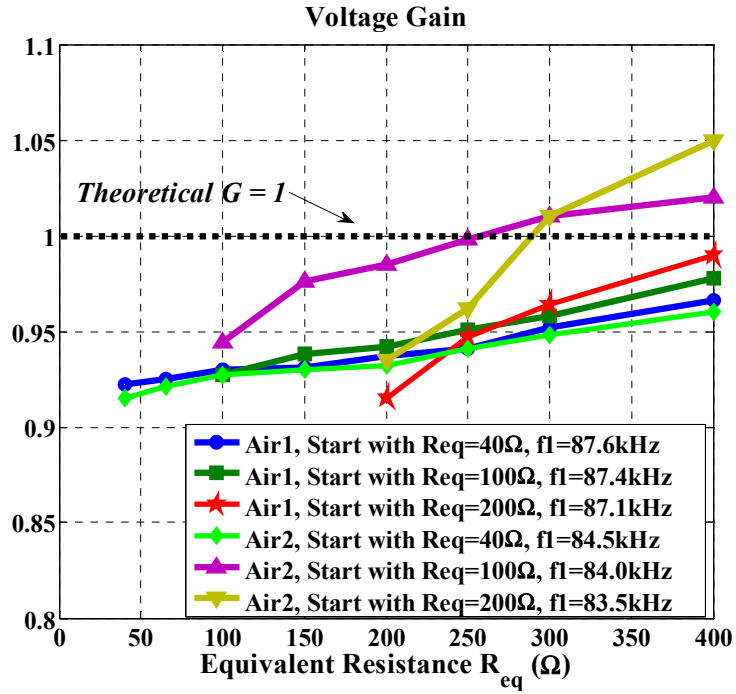
(a)
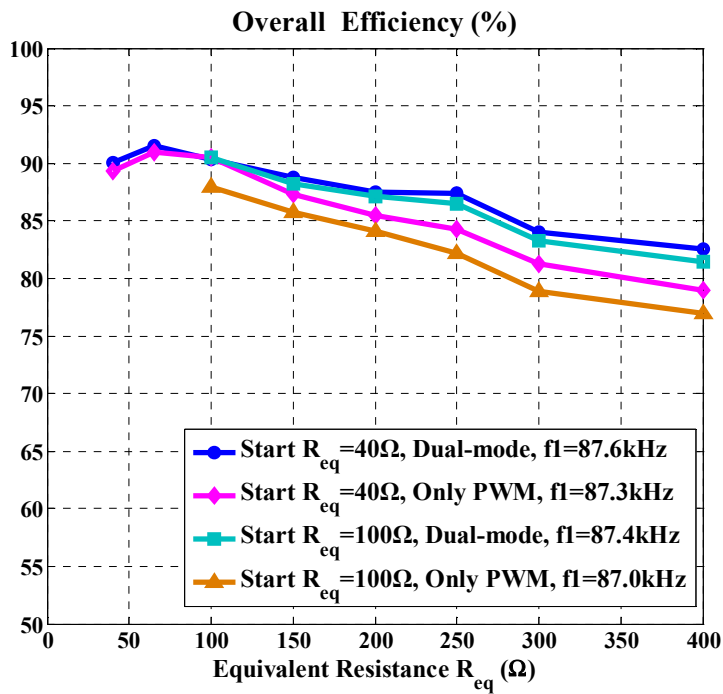
(b)

Fig. 4.7. Experimental results of Charger 1: (a) with two air gaps: Air 1 = 12 cm and Air 2 = 17 cm, the voltage gain vs. R_{eq}, when the starting R_{eq} = 40, 100, or 200 Ω, and (b) the overall efficiency vs. R_{eq}, if Charger 1 is controlled by the dual-mode scheme or only PWM during frequency tracking, with Air 1 and the starting R_{eq} = 40 or 100 Ω.

Comparing Charger 1 with the dual-mode control or only PWM, the overall efficiency from the DC input of the primary DC-AC converter to the output of the on-board DC-DC converter is shown in Fig. 4.7(b). With the same starting R_{eq} (40 or 100 Ω) but the dual-mode modulation of the on-board charger, the overall efficiency is higher than the charger controlled by PWM only, especially when the load becomes light. The obviously different efficiency with a light load is caused by different reflected R_{load} seen by the resonant circuits. Two systems reflect different values of R_{load} when the R_{eq} is the same and the variance of R_{load} becomes larger when load is lighter. As shown in Fig. 3.2, the voltage gain of the LC circuits may be increased to be higher than the nominal fixed gain when the load becomes light, because f_1 is not accurately controlled. Therefore, the input of the on-board charger is higher than the nominal value. To provide a constant output voltage, the reflected impedance R_{load} with a higher input voltage V_1 of the on-board charger is much larger than the value of R_{load} when V_1 is relatively constant. According to the common efficiency trends in IPT systems, the overall efficiency with higher R_{load} is lower [4, 29]. In another aspect, the on-board DC-DC converter commonly has the highest efficiency when a duty cycle is around 0.5 because of harmonics' influence. The efficiency difference caused by DC-DC converter also becomes more significant when the load becomes light since the input voltage is increased and the duty cycle needs further adjustment. For further efficiency improvement, synchronous rectifier or interleaved converter can be applied to replace the common boost converter.

4.8.2. Experimental Results with Charger 2

When the load contains Charger 2, the voltage gain of the resonant circuits is measured in experiments, as shown in Fig. 4.8. The duty cycle of the DC-DC converter

D_1 is also 0.7 during frequency-tracking process. Similar to the results in Charger 1, the error of G is limited a range of ±8%, with various starting R_{eq} and air gaps. The accuracy of the tracked f_1 is reduced when the charging cycle starts with a lighter load (a higher R_{eq}). However, the range of the measured voltage gain in the Charger 2 is smaller than the voltage-gain range in the Charger 1. In fact, the tracked f_1 with the Charger 2 is more accurate because of tighter mutual coupling. In other words, if the mutual inductance M is increased and the resistance R_{load} is fixed, the zero-crossing point of the load-phase curve will be closer to the theoretical f_1, with the same R_{eq}. The overall efficiency of the system is also similar to the results with Charger 1.

Compared with the tracked frequencies without the on-board charger, the tracked frequency with the on-board charger is more accurate. Moreover, the variances of the
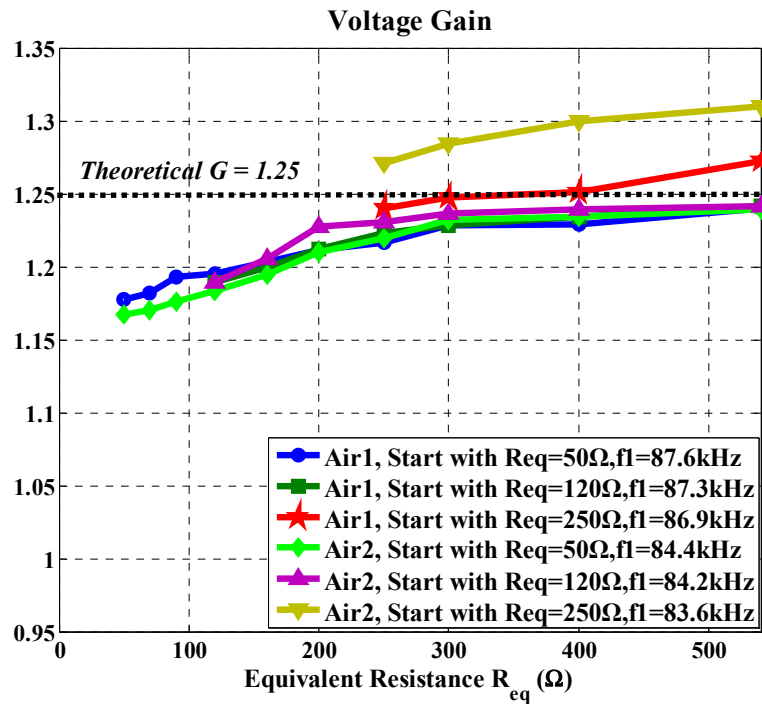
Fig. 4.8. With two air gaps: Air 1 = 12 cm and Air 2 = 17 cm, the measured voltage gain of resonant circuits, when Charger 2 starts with various R_{eq} = 50, 120, or 250 Ω. The duty cycle of the DC-DC converter during frequency tracking (Mode 1) D_1 is 0.7.

voltage gain vs. the load resistances are smaller than the voltage gain of the system without the on-board charger. Note that the charging voltage on batteries V_o is not shown here because it is a good output with either on-board charger when the input voltage of the back-end DC-DC converter is stable.

In summary, the practical experiments demonstrate the applicability of the proposed on-board chargers. Based on the proposed on-board AC-DC converter, the frequency at the fixed-gain point f_1 can be adaptively tracked and the input of the back-end converter is universally maintained stable during the charging process. More importantly, the specially-controlled DC-DC converter makes it possible for the IPT system to track f_1 when the starting R_{eq} is high. Without Mode 1 operation of the DC-DC converter, f_1 cannot be tracked when R_{eq} is too high (for example, higher than 120 Ω in Charger 1). The accuracy of the tracked f_1 is seriously influenced as well. Besides accurately tracked f_1, the dual-mode modulation of the on-board charger also leads to higher overall efficiency, especially in light-load conditions.

4.9. Chapter Summary

In this Chapter, a scheme of designing a dual-mode on-board charger is developed. The proposed on-board charger works in coordination with a previously proposed UIC. The design includes two aspects: the design of the *LC* circuit and the receiving coil and the design and operation of the DC-DC converter. An S-connected *LC* was proven to be a better type of resonant circuits for the on-board AC-DC converters, because the fixed-gain point the resonant circuits can be universally and more accurately tracked. A non-polarized pad in the similar size as the transmitting pad is preferred as the design of the receiving pad, because of its higher coupling coefficient and power transfer capability. A

simple and low-cost control method based on dual-mode operation was applied for more accurately tracking the optimal frequency. Simulations and hardware experiments demonstrate the universality of the proposed design and a better accuracy of system operation.

Despite the fact that the S-connected secondary *LC* circuit has many advantages, a P-connected *LC* circuit has its own pros. For example, the P-connected *LC* acts as a constant current source vs. various load resistance. The performance is more suitable for battery charging. Moreover, from the view of the universal charging, a design scheme of the on-board chargers with a P-connected secondary *LC* circuit must be analyzed as well.

CHAPTER 5: DESIGN OF ON-BOARD CHARGERS WITH P-CONNECTED LC RESONANT CIRCUITS

5.1. Overview

A UIC of EVs and a dual-mode on-board charger with an S-connected *LC* circuit are proposed in previous two Chapters. The UIC is capable of charging different EV models even with the influences of varied magnetic coupling and various receiving coils. For on-board chargers, S-connected *LC* circuits prove to be the optimal resonant topology of the load-side charger for universal inductive charging. However, P-connected *LC* circuits have some advantages over S-connected *LC* circuits, such as a much lower voltage stress on the resonant capacitor and a smaller range of the optimal frequencies for stable charging voltage [117]. Moreover, a P-connected *LC* circuit works as a current source that is more suitable for battery charging [115]. The definition of the UIC requires a design standard of on-board chargers containing P-connected *LC* circuits, before realizing the "real" universal inductive charging.

By previous analysis, there are challenges of applying P-connected *LC* circuits in on-board chargers. First, with a P-connected *LC* circuit on load side, the voltage control of the universal inductive charger may not be stable enough, because the voltage gain varies sensitively vs. frequency. According to the curves of the voltage gain in Fig. 3.2(b), when R_{load} is small, a tiny error of the AC frequency from the fixed-gain point leads to a distinct difference from the fixed voltage gain. Another challenge for the inaccurate frequency control is from the equivalent load-phase angle of the *LC* circuits. According to theoretical calculations, the load-phase angle is slightly lower than 0 when the

frequency is at the fixed-gain point. In other words, the zero-crossing point of the load-phase angle is higher than the fixed-gain point. Therefore, the voltage gain with an inaccurate frequency cannot be maintained stable. Moreover, the difference between the fixed-gain point and zero-crossing point of the load-phase angle increases when the load resistance R_{load} increases. The error is exacerbated in practical applications, because of parasitic resistance on coils. As a result, with a SP topology, the fixed-gain point cannot be accurately tracked and a stable voltage gain vs. R_{load} is difficult to be maintained. The existing problems of SP-connected LC circuits must be solved before realizing the real universal inductive charging.

This Chapter proposes a specifically designed on-board charger used for universal inductive charging, based on a P-connected secondary LC circuit. Higher efficiency and more accurate control can be achieved, compared with the on-board charger applying traditional P-connected resonant circuit. Section 5.2 describes a specifically designed on-board charger consisting of P-connected LC circuits. A step-down converter is selected as the on-board DC-DC converter. To improve the accuracy of tracking frequency and maintain soft switching of the primary DC-AC inverter, an additional inductor is series connected to the P-connected LC circuit. Section 5.3 analyzes the advantages of the proposed secondary resonant circuit: a much smaller range of optimal frequencies and a lower voltage stress on the resonant capacitors. Section 5.4 lists experimental results that are used to validate the proposed design.

5.2. On-board Chargers with P-connected LC Circuits

5.2.1. Application of a Step-down DC-DC Converter

Based on the calculation results in Fig. 3.2, if the load contains a P-connected LC circuit and the AC frequency is at the fixed-gain point, the voltage gain keeps constant within varied load conditions, as

$$G = \left| \frac{V_{out}}{V_{in}} \right| = \frac{L_2}{M}. \tag{5.1}$$

According to the design of the charging interfaces in Chapter 4, a larger receiving pad leads to better coupling and higher power-transfer capability. A reasonable design of the receiving pad has a similar size of the transmitting pad, because of the tighter coupling and higher power-transfer capability when the size of the receiving pad is limited. If the coupling coefficient ranges from 1/8 to 1/4, the fixed voltage gain ranges from 8 to 4. The fixed voltage gain may be too high for charging EV batteries when the coupling coefficient is low enough. Thus, the on-board AC-DC converter can be formed by a diode rectifier and a step-down converter, converting the voltage to a lower value. For example, when the DC input V_{in} is 200V, the output voltage of diode bridge following the secondary resonant circuit typically ranges from 800Vrms to 1600Vrms, in the RMS value. In a typical example, the standard charging voltage of the EV battery pack of Nissan Leaf starts from 300 V to 420 V during the charging process (from the heaviest to the lightest load condition). Thus, the duty cycle D of the step-down converter applied ranges from 0.525 to 0.1875.

The application of a step-down converter has another advantage. The equivalent resistance reflected from the batteries to the output of the secondary resonant circuit is larger than the equivalent resistance of the batteries themselves. Therefore, the voltage gain around the fixed-gain point is stable vs. the AC frequency. If the step-down

converter is a BUCK converter, the equivalent resistance looking from the output of the

secondary resonant circuit can be approximately calculated by

$$R_{load} \approx \left(1/D^2 \right) R_{eq} \cdot p_{DC \to AC}, \tag{5.2}$$

where $p_{DC \to AC}$ is the parameter to convert the resistance at the DC output of the on-board

AC-DC converter to the resistance at the AC output of the secondary LC circuit. With a

step-down converter, a larger value of R_{load} means more stable output voltage of the

secondary LC circuit, because the voltage gain is more sensitive to the frequency variance

when R_{load} is smaller. Therefore, the output voltage of the secondary LC circuit or the

voltage gain is more stable, when the on-board AC-DC converter is a step-down

converter. For example, let the LC circuits be the design in Table 5.1. When the coupling

coefficient $k = 0.20$, the voltage gain at the fixed-gain point is $G = 5$. A buck converter is

used to charge EV batteries with the nominal voltage 400 V. The duty cycle of the buck

converter will be around 0.4. $R_{load} = 200 \sim 1520$ Ω when $R_{eq} = 40 \sim 300$ Ω in common

load conditions. Based on this design, the curves of DC characteristics vs. AC frequency

are shown in Fig. 5.1.

Table 5.1. Parameters in Simulations of SP-connected LC Circuits

Parameters	Values
Primary L_1	200 μH
Primary C_1	19.79 nF
Secondary L_2	200 μH
Secondary C_2	19.79 nF
Mutual M	40 μH
Load R_{load}	200, 250, 300, 400, 500, 600, 800, 1000, 1200, 1600 Ω
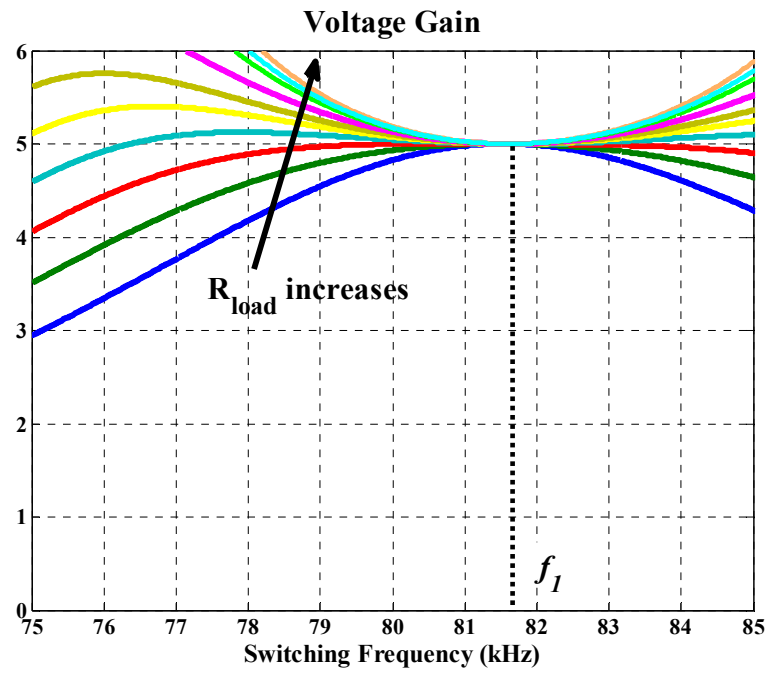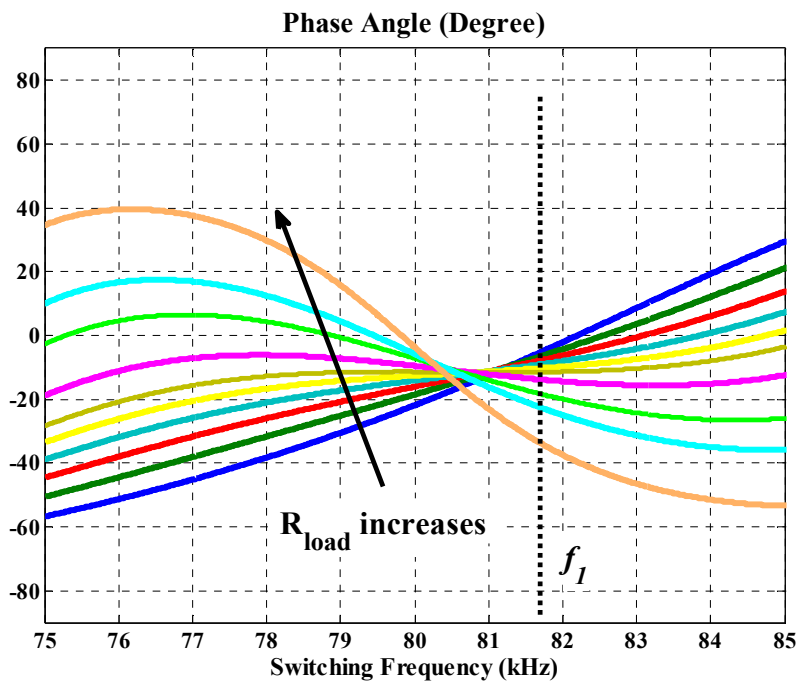
Fig. 5.1. The simulated curves of (a) the voltage gain and (b) the load phase angle vs. the AC frequency in the SP-connected *LC* (resonant frequency of both *LC* circuits is 80 kHz).

In Fig. 5.1, the voltage-gain curves vary from a bulge to a hollow when equivalent load resistance R_{load} increases. The variation trend of the voltage gain vs. AC frequency is much more stable than the curves in Fig. 3.2. However, the zero-crossing points of the load-phase-angle curves are shifted from the fixed-gain point f_1. When R_{load} increases, the zero-crossing point of load-phase angle moved to be higher and then be lower than f_1. When R_{load} is large enough ($\geq$ 600 Ω), the load-phase-angle curves vs. AC frequencies vary in different trends and the zero-crossing point becomes lower than f_1. Moreover, there is a range of R_{load} without zero-crossing point of load-phase angle. Therefore, the fixed-gain point f_1 still cannot be accurately tracked in the full range of R_{load}. Besides unstable voltage gain and the inaccurately tracked frequency, the load-phase angle is always lower than zero, meaning ZVS of primary DC-AC inverter is not achieved. ZVS cannot be maintained even if f_1 is accurately tracked. So, the fixed voltage gain of resonant circuits and high-efficiency operation of the DC-AC inverter cannot be achieved.

5.2.2. Application of an Additional Inductor

According to previous analysis, the zero-crossing point of the load-phase-angle curve shifts from the fixed-gain point f_1 when the load resistance R_{load} becomes larger. Thus, the frequency at the fixed-gain point cannot be accurately tracked. Moreover, the load-phase angle at the fixed-gain point is lower than 0, meaning that ZVS of the primary DC-AC inverter cannot be adaptively achieved. To more accurately track the fixed-gain point f_1, an additional inductor is added in series with the secondary LC circuit (similar to "LCL" circuit), as

$$L_{S2} = \eta_2 L_2.$$
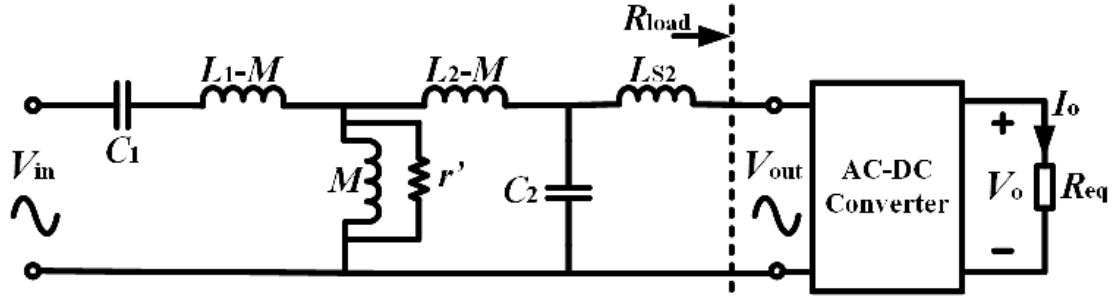
Fig. 5.2.   The equivalent topology of the system with a P-connected secondary LC circuit and an additional inductor L_{S2}.

The equivalent circuit of the system with the additional inductor is shown in Fig. 5.2. Based on the previously used UIC, the DC characteristics with a secondary "LCL" circuit ($L_{S2} = 8$ µH) are calculated, as shown in Fig. 5.3. In Fig. 5.3, a reasonable value of L_{S2} makes the zero-crossing point of the load-phase angle locate at fixed-gain point f_1. Because the tracked frequency is usually higher than f_1, the load-impedance angle is higher than 0 in the heavy load conditions: $R_{load} = 200 \sim 600$ Ω. Therefore, ZVS operation of the primary DC-AC inverter is achieved in heavy load conditions (high input current).

When L_{S2} is small, the voltage gain is approximately same as Equation (5.1). When the mutual inductance M decreases to the lowest value ($M = 20$ µH, $k = 0.1$) in the common range, the DC characteristics are shown in Fig. 5.4. In Fig. 5.4, when M is reduced, the fixed-gain point is moved towards the resonant frequency. When the AC frequency is set to be the fixed-gain point, the load-phase angle is always higher than 0, leading to durative ZVS of the DC-AC inverter.

Voltage Gain

R_{load} increases

f_1

Switching Frequency (kHz)

(a)

Phase Angle (Degree)

R_{load} increases

f_1

Switching Frequency (kHz)
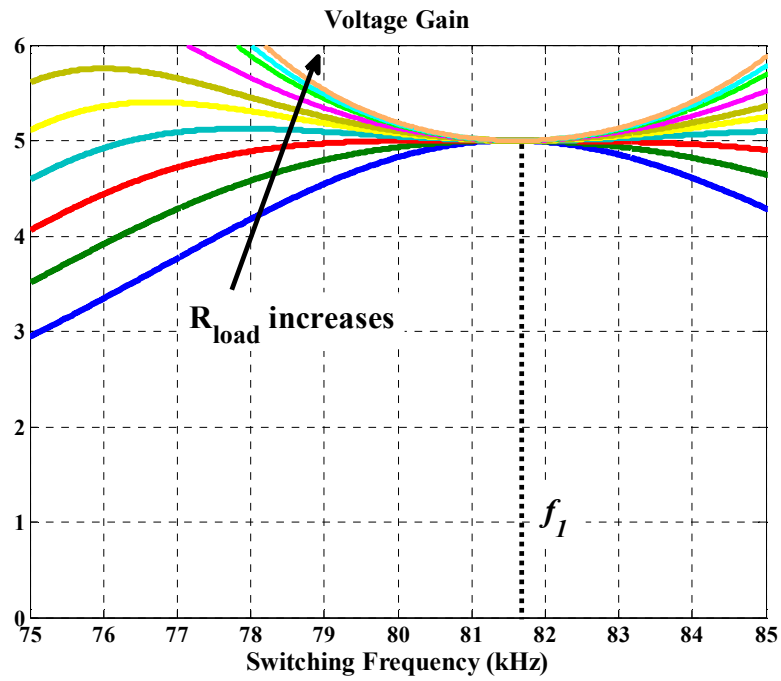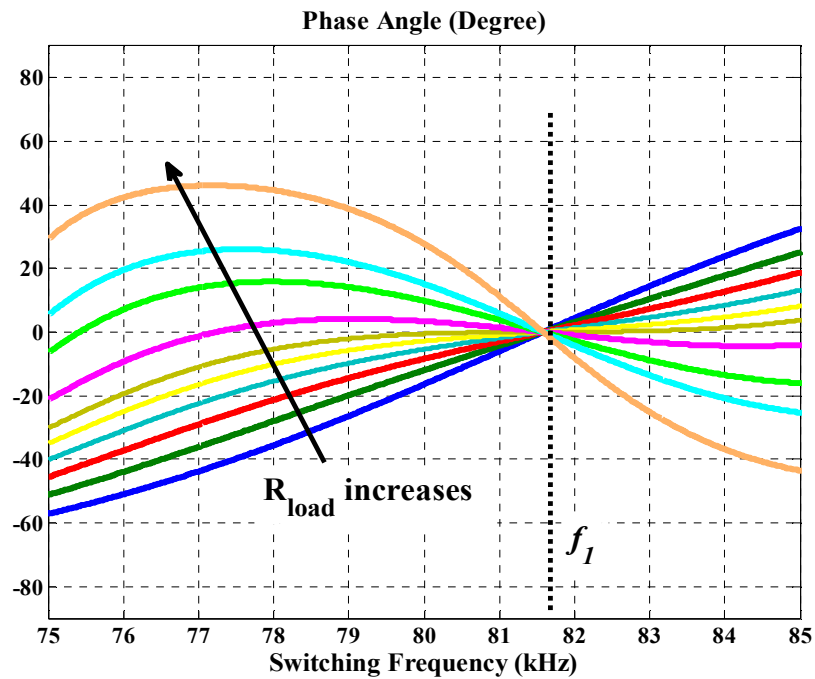
(b)

Fig. 5.3. The curves of (a) the voltage gain and (b) the load phase angle vs. the AC frequency in the SP-connected *LC* with $L_{S2} = 8$ μH. Other parameters are same as Table 5.1.

As a result, the value of L_{S2} is determined, based on the condition that all load-phase-angle curves with the maximum M have the same zero-crossing point locating at the fixed-gain point. After choosing L_{S2}, ZVS operation of the DC-AC inverter can be maintained in all load condition, when M is equal to or smaller than the maximum value.

In another respect, when R_{load} becomes higher, the zero-crossing point of the load-phase angle is moved to be lower. This means that the accuracy of frequency tracking is reduced. However, according to the standard range of the AC frequency applied in EV
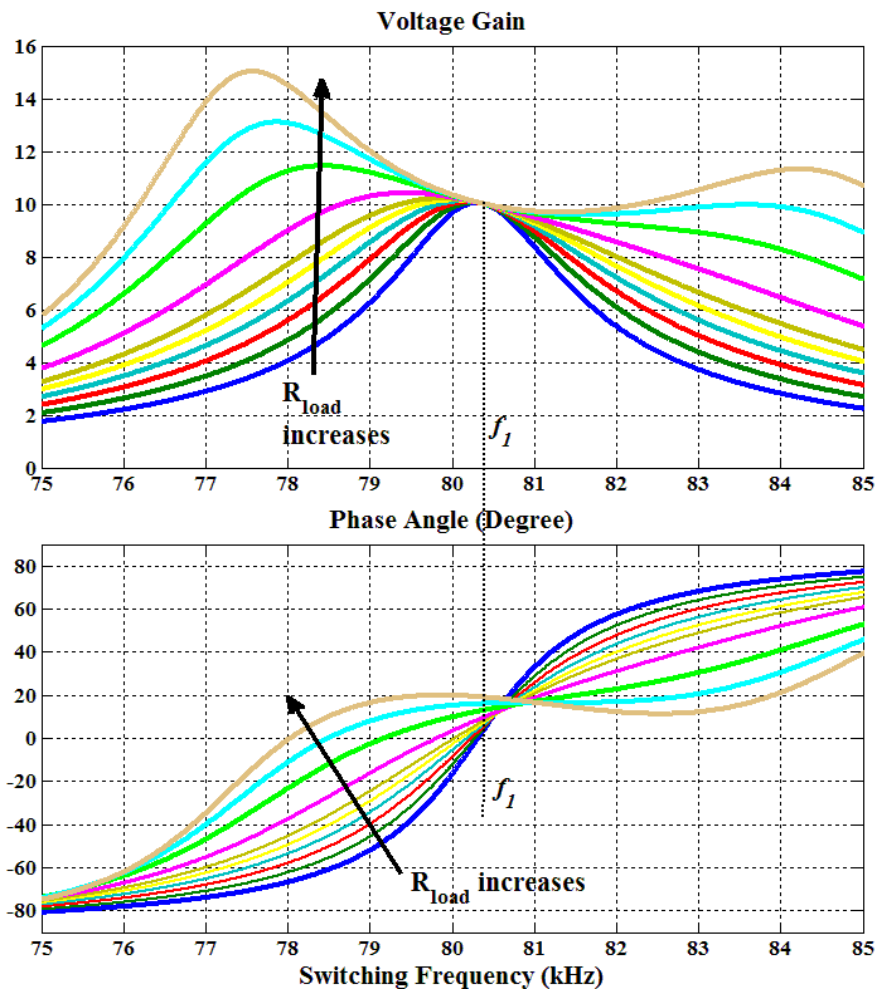
Fig. 5.4. The curves of (a) the voltage gain and (b) the load-phase angle vs. the AC frequency in the SP-connected circuits with $L_{S2} = 8$ μH. $M = 20$ μH ($k = 0.1$). Other parameters are same as Table 5.1.

wireless charging, the switching frequency cannot be lower than 80 kHz. Thus, the frequency is set as the lowest frequency in the standard, if the tracked frequency is lower than the low boundary of the standard. Although the voltage gain will vary during the charging process, the range of variation is small ($G = 9.5 \sim 10.8$). More importantly, ZVS of the DC-AC inverter is still maintained.

5.3. Performance Analysis of the Proposed On-board Charger

5.3.1. A Smaller Range of Frequency Variations

Compared with IPT system containing an S-connected secondary LC circuit, the system containing a P-connected secondary LC circuit has a much smaller range of the fixed-gain point, when the range of the coupling coefficient k is fixed. By circuit analysis in Chapter 3, the fixed-gain point f_1 of the SS-connected LC circuits is

$$f_1 = \sqrt{\frac{\sqrt{L_2}}{C_1(L_1\sqrt{L_2} - M\sqrt{L_1})}} / 2\pi = \sqrt{\frac{1}{(1-k)}} \cdot f_0, \tag{5.3}$$

where f_0 is the resonant frequency of the LC circuits, and k is the coupling coefficient. When the secondary LC circuit is P-connected, the frequency at the fixed-gain point f_1 is

$$f_1 = \sqrt{\frac{L_1}{C_2(L_1L_2 - M^2)}} / 2\pi = \sqrt{\frac{1}{1-k^2}} \cdot f_0. \tag{5.4}$$

As a result, the range of the fixed-gain point f_1 with a P-connected LC circuit on load is much smaller than the range of f_1 with an S-connected LC circuit. For example, let $k = 1/8 \sim 1/4$. The range of f_1 with an S-connected secondary LC circuit is $(1.155 \sim 1.069) \cdot f_0$, and the range of f_1 with a P-connected secondary LC circuit is $(1.033 \sim 1.008) \cdot f_0$.

When the resonant frequency of all LC circuits is $f_0 = 80$ kHz, the range of f_1 vs. k with a P-connected secondary LC circuit is in 2 kHz, a value that is much smaller than the range with an S-connected secondary LC circuit: 7 kHz. Moreover, in Fig. 5.3, when the coupling is in guaranteed to be tight enough (for instance, $k > 0.15$ and possible range of k is small), the variation of the voltage gain is small ($< 3\%$) in the 2-kHz-frequency range. This means the charger can apply a constant-frequency control.

5.3.2. A Lower Voltage Stress on Resonant Capacitors

A problem of designing an inductive charging system for EVs is the high voltage stress on resonant capacitance. Because of high-frequency (> 80 kHz) AC power and a high current level (maximum 20 A RMS), the highest voltage on the resonant capacitance can be higher than 2000 Vrms. The high voltage stress on resonant capacitance requires high voltage tolerance of the resonant capacitors in the hardware system. In practical designs, researchers need to series connect capacitors to reduce the voltage stress on each capacitor. A P-connected secondary LC circuit has significantly lower voltage stress on the resonant capacitor than the value of an S-connected secondary LC circuit.

For comparing the voltage levels on resonant capacitances in different LC topologies, let an SS-connected LC topology and an SP-connected LC topology have the identical L_1's, L_2's, C_1's, and C_2's. The range of load resistances and the range of possible coupling coefficients are the same for two topologies. For an SP-connected LC topology, the voltage on C_2 is equal to the output voltage of the secondary LC circuit, as

$$V_{C2,SP} = V_{out,SP}.$$

For an SS-connected LC topology, the voltage on C_2 is calculated by

$$V_{C2,SS} = \frac{V_{out,SS}}{R_{load,SS}} \cdot Z_{C2,SS} = \frac{V_{out,SS}}{R_{load,SS}} \cdot \frac{1}{(j\omega C_2)_{SS}} .$$

At the fixed gain point, the ratio between the RMS output voltages of the two topologies

is

$$\frac{V_{out,SP}}{V_{out,SS}} = (\frac{L_2}{M} \cdot V_{in}) / (\sqrt{\frac{L_2}{L_1}} \cdot V_{in}) = \frac{1}{k} .$$

As a result, the ratio between the voltage levels on C_2 in two topologies is

$$\frac{V_{C2,SP}}{V_{C2,SS}} = \frac{1}{k} \cdot \frac{R_{load,SS}}{Z_{C2}} = \frac{(1-D_{SS})^2 \cdot R_{eq} \cdot (8/\pi^2)}{k \cdot Z_{C2,SS}} , \tag{5.5}$$

where D_{SS} is the duty cycle of the on-board DC-DC converter in nominal condition. The

$V_{C2,SP}$ becomes the maximum when k is the smallest. The $V_{C2,SS}$ becomes the maximum

when R_{eq} is the smallest. Based on the previous example, if $L_1 = L_2$, the voltage gain at

the fixed-gain point is nearly 1 and the theoretical $D_{SS} = 0.5$. Also, k ranges from 1/8 to

1/4 and $R_{eq,min} = 40\ \Omega$. With the roughly applied switching frequency $f_{sw} = 80$ kHz, $Z_{C2} =$

104.55 Ω. Therefore,

$$\frac{V_{C2,SP,max}}{V_{C2,SS,max}} = 0.6 .$$

As a result, the voltage on C_2 in an SP-connected topology is lower than the value in an

SS-connected topology. In practical applications, the self-inductance of the receiving coil

L_2 is designed to be smaller than L_1, in order to avoid a too high output voltage of the P-

connected secondary LC circuit with a loose coupling effect, according to Equation (1).

V_{C2} is further reduced if L_2 is smaller than L_1.

5.4. Experiment Results and Analysis

Similar to the on-board charger with an S-connected LC circuit, an on-board charger with a P-connected LC (LCL) circuit is built, to work with the previously-used UIC. The parameters of hardware are listed in Table 5.2. Note that equivalent load resistances are used to represent power consumption of an on-board DC-DC converter (a step-down converter) and batteries. The range of R_{load} in Table 5.2 is used as the equivalent resistance of batteries (R_{eq}) varying from 50 to 250 Ω, when the voltage-step-down ratio of the DC-DC converter is 0.5.

Based on the hardware system, the normalized voltage gain of the resonant circuits vs. R_{load} is shown in Fig. 5.5, with three air gaps. For different air gaps, the tracked AC frequency is reduced when magnetic coupling is reduced. From the curves of the normalized voltage gain, the error between the theoretical and practical values is maintained in a range of (-10%) ~ (12%). The measured range is much smaller than the range of the voltage gain when the frequency is set as other values. One reason for variance of the voltage gain vs. load resistance is that the AC frequency is not chosen as

Table 5.2. Parameters of the LCL Secondary Circuit

Parameters	Values
Dimensions of Receiving Coil	SP, inner length 24 cm, outer length 40 cm.
Turn NO.	15
Coil Inductance	135.5 µH
Resonant Capacitance	29.21 nF
Additional Inductor	5.0 µH
Equivalent R_{load}	200, 250, 300, 350, 450, 550, 700, 1000 Ω

the exact fixed-gain point. By theoretical results in Fig. 5.3, if the AC frequency is close to the fixed-gain point but not at the exact fixed-gain point, the voltage gain increases as the equivalent load resistance R_{load} increases. Another reason for variance of the voltage gain is from the voltage drop by parasitic components in the practical circuit, such as parasitic resistance of coils. The voltage drop of coil resistance is larger when the current is higher, as R_{load} is smaller. Similar to the system with SS-connected LC circuits, the voltage gain varies in a larger range when air gap increases. When the air gap increases, the influence on the voltage gain by inaccurately tracked frequency becomes more serious, because the voltage variance by parasitic components in the primary side becomes larger when magnetic coupling is reduced.

Fig. 5.5. With three air gaps, the measured voltage gain vs. load resistance of an inductive charging system with an LCL secondary circuit.

The system efficiency (from the DC input of the primary inverter to the output of the secondary resonant circuit) vs. R_{load} is shown in Fig. 5.6, with three air gaps. The system efficiency is reduced when the air gap increases. Different from SS-connected resonant circuit, the efficiency increases when load resistance increases. The reason for the efficiency variance is from the equivalent model of an SP-connected structure, as a constant-current source. This is similar to the efficiency trend of a constant-current model, which has higher output power and efficiency when R_{load} becomes larger, although the proposed control method realizes a constant-voltage output of the system.

Finally, the tracked frequencies vs. air gap also demonstrate the small range of the
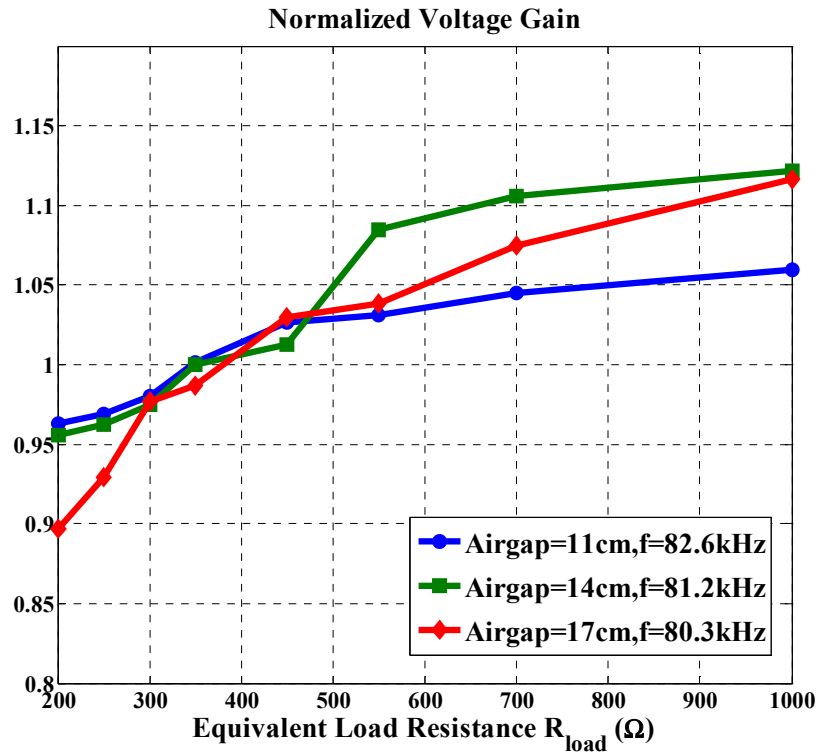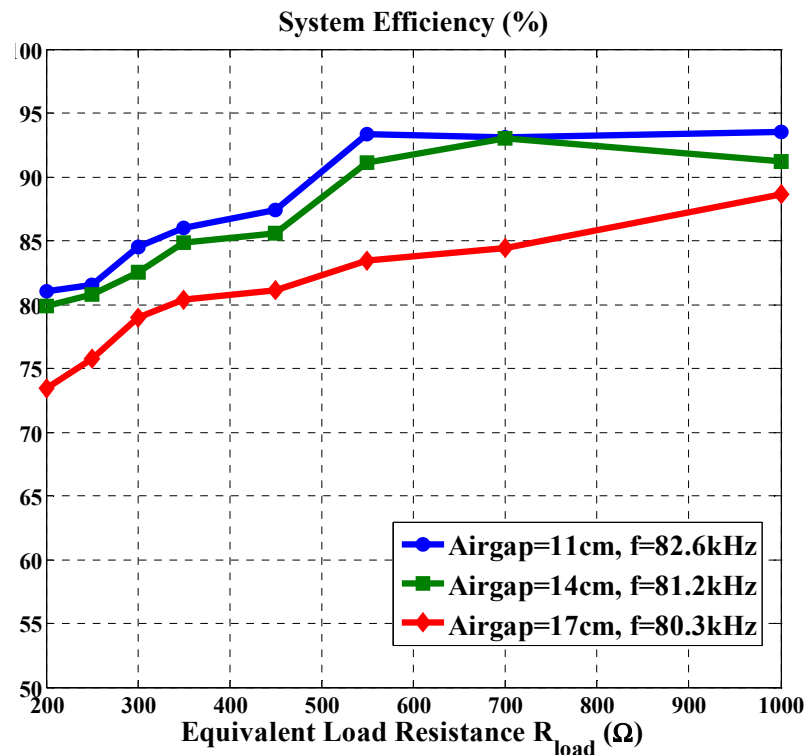
System Efficiency (%)

Fig. 5.6. With three air gaps, the measured system efficiency vs. load resistance of an inductive charging system with an *LCL* secondary circuit.

optimal frequency (80.3 ~ 82.6 kHz) with various magnetic coupling.

5.5. Chapter Summary

In this Chapter, an on-board charger with a P-connected *LC* circuit is proposed, to work in coordination with the UIC. The proposed scheme of designing the on-board charger finally achieves universality of the inductive charging system. The on-board charger applies a P-connected *LC* circuit, with an additional inductor connected in series with the resonant tank. The "*LCL*" structure leads to the equality of the fixed-gain point and the zero-crossing point of the load-phase-angle curves. A voltage-step-down DC-DC converter is used to provide standard charging voltage and current to EV batteries. The input/output characteristics of the step-down converter also stabilize the voltage gain of the resonant circuits vs. the AC frequency. Simulations and hardware experiments are applied to demonstrate the advantages of the proposed design: better universality to varied load conditions and magnetic coupling, more accurate frequency control, much smaller range of frequencies, and lower voltage stress on resonant capacitors. From simulation and experiment results, the frequency at the fixed-gain point can be more accurately tracked when the load resistance is smaller. This means a dual-mode control method of can be applied when the secondary resonant circuit is P-connected.

CHAPTER 6: HARDWARE SYSTEMS

To validate the applicability of the proposed design, hardware equipments are built to test the essential variables of the universal inductive charging system. Because of low coupling, an IPT system is more easily influenced by the environment. Errors between theoretical and practical results are more obvious. As a result, the hardware experiments are important for the research of wireless charging. The main structure of the hardware system is shown in Fig. 6.1. The hardware system mainly includes 2 parts: the universal inductive charger, and the on-board AC-DC converter.

6.1. Hardware of Universal Inductive Charger

A 5 kW (maximum power) prototype has been built to test the applicability of the proposed system. The primary DC-AC inverter is a full-bridge inverter built by four MOSFETs, FDH44N50 (500V, 44A), as shown in Fig. 6.2.

A control model is built based on DSP (ADSP-21369) and FPGA (XC3S200-4TQG144C), as shown in Fig. 6.2. The DSP focuses on switch-signal calculations and FPGA does voltage and current measurement and generating gate-drive signals. A sensor
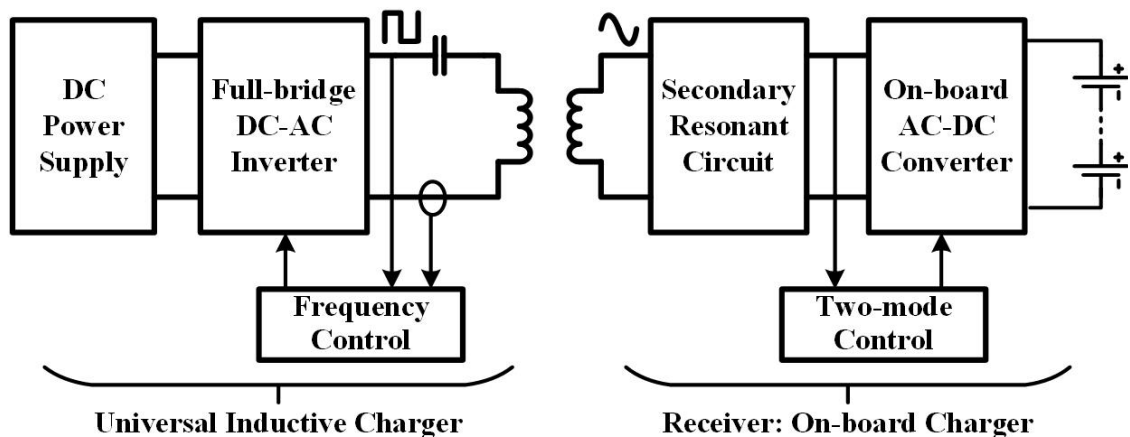
Fig. 6.1. Diagram of the main structure of the hardware system.
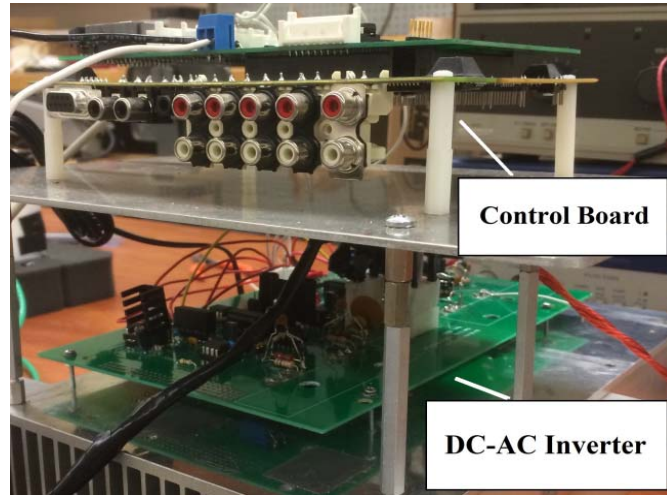
Fig. 6.2. Hardware of UIC: a full-bridge inverter and a control board.

board is applied to work in coordination with the FPGA for voltage and current measurements, as shown in Fig. 6.3. A frequency-tracking module made by analog devices and logic-circuits is used to detect f_1, based on the structure in Fig. 6.5. The diagram of structure and operation of the control model is shown in Fig. 6.4. The detailed coding of DSP is listed in APPENDIX C.3.2.

Fig. 6.3. Voltage & Current sensor board.
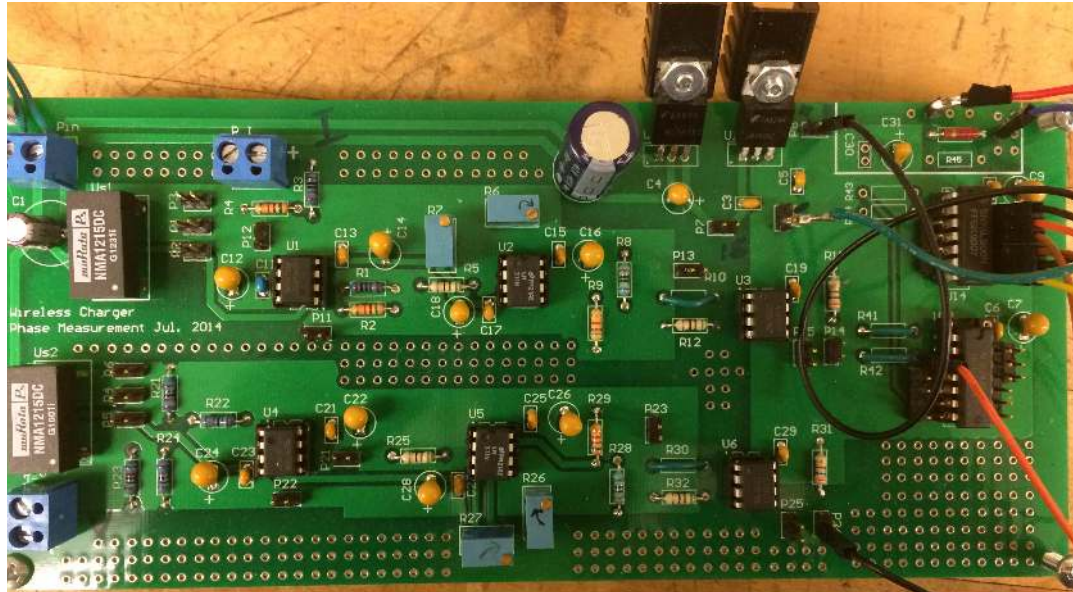
Fig. 6.5. Frequency-tracking module.
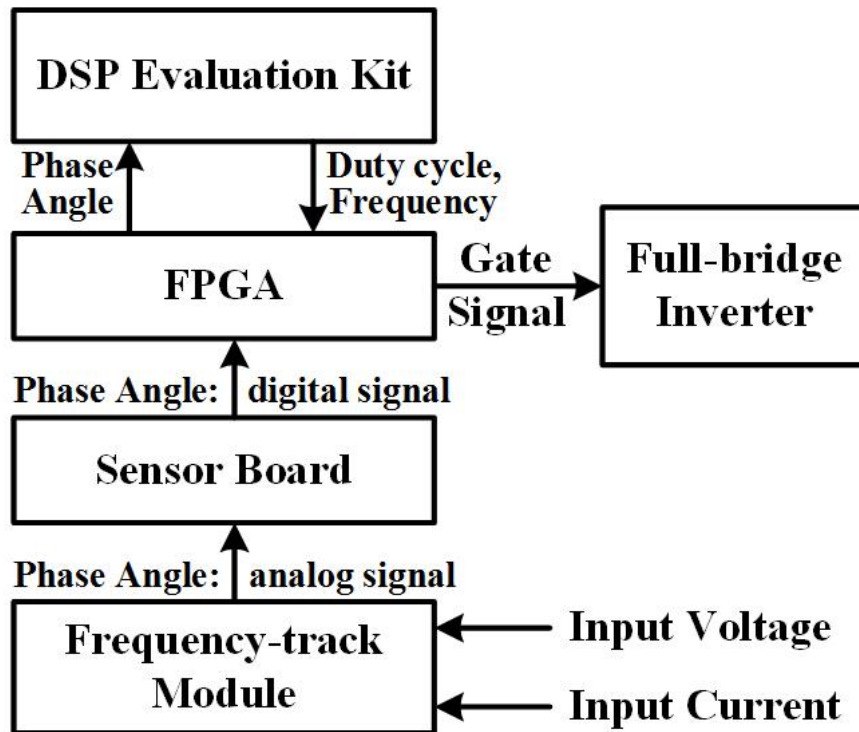
Fig. 6.4. Diagram of structure and operation of the control system.

The transmitting coil is shown in Fig. 6.6. The litz wire (14 AWG 5X33/36 Single Polyurethane-Nylon) is placed on a plastic structure. The detailed parameters of the transmitting coil are listed in Table 3.2.
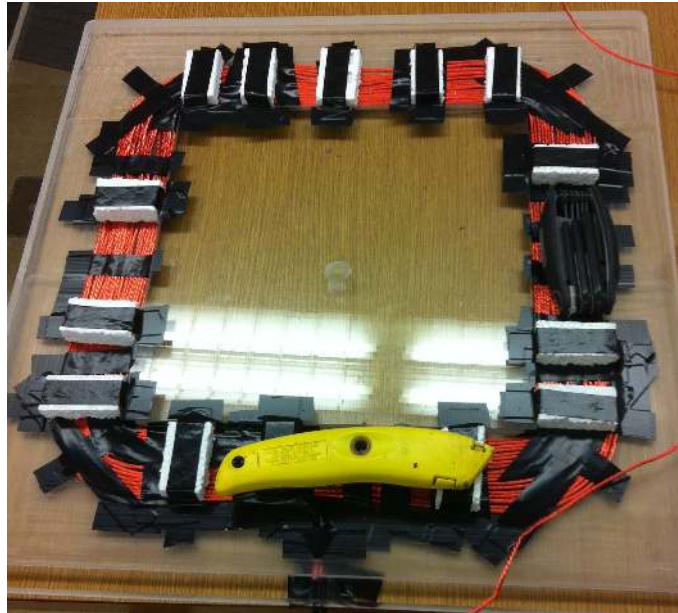
Fig. 6.6. Transmitting coil (pad) used in experiments.

6.2.   DC Power Supply

A power source (Agilent 6813B, AC Power Source/Analyzer, 300Vrms, 1750VA) made by *Agilent* is used to supply power to the primary DC-AC inverter, as shown in Fig. 6.7. In practical experiments, the output voltage is set to be a square waveform with a low frequency (0.01 Hz). A diode bridge with a DC capacitor is connected between the power supply and the input ports of the DC-AC inverter.

6.3.   Hardware of On-board Charger

The on-board AC-DC converter, also known as the on-board charger, consists of a receiving coil, a low-pass filter, and a DC-DC converter. The on-board charger receives

Fig. 6.7. DC power supply used in the hardware prototype.

AC power from the primary UIC and transfers it to nominal charging voltage and current to the batteries.

Similar to the schematics shown in Fig. 4.2, the prototypes of the two receiving pads are used to test design of on-board chargers with an S-connected *LC* circuit, as shown in Fig. 6.8. Two types of receiving coils, an SP (Coil 1) and a CP (Coil 2) are used for testing. The parameters of each receiving coil are listed in Table 3.2. Note that the structures of receiving coils and the transmitting coil are different from each other. The receiving coils have ferrite bars placing on the back of the pad for regulating the
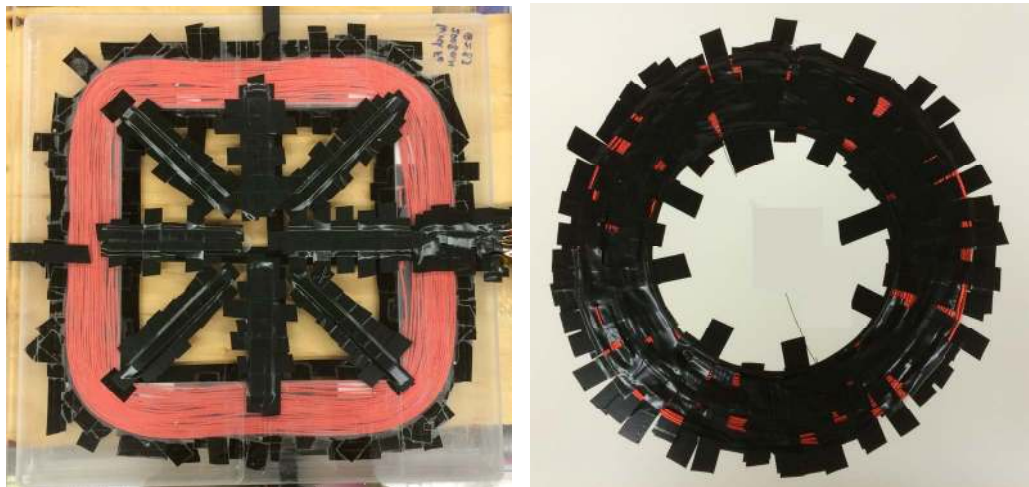
Fig. 6.8. Two types of receiving coils used in experiments with an S-connected secondary *LC* circuit.

magnetic flux and acquiring better coupling effect. Each ferrite bar is of 127mm×2mm×10mm - 3F3.
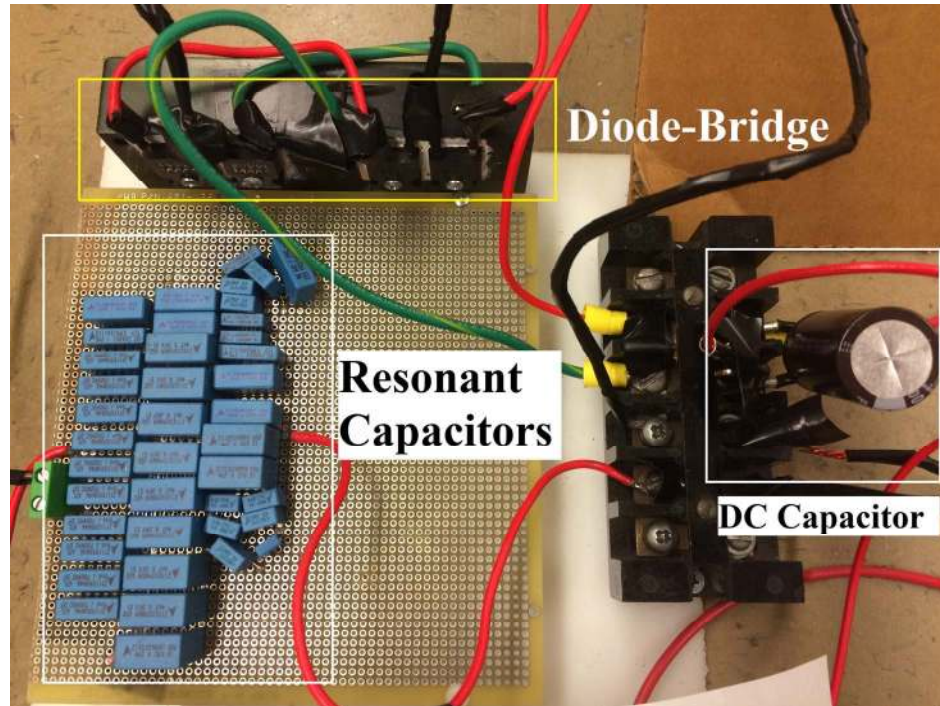
Fig. 6.9. The diode-bridge and the DC capacitor used in on-board chargers.

The diode bridge is formed by 4 ultra-fast diodes: STTH3006, 600V, 30A for an S-connected secondary *LC* circuit; or GP2D010A170B, 1700V, 33A for a P-connected secondary *LC* circuit. A 300μF, 1000V capacitor is used as the filter connected with the diode bridge. The secondary resonant capacitors, the diode bridge, and the filter are assembled in one board, as shown in Fig. 6.9.

When the on-board charger contains an S-connected *LC* circuit, a boost converter is used as the back-end DC-DC converter on the load. The structure of the DC-DC converter is shown in Fig. 6.10. The input voltage of the DC-DC converter is measured to test the two operation modes. The input current and output voltage are used for charging
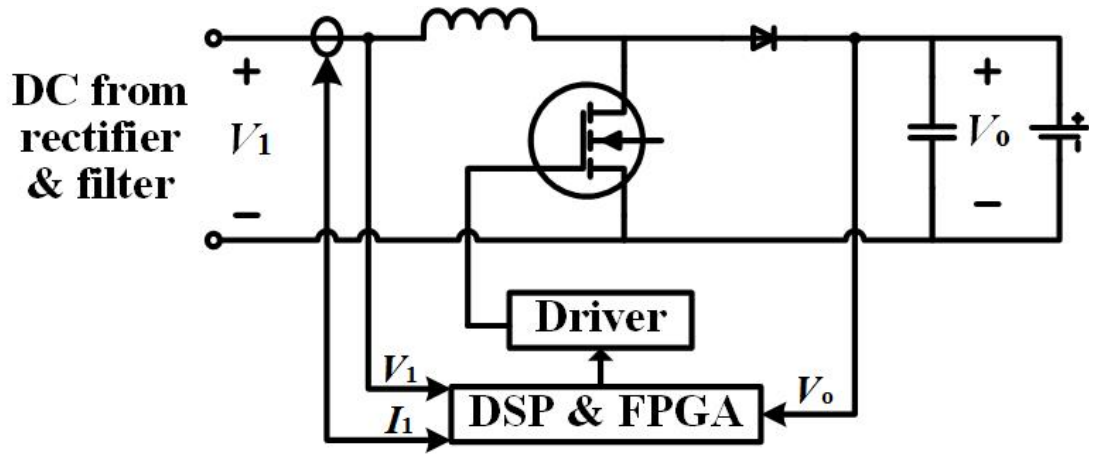
Fig. 6.10. Structure of the on-board DC-DC converter.

control. The input voltage ranges from 180V to 280V, and the input current can be higher

than 25A rms. The DC-DC converter used in experiments, including the boost converter

(inductor: 550 µH, capacitor 140 µF, switching frequency: 40 kHz). The control system

applies the same module (made by the DSP and FPGA boards) as that of the control

system applied in the UIC. The DSP focuses on switching signal calculations and FPGA

does voltage and current measurement and generating gate-drive signals. The hardware

DC-DC converter is shown in Fig. 6.11.
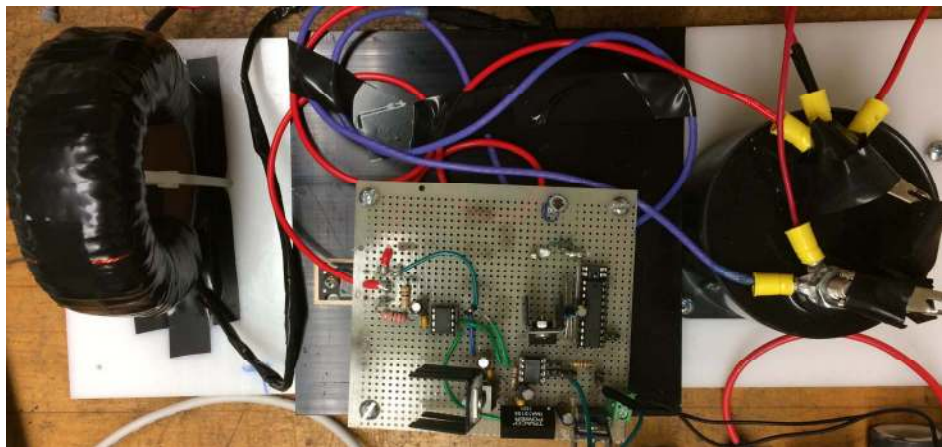
Fig. 6.11.   The on-board boost converter (inductor: 550 µH, capacitor 140 µF, switching frequency: 40 kHz).

CHAPTER 7: CONCLUSIONS, CONTRIBUTIONS, AND FUTURE WORK DIRECTIONS

7.1. Conclusions

Despite the fact that IPT technology has a bright future in EV charging, practical applications of inductive charging for EVs are seriously influenced by some common problems. First, varied magnetic coupling caused by various air gaps and horizontal misalignments changes the electrical characteristics of the IPT system. The variances of electrical characteristics lead to system instability. Moreover, the rapidly growing market of EVs requires a design standard for the universal charger that is capable of charging various EV models with different designs. To solve these practical problems of IPT systems, this dissertation proposes a universal inductive charging system, which is capable of providing stable charging V&I even with influences by varied magnetic coupling. The charging system is also capable of charging different EV models with various receiving pads and *LC* circuits. The proposed design scheme includes two parts: the universal inductive charger (UIC) on the primary side and two types of on-board chargers on the secondary side. The proposed design can be used as standards for IPT systems of EVs in the future.

The proposed UIC on the primary side is the basis for the universal inductive charging system. The UIC applies an S-connected *LC* circuit that always has a fixed-voltage-gain point of the resonant tank. The AC frequency at the fixed-gain point is the optimal frequency. The value of the fixed-gain point is not influenced by varied load resistances. A variable-frequency control strategy is used to track the fixed-gain point at

the beginning of every charging cycle. The fixed-gain point is tracked by increasing the AC frequency from the resonant frequency step by step and measuring the zero-crossing point (frequency) of the load-phase angle. The variable-frequency method guarantees ZVS operation of the primary DC-AC inverter within a wide range of magnetic coupling effects. For a more flexible control strategy, the AC frequency can be further adjusted to reduce the power factor of the system when the load becomes lighter during a charging cycle. Finally, the charging interfaces applied in IPT are optimized. A better pad design has a tighter coupling effect, meaning that the system has a higher efficiency and a higher power-transfer capability when the air gap and misalignment are the same. Considering practical size limitations on receiving pads, non-polarized square pads are proven to be the optimal charging interface.

Another part of the entire charging system, a specifically designed on-board charger, is proposed to coordinate with the previously proposed UIC for more accurate and adaptive frequency control and more stable charging V&I. The design scheme includes the same three aspects as the design of the UIC. The S-connected secondary topology is preferred because the voltage gain at the fixed-gain point is not influenced by varied magnetic coupling. To improve the accuracy of the tracked frequency, the on-board converter adds another operation mode besides the common charging control. In the added operation mode, the on-board charger sets the duty cycle as high as possible during the frequency-tracking process. A non-polarized pad is chosen as the receiving pad, according to the previously proposed transmitting pad in the UIC. A detailed design process of the receiving pad is proposed based on tighter magnetic coupling and specific charging profiles (nominal V&I) of the load. Simulations also demonstrate that a

122

receiving pad with a similar size to the transmitting pad is a good choice for tighter coupling and saving space.

To achieve the proposed universal inductive charging, a design scheme of the on-board charger with a P-connected *LC* circuit is analyzed. A small additional inductor is connected in series with the P-connected resonant tank for more accurate frequency tracking. Different from the traditional receivers with a P-connected *LC* circuit, the proposed design improves the efficiency by realizing ZVS of the primary DC-AC inverter. The advantages of the proposed on-board charger are demonstrated, including a much smaller range of optimal frequencies vs. magnetic coupling and lower voltage stress on resonant capacitors.

To validate the proposed design, simulations and hardware experiments are used. Simulations mainly include three main aspects: analyzing the DC characteristics of the resonant circuits, detailed circuit simulations of the system, and magnetic simulations on charging interfaces. A hardware system composed of two parts is built. The two parts include the UIC with variable-frequency control and two on-board chargers with different *LC* circuits, pad designs, and DC-DC converters. Based on the hardware system, the system efficiency, the optimal AC frequency, the voltage gain of resonant circuits, and the soft switching of the full-bridge DC-AC inverter are tested. The system (DC to DC) efficiency can be higher than 92%. With the dual-mode control of the on-board converter, the error between the practically tracked AC frequencies and the theoretical values is lower than 1 kHz. The voltage gain vs. the load resistance can be maintained in a range with errors lower than $\pm 8\%$. The measured voltage and current waveforms of the

switches used in the DC-AC inverter indicate that the input current always lags the input voltage. Thus, ZVS of the inverter is realized.

In summary, universal inductive charging is the main aim of this dissertation. Stable output, high efficiency, and robust control are the most important advantages of the proposed design. The designs of a primary charger and on-board chargers are analyzed. The design details, including the design of the resonant circuit, the control strategies, and the design of the interfaces, are optimized. Simulations and hardware experiments are employed to validate the proposed system.

7.2. Contributions

The contributions of the dissertation are summarized as follows:

1) A UIC is proposed to provide a stable and controllable charging voltage to loads with different characteristics via varied magnetic coupling between transmitting and receiving pads. The idea of the universal charging has rarely been mentioned by previous research. The design scheme of the UIC is comprehensively analyzed by this dissertation, in the areas of *LC* resonant circuits, control methods, and charging pads. Circuit and magnetic simulations along with hardware experiments demonstrate the high efficiency and universality of the proposed UIC. The proposed design scheme can be treated as a standard for designing EV inductive chargers in the future.

2) A design scheme for on-board chargers is also proposed. According to the definition of universal charging, on-board chargers based on an S-connected and a P-connected

LC circuits are both analyzed and optimized. The proposed design scheme works as a comprehensive reference for future development of on-board chargers.

3) A hardware system is built, including two parts: the UIC with an adaptive frequency-control strategy, and two on-board chargers with different receiving pads and DC-DC converters. The voltage gain and system efficiency are tested, in different load conditions and with various coupling effects. Detailed waveforms are measured to demonstrate ZVS of the UIC. More IPT tests can be conducted based on the current prototype, with only minor adjustments.

4) An easy and low-cost variable-frequency method is the main control strategy in the proposed UIC. Most of current research applies PWM to control the output V&I. Wireless communication is the basis for controlling most of the previously proposed systems. However, the proposed variable-frequency control is a more flexible method for controlling the output and optimizing efficiency at the same time. Wireless communication between the primary charger and the receiving load is unnecessary. The variable-frequency control can also be used in combination with the traditional PWM.

5) An effective method of V&I sensing is proposed to provide information for variable-frequency control. In common IPT systems, transient measurements of high-frequency (80 kHz ~ 90 kHz) voltage and current are difficult. The proposed method effectively captures the phase difference between the input voltage and current of the primary DC-AC inverter in a high-frequency application. The proposed load-phase-detecting method is also capable of detecting the *LC* connection and the charging condition of the load without wireless communications.

6) A novel dual-mode modulation of the on-board charger is analyzed for more accurate frequency control and more stable output voltage. Coordination between the primary charger and the load is robust, without the necessity of wireless communication. The primary charger or the load only needs to measure the V&I on its own side. No additional device is added to achieve two-side coordination. The control of the system can be used as another loop in addition to transmitting the notifications of the charging states such as pause, error, and stop. These notifications do not need transient system control or response in microseconds.

7) Designs of resonant circuits and charging pads are analyzed based on practical conditions. Non-polarized charging pads are preferred because of the size limitation by EVs' chassis. Moreover, the battery pack of Nissan Leaf is used as a practical example for designing on-board chargers. As a result, the proposed "universal inductive charging" is reliable and applicable.

7.3. Publications

Two journal paper and four conference papers are planned to be published from the proposed dissertation research:

1) **Liu, Nan**; Habetler, T.G., "Design of a Universal Inductive Charger for Multiple Electric Vehicle Models,"*Power Electronics, IEEE Transactions on*, vol.30, no.11, pp.6378,6390, Nov. 2015.

2) **Liu, Nan**; Habetler, T.G., "Design of a Series-LC-Compensated On-board Charger for Universal Inductive Charging of Electric Vehicles," will be submitted on *IEEE Transactions*.

3) **_Liu, Nan_**; Habetler, T.G., "Design of On-board Charger for Universal Inductive Charging", *Energy Conversion Congress and Exposition (ECCE 2015),* IEEE, 2015, accepted.

4) **_Liu, Nan_**; Habetler, T.G., "Design of a universal inductive charger for electric vehicles." *Transportation Electrification Conference and Expo (ITEC), 2014 IEEE.* IEEE, 2014.

5) **_Liu, Nan_**; Habetler, T.G., "A study of designing a universal inductive charger for Electric Vehicles," *Industrial Electronics Society, IECON 2013-39th Annual Conference of the IEEE*, vol., no., pp.4528,4533, 10-13 Nov. 2013.

6) **_Liu, Nan_**; Habetler, T.G., "A Parallel-LC-Compensated On-Board Charger for Universal Inductive Charging in Electric Vehicles," will be submitted on *Energy Conversion Congress and Exposition (ECCE 2016)*.

Another paper about inductive charging was published during the internship in MERL in summer 2013:

1) **_Liu, Nan_**; and Wang, B., "An LLC-based planar wireless power transfer system for multiple devices." *Applied Power Electronics Conference and Exposition (APEC), 2014 Twenty-Ninth Annual IEEE*, 2014.

7.4. Future Work Directions

Based on the analysis and results presented in this dissertation, the following improvements are recommended for future research on the universal inductive charging systems.

7.4.1. Replace Load Resistance with EV Batteries

In the experiments, a resistor and capacitor are connected in parallel to represent the power consumption and load characteristics of EV batteries. However, the V&I characteristics of EV batteries are non-linear in practical applications. Nowadays, battery management systems (BMS) are installed on EVs to control the battery-charging V&I and protect the battery. Therefore, in practical applications, the load characteristics looking from the output of the secondary LC is different from a common DC-DC converter connected by a parallel RC combination at the output. Although various resistors are used in hardware experiments to represent varied load conditions, using real batteries in hardware experiments is important to validate system applicability.

7.4.2. Optimization of Resonant Circuits

This dissertation demonstrates the stable output voltage and high efficiency of the proposed system, with various magnetic coupling and load resistance. While the proposed design aims at choosing the optimal LC topologies, the optimization of inductance and capacitance are not analyzed. In fact, each coil in the charging pads has parasitic resistance, which consumes a considerable portion of the overall power loss. The parasitic resistance of a coil is related to the overall length of the wire, meaning that the parasitic resistance is related to the coils' turns, self-inductance, and quality factor. From this view, the inductances of the charging pads can be optimized for higher efficiency when the frequency range and the load range are determined.

First, the ratio of L_2 to L_1 is fixed based on the requirements of the output voltage. With the already-known ratio, the values of L_1 and L_2 can be optimized, based on the equivalent topology of LC circuits with parasitic resistances. The basic calculations can be done by the same structure used in calculating DC characteristics.

7.4.3. Roadway Electrification

A lot of relevant research on IPT technology has proposed applications of roadway electrification (on-line charging) where EVs are charged while driving on road. The main challenge of roadway electrification is the fast variation of the coupling effect vs. horizontal movement in a wide range. Consequently, the roadway charging system needs a stable output vs. the varied magnetic coupling. More importantly, system modulation must be adaptive, accurate and ultra-fast. The variable-frequency control proposed in this dissertation can be applied in roadway electrification. Moreover, the proposed system with SP-connected *LC* circuits has a relatively constant optimal frequency vs. magnetic coupling, giving it an advantage for use in roadway electrification.

APPENDIX A: CIRCUIT SIMULATIONS AND MODELING OF UNIVERSAL INDUCTIVE CHARGING SYSTEM

A.1   DC Characteristics by Theoretical Modeling

By previous analysis, the DC characteristics (voltage gain and load-phase angle) are the most important parameters for evaluating an IPT system. For the proposed UIC, the voltage gain and overall load-phase angle of the resonant circuits are analyzed in a certain range of the AC frequencies (the switching frequency of the primary DC-AC inverter), with various mutual inductances. The DC characteristics are also analyzed with a fixed primary *LC* circuit but different secondary *LC* topologies for testing the universal applications with various models of EVs. The topologies used in the circuit modeling are referred to Fig. 2.2. The Matlab codes are listed below:

"

```matlab
clear all;

% This program is used to test the DC characteristics of LLC resonant
% Converter, which may be applied in wireless power transfer.


L1 = 199.5e-6;  % Self-Inductance 1
L2 = 200.8e-6;

% Ls = 20e-6;   %Added Series-inductance
Ls = 0e-6;    %Added Series-inductance

M= 44e-6;      %Mutual Inductance when air gap=11cm.

% Resonant frequency
f0=80*1000;
omega = 2*pi*f0;

% Resonant capacitance
C1=1/(omega*omega)/(L1+Ls);    % Primary Resonant Cap when f0=50kHz.
C2=1/(omega*omega)/(L2);     % Secondary Resonant Caps when f0=50kHz.
```

```matlab
% Load Resistance
%R = [2; 3.5; 5; 7; 9.4; 15; 20; 25; 50; 70]*2;
R = [10; 15; 20; 25; 30; 35; 40; 50; 60; 80; 120];

V_gain = zeros(601,11);   % Voltage gain between output and input.
Z = zeros(601,11);        % Overall impedance at the certain condition
Phase =  zeros(601,11);   % Load-phase angle
V_charge = zeros(601,11);

Q=zeros(11,1);% Quality Factor

f=60e3;        % Initial value in the range of frequency by analysis

V_in = 1;

for q=1:11  % Various values of load resistance

    for i =1:601    % Various values of frequency
        f=60e3;
        f = f+(i-1)*100;
        omega = 2*pi*f;

        % Impedance following mutual inductance M
        Z_load = 1j*omega*(L2-M)+1/(1j*omega*C2)+R(q,1);   % SERIES-
connected LC

%          Z_load = 1j*omega*(L2-M) +
1/(1j*omega*C2)*R(q,1)/(R(q,1)+1/(1j*omega*C2)); %Parallel-connected LC
load

        % Impedance of the branch of mutual inductance M
        Z_M = 1j*omega*M*Z_load/(1j*omega*M+Z_load);

        % Overall impedance
        Z_total = 1j*omega*Ls + 1j*omega*(L1-M) + 1/(1j*omega*C1) +Z_M;
        Z(i,q)=Z_total;
        Phase(i,q) = atan(imag(Z_total)/real(Z_total))/pi*180 ;

        % Input voltage
        V_in = 1;

        % Voltage on M branch
        V_M = V_in*Z_M/Z_total;

        % Output voltage
        V_out = V_M*R(q,1)/Z_load;

        V_charge(i,q)=abs(V_in*(1j*omega*(L1-M)+Z_M)/Z_total/V_in);
        V_gain(i,q) = abs(V_out/V_in);

    end
```

```
%    Q=imag(Z_total)/real(Z_total);
end

subplot(2,1,1)
f_axis = 60:0.1:120;
% line_axis=[113.9; 113.1; 112.1; 112; 109.7; 105.1; 100];
% line_value = [1.007; 1.001;  1.003; 1.00; 1.002; 1.003; 1.002;];
plot(f_axis(:),V_gain(:,1),f_axis(:),V_gain(:,2),f_axis(:),V_gain(:,3),
f_axis(:),V_gain(:,4),f_axis(:),V_gain(:,5),f_axis(:),V_gain(:,6),f_axi
s(:),V_gain(:,7),f_axis(:),V_gain(:,8),f_axis(:),V_gain(:,9),f_axis(:),
V_gain(:,10),f_axis(:),V_gain(:,11));
xlabel('Switching Frequency');
ylabel('Voltage Gain');
xlim([67 92]);
% ylim([0 3]);
ylim([0 7]);
grid on

% % subplot(2,1,1)
% f_axis = 70:0.1:130;
% line_axis=[113.9; 113.1; 112.1; 112; 109.7; 105.1; 100];
% line_value = [1.007; 1.001;  1.003; 1.00; 1.002; 1.003; 1.002;];
%
plot(f_axis(:),V_charge(:,1),f_axis(:),V_charge(:,2),f_axis(:),V_charge
(:,3),f_axis(:),V_charge(:,4),f_axis(:),V_charge(:,5),f_axis(:),V_charg
e(:,6),f_axis(:),V_charge(:,7),f_axis(:),V_charge(:,8),f_axis(:),V_char
ge(:,9),f_axis(:),V_charge(:,10));
% xlabel('Switching Frequency');
% ylabel('Voltage Gain');
% xlim([85 115]);
% % ylim([0 5]);
% grid on

subplot(2,1,2)
f_axis = 60:0.1:120;
plot(f_axis(:),Phase(:,1),f_axis(:),Phase(:,2),f_axis(:),Phase(:,3),f_a
xis(:),Phase(:,4),f_axis(:),Phase(:,5),f_axis(:),Phase(:,6),f_axis(:),P
hase(:,7),f_axis(:),Phase(:,8),f_axis(:),Phase(:,9),f_axis(:),Phase(:,1
0),f_axis(:),Phase(:,11));
xlabel('Switching Frequency');
ylabel('Phase');
xlim([67 92]);
ylim([-90 90]);
grid on
"
```

The DC characteristics shown in Fig. 3.2 are calculated by the codes above. In the

proposed design, the S-connected *LC* circuit is chosen as the optimal topology of the

primary resonant circuit. On the other hand, the sentences of the "Z_M" and "Z_load" are

edited if the secondary *LC* circuit is changed, but the coding sentence of "Z_total" (the primary *LC* circuit) is kept same. The coding sentence of "V_out" should also be revised when the secondary *LC* circuit is changed. To analyze the influence of the mutual inductance *M* on the output performance, the variable "M" should be revised. An array of "M" can be used to test the electrical characteristics vs. mutual inductances. To test the DC characteristics of an *LLC* structure, the variable "Ls" should be edited.

A.2 Simulink Models of an IPT System

A.2.1 Typical Model of an IPT System

As shown in Fig. A.1, Simulink models are used to show the transient
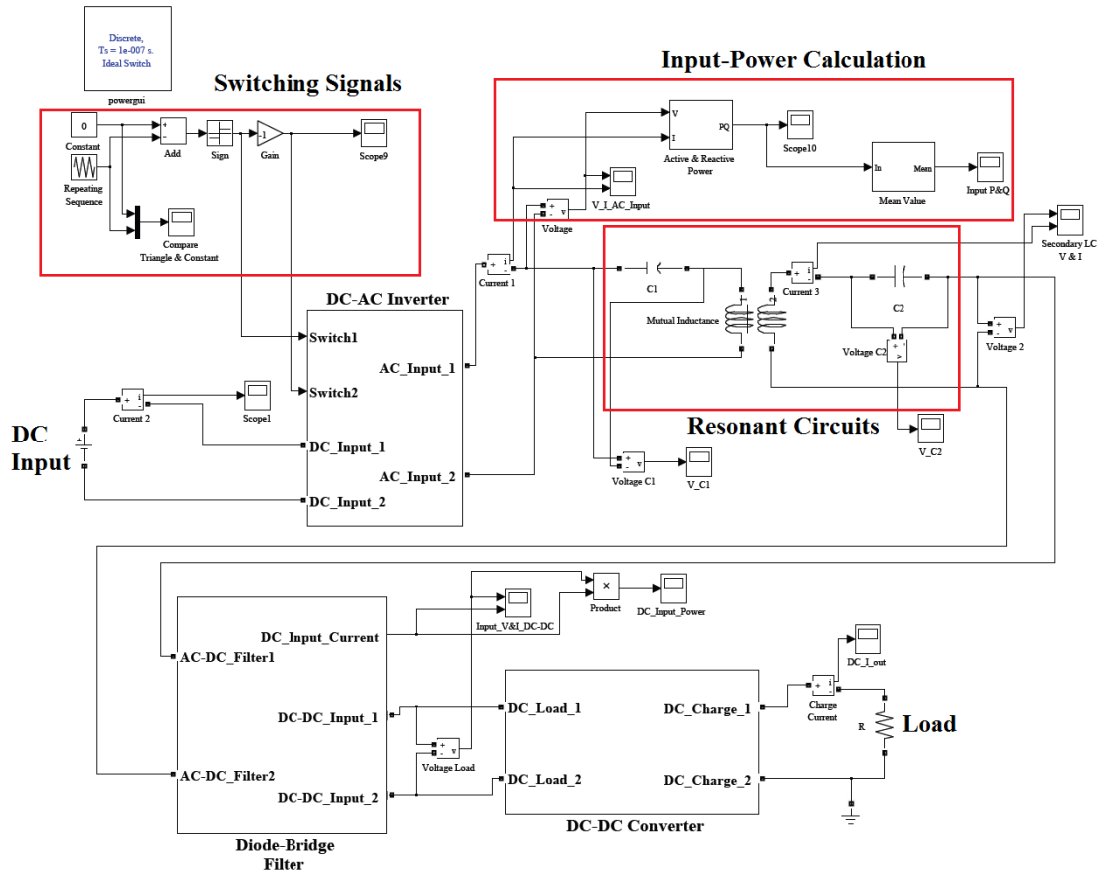
Fig. A.1. Simulink model of a typical IPT system.

characteristics of the IPT system. A typical model of the IPT system is built by the components of the Library "SimPowerSystems". The model consists of 6 main parts: the primary DC-AC inverter, the signal generator for the primary DC-AC inverter, the *LC* resonant tank, the on-board AC-DC filter, the on-board DC-DC converter, and the power-calculation modules. A constant-voltage DC input is used to provide DC power to the primary DC-AC inverter. A resistance module is used to represent the load. In fact, a capacitor if parallel connected to the output ports of the on-board DC-DC converter; the parallel-connected resistance and capacitance are used to simulate the load condition of batteries.

The under-mask model of the subsystem of the DC-AC inverter is shown in Fig. A.3. The components "Ideal Switch" and "Diode" are used to form the model of MOSFET. The parameters including the internal resistance R_{on}, the forward voltage V_f,
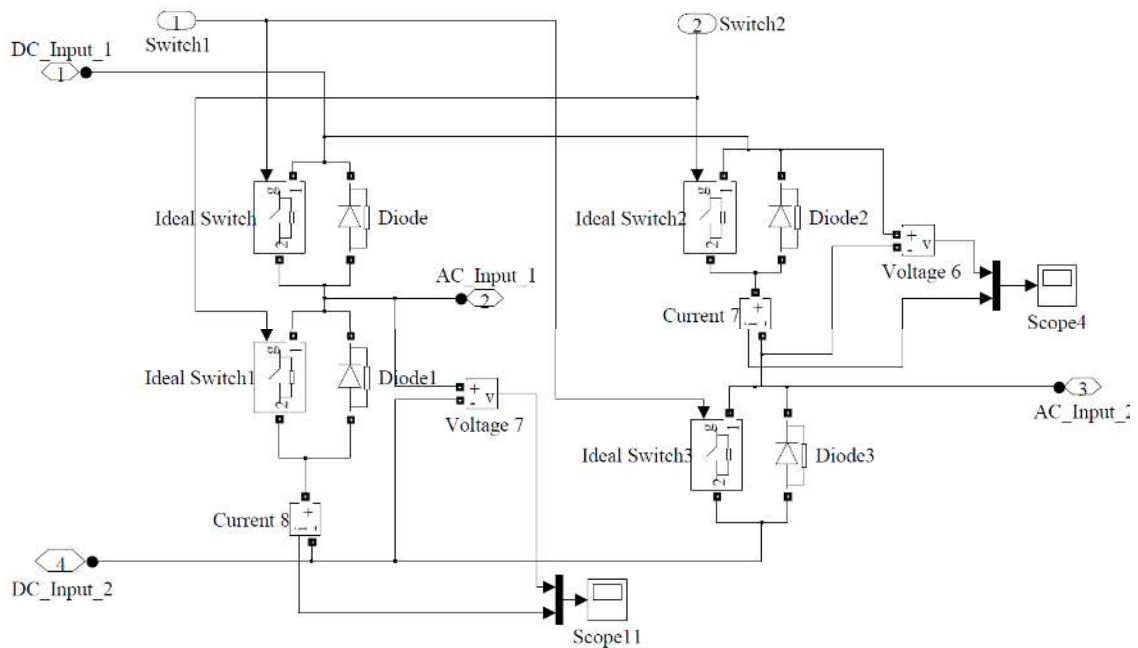
Fig. A.2. Subsystem of the primary DC-AC inverter in the Simulink model.
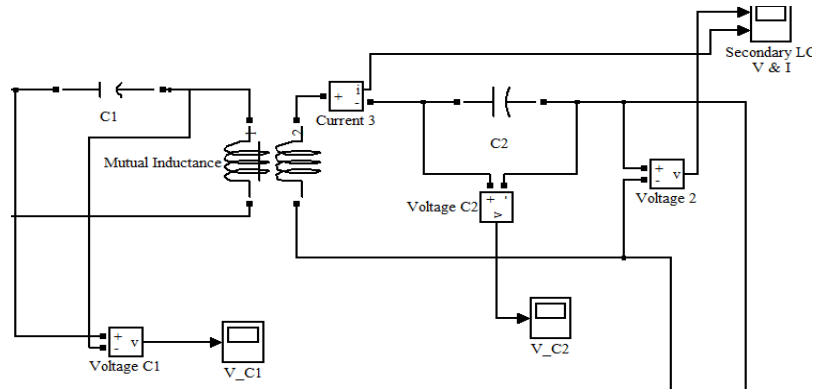
Fig. A.3. Resonant Circuits in the Simulink model.

the snubber and the capacitances, can be adjusted in the user interface of "Block Parameters". Since an IPT usually has a relatively high input DC voltage and the resonant circuit directly connecting to the output of the DC-AC inverter, the effects of adjusting forward voltage of the diodes and parasitic capacitance in the simulation is not obvious. The ZVS operation of DC-AC converter and be demonstrated by measuring the Drain-Source voltage of the switch and the overall current flowing through both a switch and its parallel-connected diode.

The model of resonant circuits is built by a block of "Mutual inductance" and 2 common capacitances, as shown in Fig. A.3. The self-inductances and parasitic resistances of the transmitting and receiving coils can be adjusted. The mutual inductance M and equivalent mutual resistance R_m can also be adjusted as well.

The subsystem of the diode bridge and the LC filter under mask is shown in Fig. A.4. The diode bridge employs the same component used in DC-AC inverter.

The subsystem of the on-board DC-DC converter under mask is shown in Fig. A.5. A dual-loop structure is used to control the switch signal. The control system (dual-
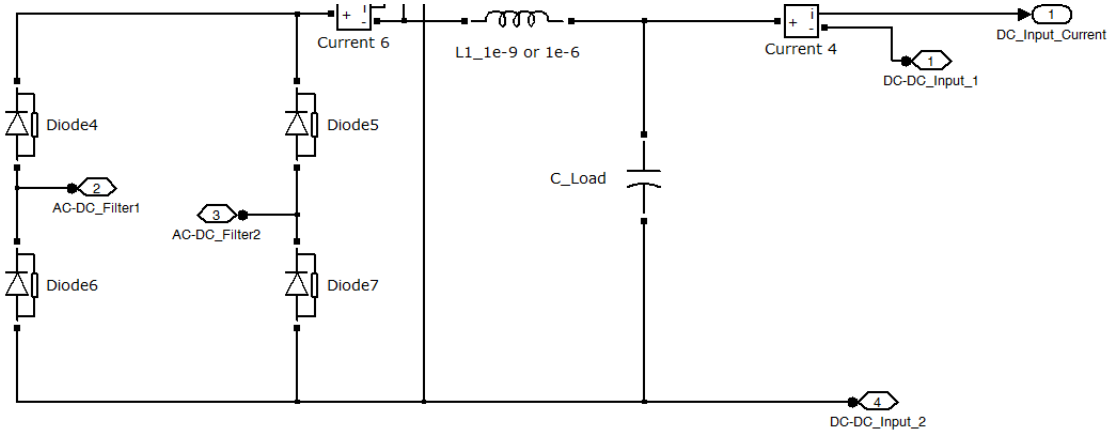
Fig. A.4. On-board diode bridge and LC filter in the Simulink model.

loop control) acquires feedbacks of the input current and output voltage. The MOSFET

used in the subsystem is the component "Mosfet" from Library "SimPowerSystems".

The gate-drive signals of the primary DC-AC inverter is generated by a
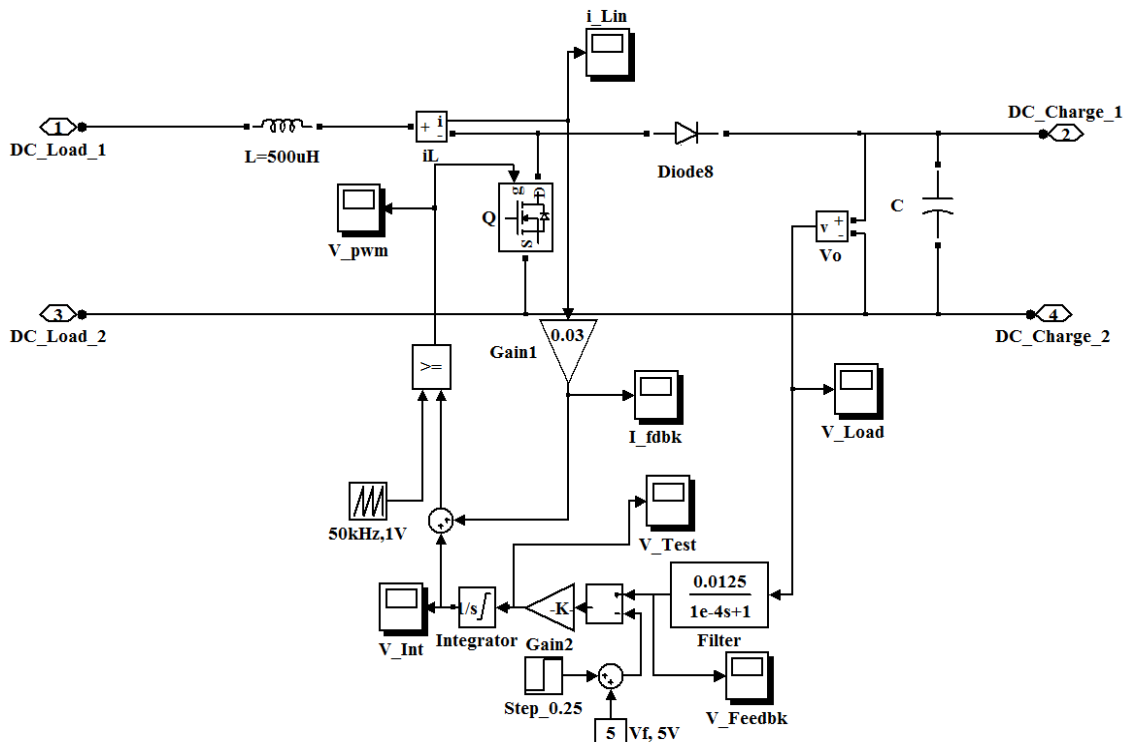
Fig. A.5. On-board DC-DC converter in the Simulink model.

136

comparator with 2 input ports: a constant source and a triangle-waveform generator (Component "Repeating Sequence"). As the frequency control is the mainly focused control strategy applied in the proposed design, the constant input is assigned to be 0 to achieve duty cycle = 0.5.

The block "Active & Reactive Power" is used to measure the transient power level of the system.

The simulated outputs can be acquired by running the Simulink model. For example, when the primary DC input is 200 V, the *LC* resonant circuits are the same in Table 3.1, the AC frequency is 87.3 kHz, and the final load resistance is 100 Ω, the simulated output current is shown in Fig. A.6. The output current is stabilized at the nominal value 4 A (nominal voltage 400 V). The validation of the ZVS operation of primary DC-AC inverter is shown in Fig. A.7. Obviously, the current I_D (green waveform)
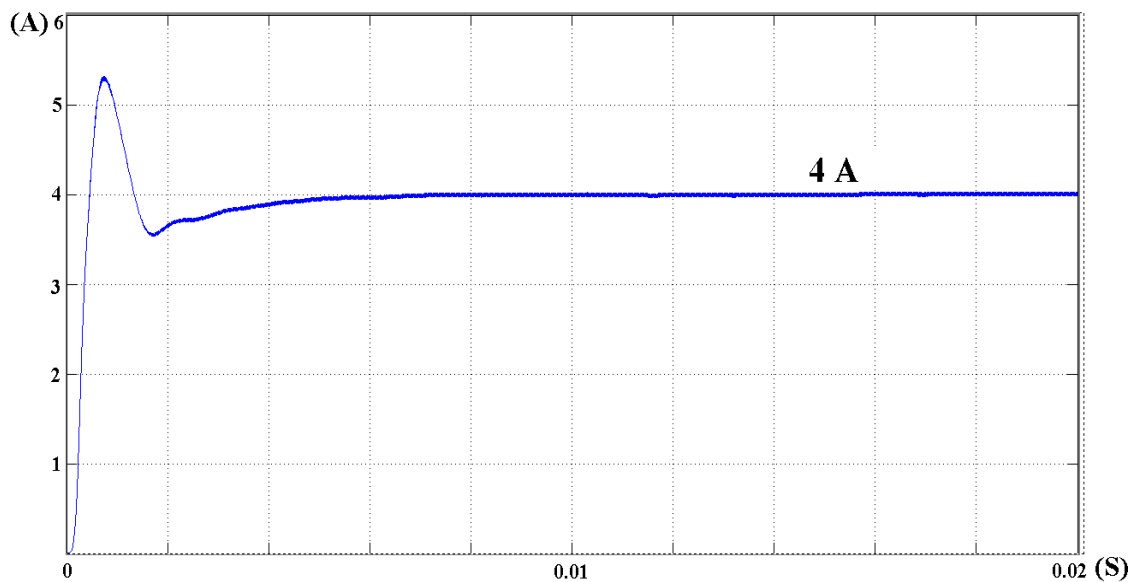
Fig. A.6. Charging current simulated by the Simulink model.

137
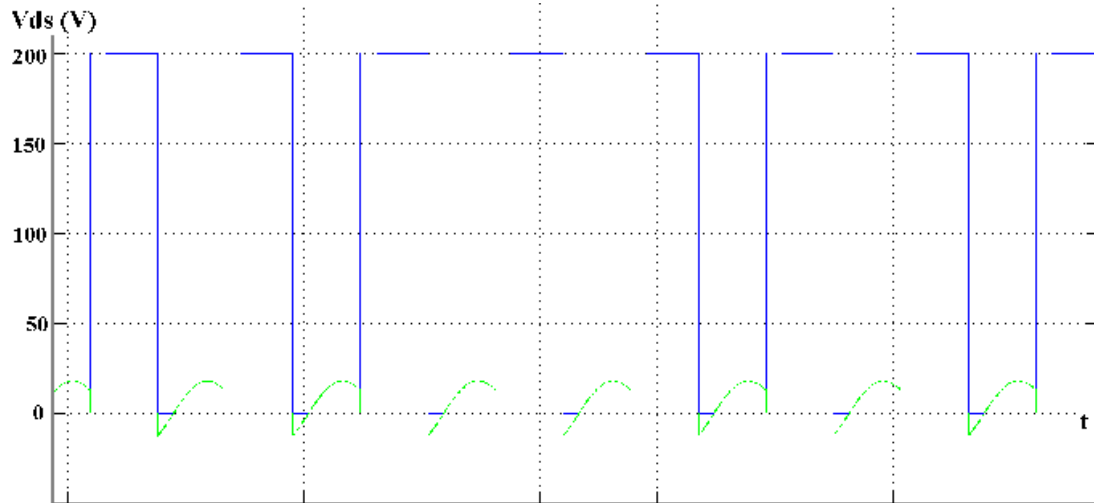
Fig. A.7. Voltage V_{DS} and current I_D of Q_1 in the Simulink model.

changes from zero to a negative value when the switch is kept off, meaning that current flows through the body diode of the switch (voltage V_{DS} changes to 0). When I_D increases from negative to zero, the switch is turned on and current will flow through the switch. Thus, the switch is turned on with zero V_{DS}.

A.2.2 Detection of Load-Phase Angle

The overall load-phase angle (phase shift between input AC voltage and current) is detected by a logic circuit and an RC average circuit. The logic circuit is used to capture the phase shift between the AC voltage and AC current. The captured signal is square waveform whose width is equal to the phase shit. Then the RC circuit transfers the captured signal to a DC voltage whose value is proportional to the width of the captured signal. A Simulink model is used to test the applicability of the circuit, as shown in Fig. A.8. A DC voltage and two complementary switches are used to generate square waveform. A resistance and a capacitance from the basic model library are used for the RC average circuit.

138
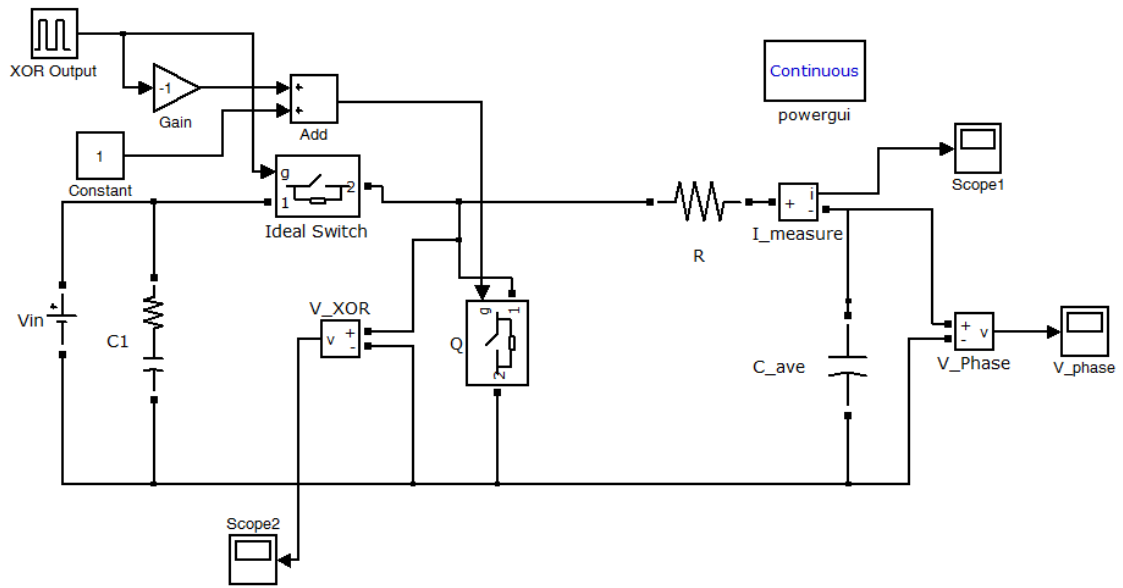
Fig. A.8. Detection of load-phase angle by the Simulink model.

APPENDIX B: MAGNETIC SIMULATION OF CHARGING INTERFACES

This Appendix introduces magnetic simulations used in the proposed system design. Magnetic simulations are important for design of IPT systems. The self-inductances of charging pads and the mutual inductance between two charging pads directly determine the power-transfer capability and the efficiency of the system. The simulation results can be taken into the circuit analysis for further analysis. Moreover, magnetic simulations of various combinations of the charging pads are done, to make comparisons among various pad designs.

B.1   Model of Non-polarized Charging Interfaces

As shown in Fig. B.1(a), non-polarized charging pads can be built in the software Ansoft-Maxwell.

First, 3-D schematics of the charging pads are drawn. The dimensions of the 3-D models must be set up carefully. Then the material of each part can be selected, such as copper and ferrite. An interface of "Coil Terminal" must be added in each coil to conduct currents in the simulation. Note that 3-D models are preferred, instead of 2-D models. Since the simulations are done with varied pads' misalignments; horizontal misalignments of the pads are better simulated by 3-D models.

After building the 3-D models, the self-inductances of coils and mutual inductances between two coils can be simulated, by the solution type "Magnetostatic Solution". The results are from the menu: Maxwell 3D > Results > Solution Data > Tab "Matrix".
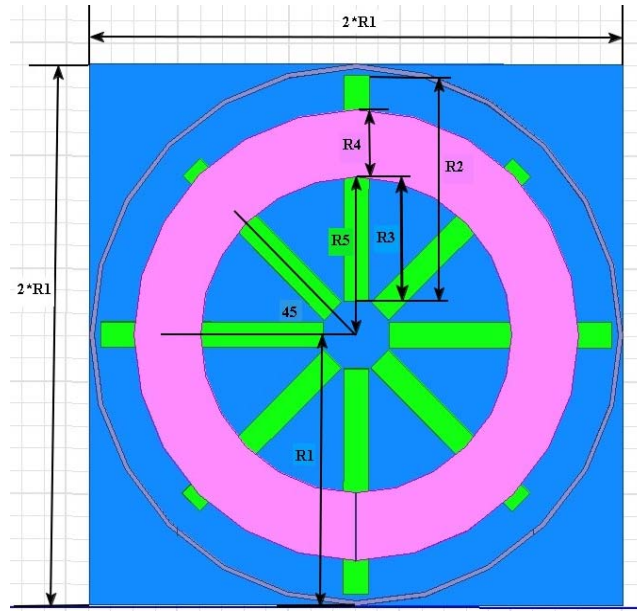
(a)
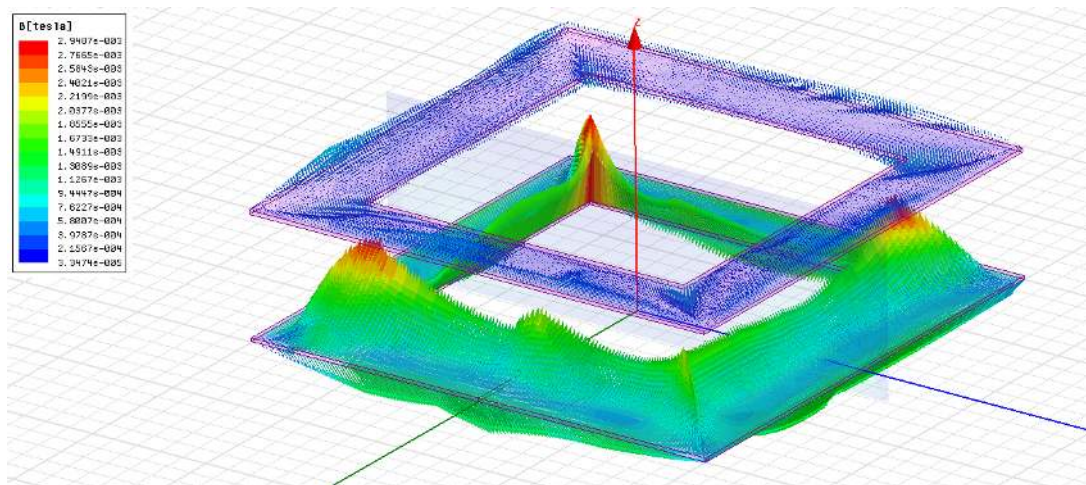
(b)

Fig. B.1. (a) Top view of a non-polarized charging pad (CP), where the red parts are coils; the green parts are ferrite bars; the blue parts are back aluminum plate; and (b) flux arrows of a pair of SPs facing to each other.

The flux distributions or flux arrows can be drawn, in "Transient Solution", as shown in Fig. B.1(b). The simulated flux in each selected time point can be drawn. Accordingly, researchers are able to observe the transient variations of the magnetic flux. The self-inductances and mutual inductances can be calculated by the solution type

141

"Transient Solution". Users need to combine windings to according terminals. The simulated inductances can be checked in Results > L(winding NO., winding NO.).

For a more clear view of the flux in a cross-section direction, users can put a surface model made by air in the relevant position and observe the flux on the surface, as shown in Fig. B.2.

B.2   Model of Polarized Charging Interfaces

As shown in Fig. B.3, polarized charging pads can also be built in the software Ansoft-Maxwell. The two coils in a polarized pad are series connected. The currents flowing through the two coils are in the opposite directions. The magnetic flux is shown in Fig. B.3(b), where the bottom pad is the transmitting pad. From the figure, it is clear
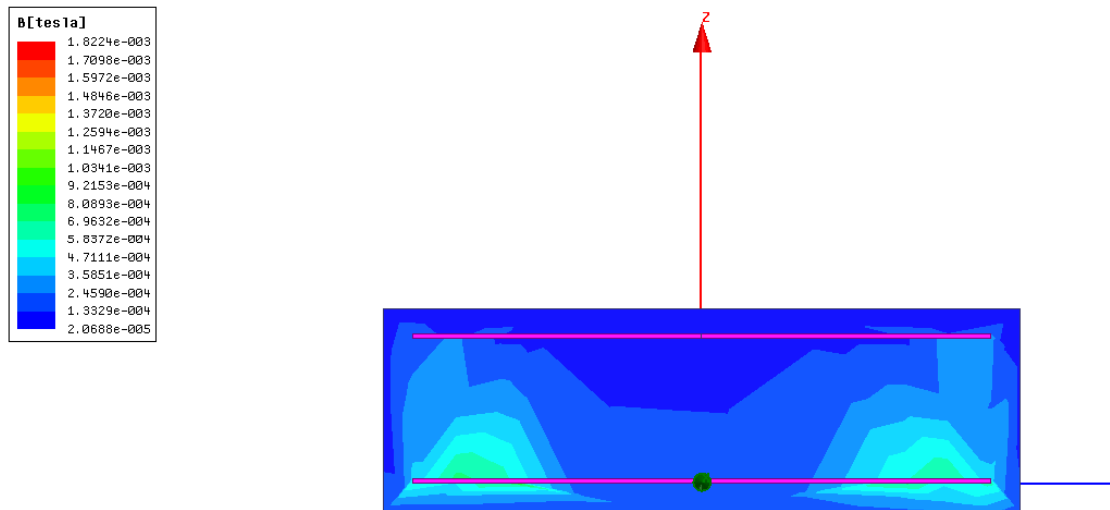
Fig. B.2. Flux distribution in a cross-section view, by Maxwell.

that the ferrite bars help force the flux to flow in the horizontal direction.
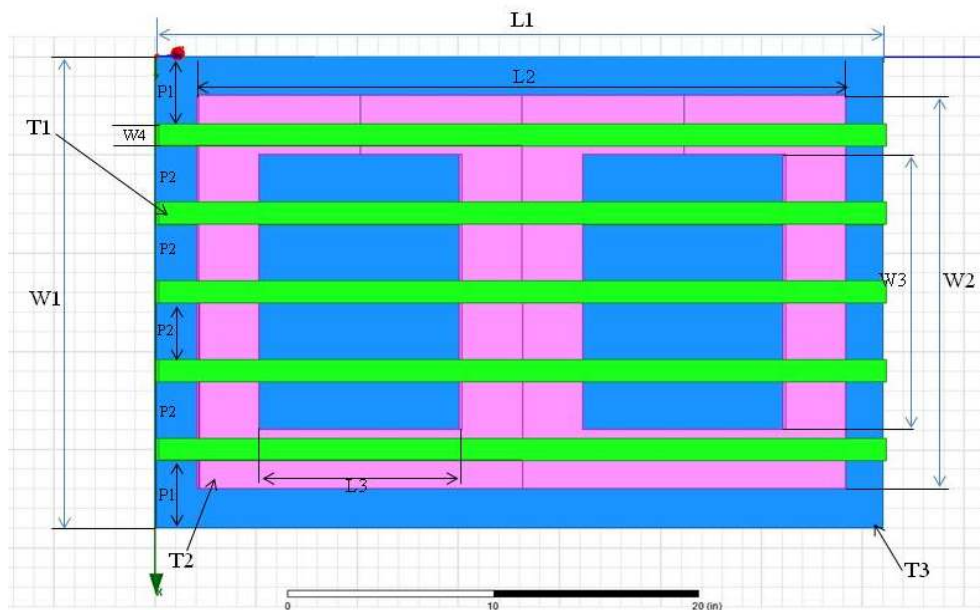
(a)
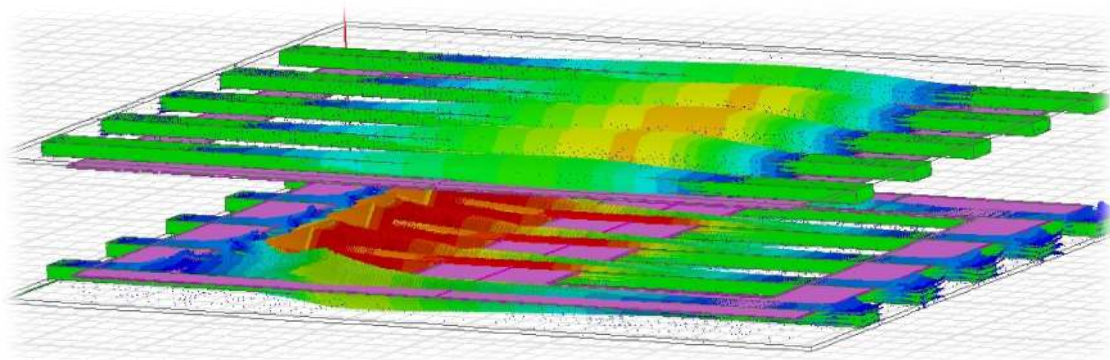
(b)

Fig. B.3. (a) One polarized charging pad (BPP) used in simulations, and (b) flux arrows of a pair of transmitting and receiving pads (BPPs) facing to each other.

APPENDIX C: LABORATORY IMPLEMENTATION OF INDUCTIVE CHARGER AND ON-BOARD CHARGER

This Appendix introduces the hardware system used to validate the proposed design. The hardware system includes the primary DC-AC inverter, various resonant circuits, the on-board chargers, and the control systems used for the system control. The schematics, PCB designs, and bills of materials are provided.

C.1   Schematic and PCB of the Primary DC-AC Inverter

The prototype of the DC-AC inverter consists of four parts: a buffer of switch-driving signals, power supplies for all ICs, four sets of gate drivers, and four MOSFETs to build the full-bridge inverter. The structure is shown in Fig. C.1.

The overall Schematic of the DC-AC inverter is shown in Fig. C.2.
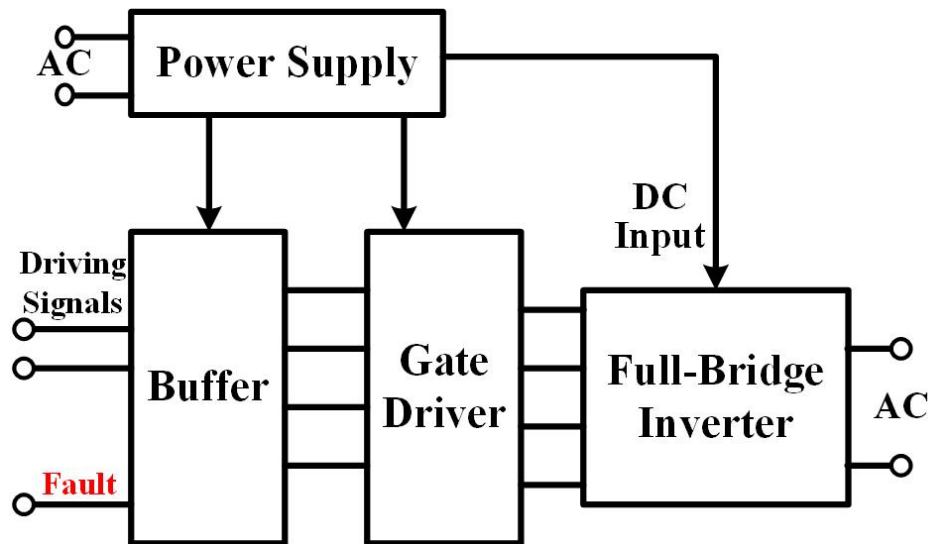
Fig. C.1. Structure of the primary DC-AC inverter.
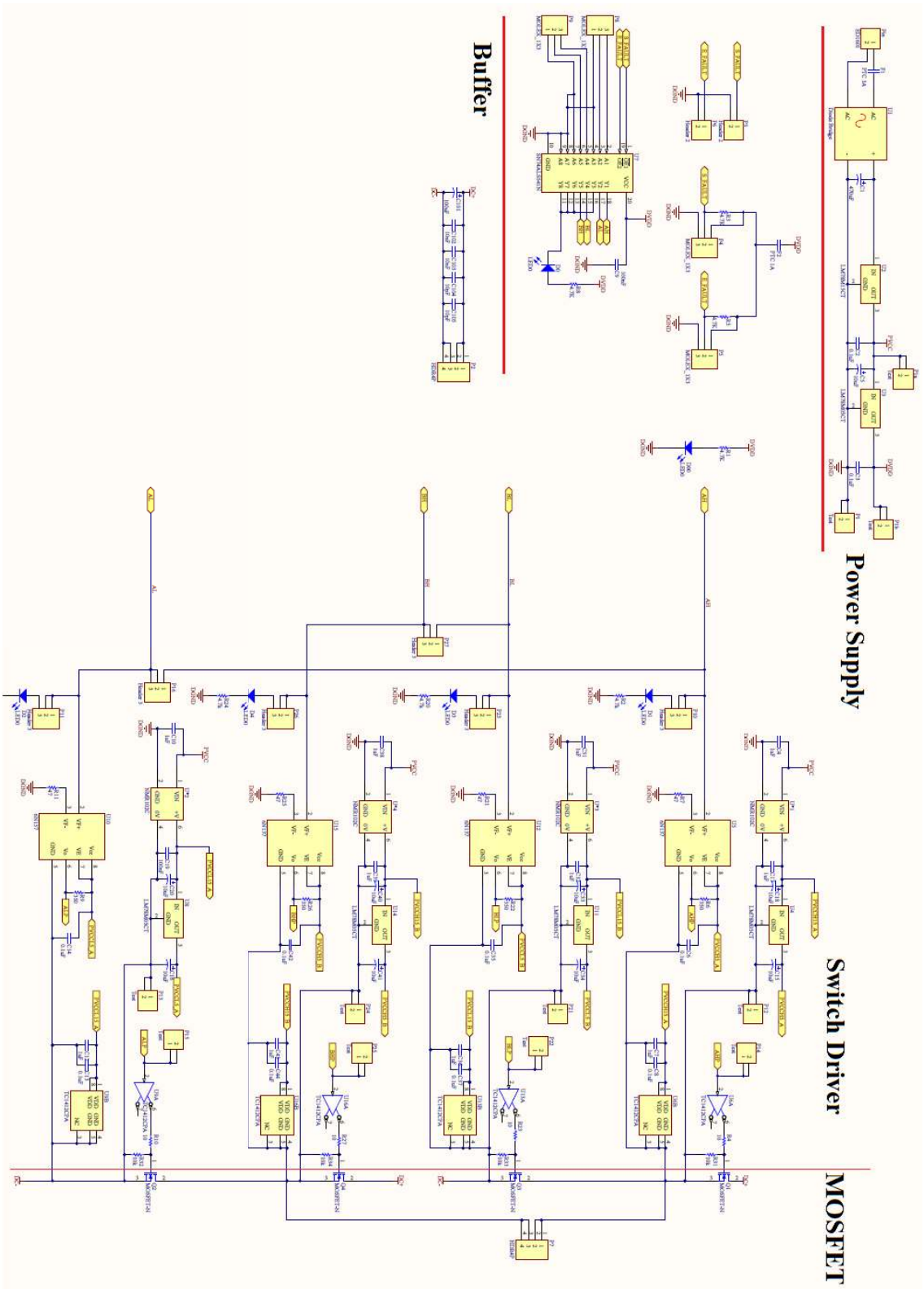
Fig. C.2. Schematic of the primary DC-AC inverter.

The power supply for the ICs on prototype is shown in Fig. C.3. The AC power from a utility outlet is transferred to PVCC (15 VDC) by LM78M15CT, and the PVCC is transferred to DVDD (5 VDC) by LM78M05CT. PVCC is used to provide power to gate drivers and DVDD provides power to buffer IC. In order to realize isolation between the power section and digital section of the board, isolated DC/DC converters are used to supply power to switch drivers directly. This part is not shown here but described in the part of the switch driver.
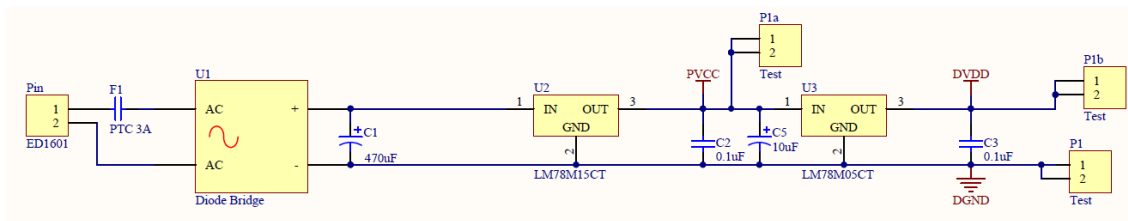
Fig. C.3. The power supply in the schematic.

The signal buffer is shown in Fig. C.4. The IC SN74ALS541N is used to provide positive logic output from the driving signal generated by MCU. The output signals of the buffer will be sent to the switch drivers. The main function of the buffer circuit is to do the Fault control: when the MCU detects over-current in the system, a Fault signal will be sent to the buffer and disable the buffer output; the inverter is shut down then. Note that the logic relation of the buffer is important. Because the common MOSFET drivers may apply negative or positive logic between the output and input, designers must confirm that the overall logic from the MCU to the final gate driver is positive.

146
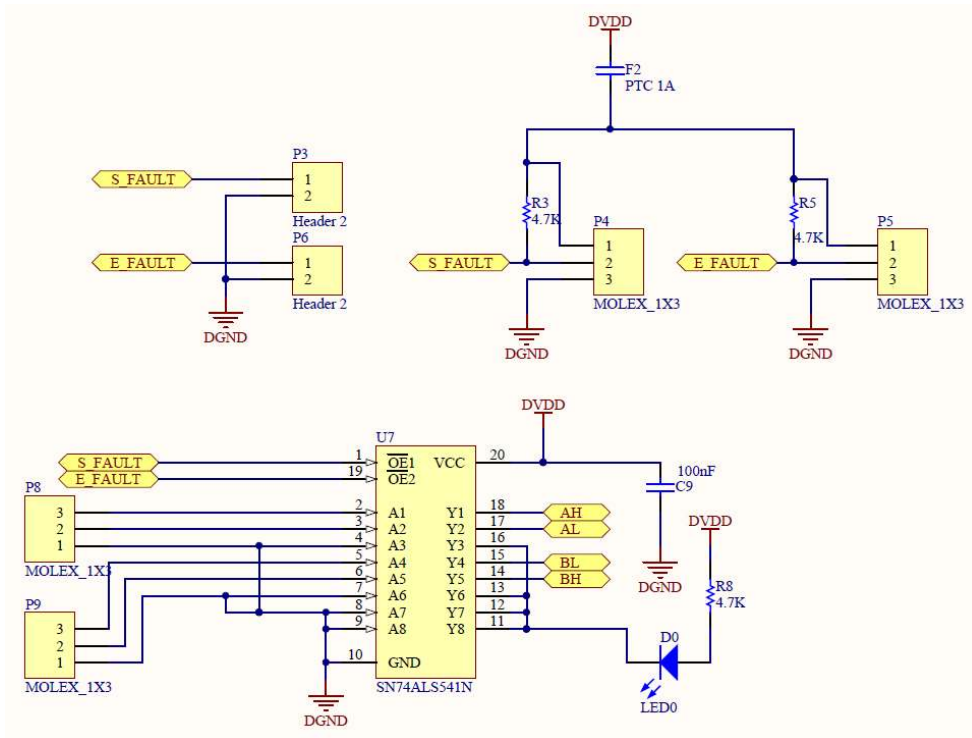
Fig. C.4. Signal buffer in the schematic.

One branch of a switch driver and a MOSFET (Q1) is shown in Fig. C.5. The output of the buffer is firstly sent to an optocoupler 6N137, which realizes isolation between the power section and digital section. The output of the optocoupler is connected to the input of the switch driver TC1412CPA (the output voltage level of the optocoupler is not high enough for driving the MOSFETs). Meanwhile, each branch of driver&switch has a set of power supply modules: NMR102C (MER1S1515SC) and LM78M05CT. The NMR102C is an isolated DC/DC converter to provide power to the LM78M05CT, who supplies power for the switch driver. To detect whether there is a driving signal from the buffer or not, an LED is connected to the input of the optocoupler.

147
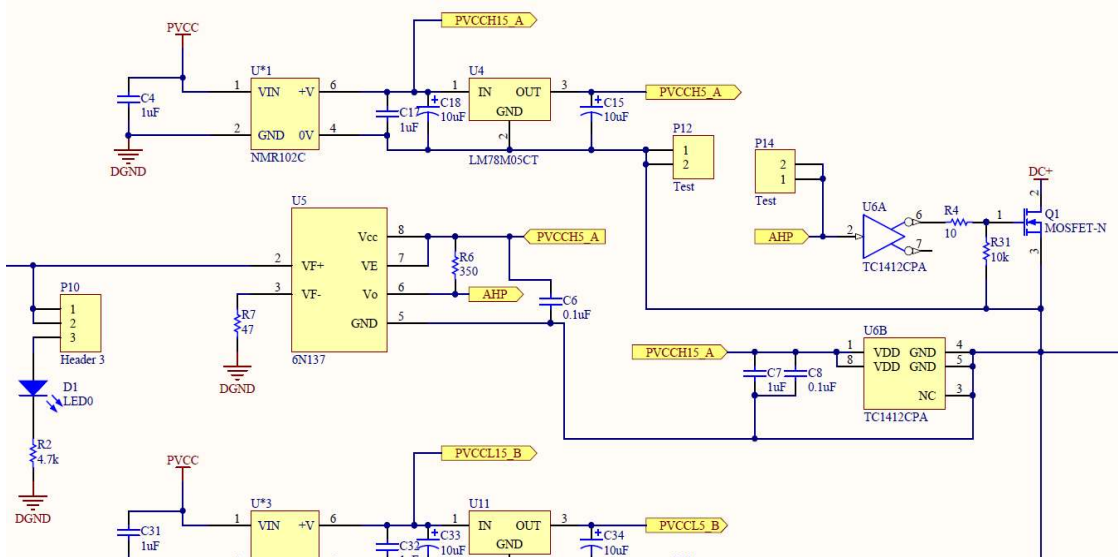
Fig. C.5. One leg of switch driver and MOSFET in the schematic.

The PCB layout of the DC-AC inverter is shown in Fig. C.6. Note that in the PCB, there are some spare pins around the main circuit. The spare pins are used to further adjust the circuit if necessary. In practical system, the space for heatsink is not used; the board is placed above a heatsink (L30cm×W20cm×H10cm) and MOSFETs are arranged at the back of the board and fixed at the heatsink. The bill of main material is summarized, as listed in Table A.1.
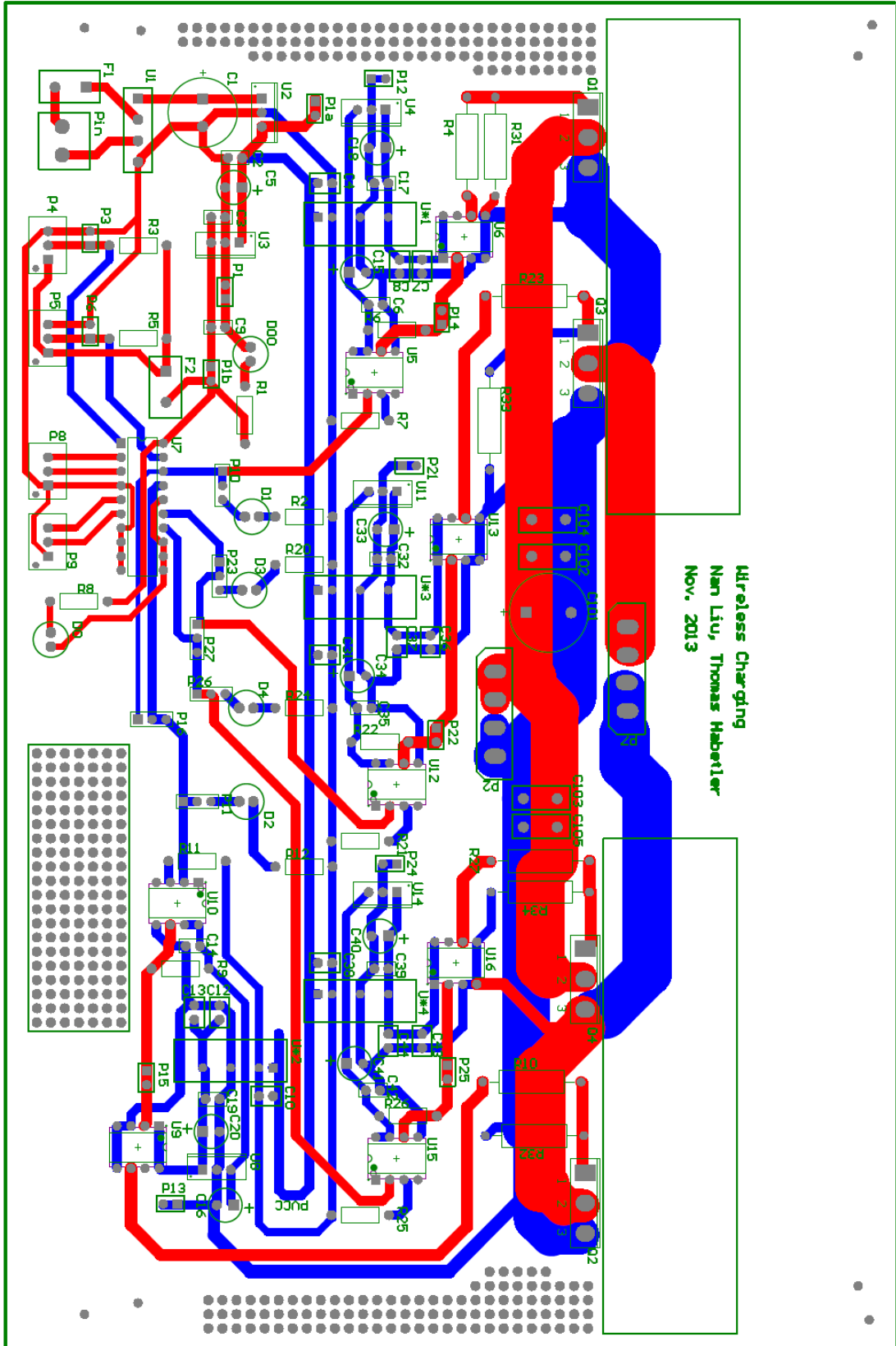
Fig. C.6. PCB layout the primary DC-AC inverter.

Table A.1. Bill of Materials of DC-AC Inverter

Item #	Designator	Part Number	Description	Quality
1	C1	94SA477X0016GNP	Solid Aluminum Capacitor with Organic, Semiconductor Electrolyte: 470uF, 16V,	1
2	U1	2KBP01M	Diode Bridge	1
3	U2	LM78M05CT	3-Terminal Positive Voltage Regulators	1
4	U3, U4, U8, U11, U14	LM78M05CT	3-Terminal Positive Voltage Regulators	5
5	U5, U10, U12, U15	6N137	OptoCoupler	4
6	U6, U9, U13, U16	TC1412CPA	2A High-Speed MOSFET Driver, Inverting,	4
7	U7	SN74ALS541N	Octal Buffer/Driver with 3-State Outputs	1
8	U*1, U*2, U*3, U*4	MER1S1515SC	Isolated DC/DC Converter, 15V/15V, 1W	4
9	Q1, Q2, Q3, Q4	FDH44N50	N-Channel MOSFET, 500V, 44A	4

C.2 Design of Load-Phase-Detecting System

The prototype of the load-phase-detecting system captures the input AC current and voltage and transfer the phase shift between the two signals to be a DC voltage output. The schematic of the load-phase-detecting system is shown in Fig. C.7. The main structure consists of three parts: the power supply for all ICs, the two loops for signal transformation, and the logic circuits. The structure is shown in Fig. 3.5. The signal of input AC current is captured by a shunt resistor, and the input AC voltage is captured by a resistor divider.
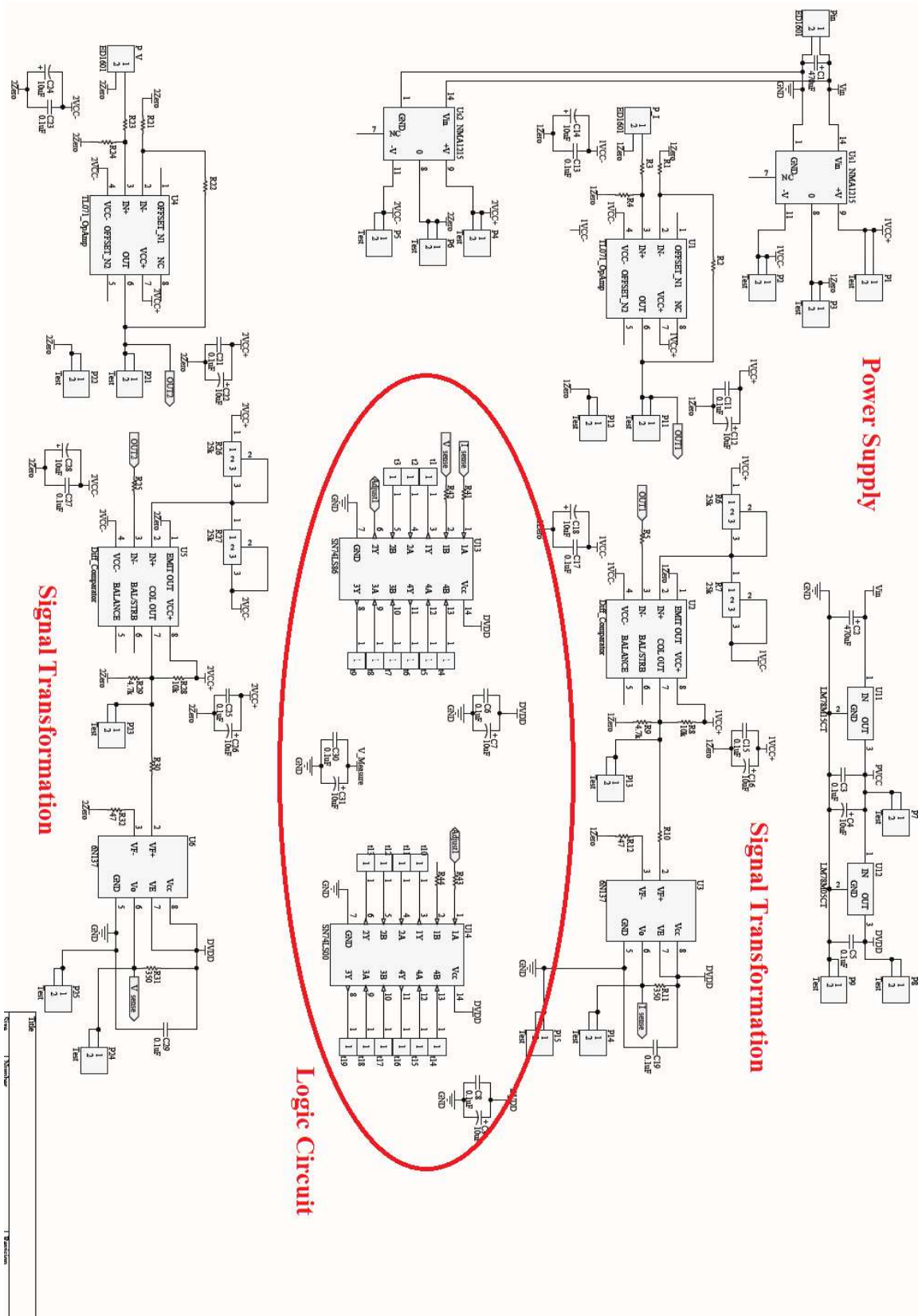
Fig. C.7. Schematic of prototype of the load-phase-detecting system.

151

The part of the power supply is similar to the power supply used in the primary DC-AC inverter.

The part of signal transformation is formed by an OpAmp circuit, a differential comparator, and an optocoupler, as shown in Fig. C.8. The captured voltage or current signal is sent to the OpAmp circuit and amplified to a signal in the same shape. A differential comparator transfers the amplified waveform to a square waveform, with the same zero-crossing point of the original waveform. The pin 2 of the differential comparator is connected with a DC voltage offset, which is used to adjust the error by parasitic elements in the circuits. The optocoupler realizes the isolation between the
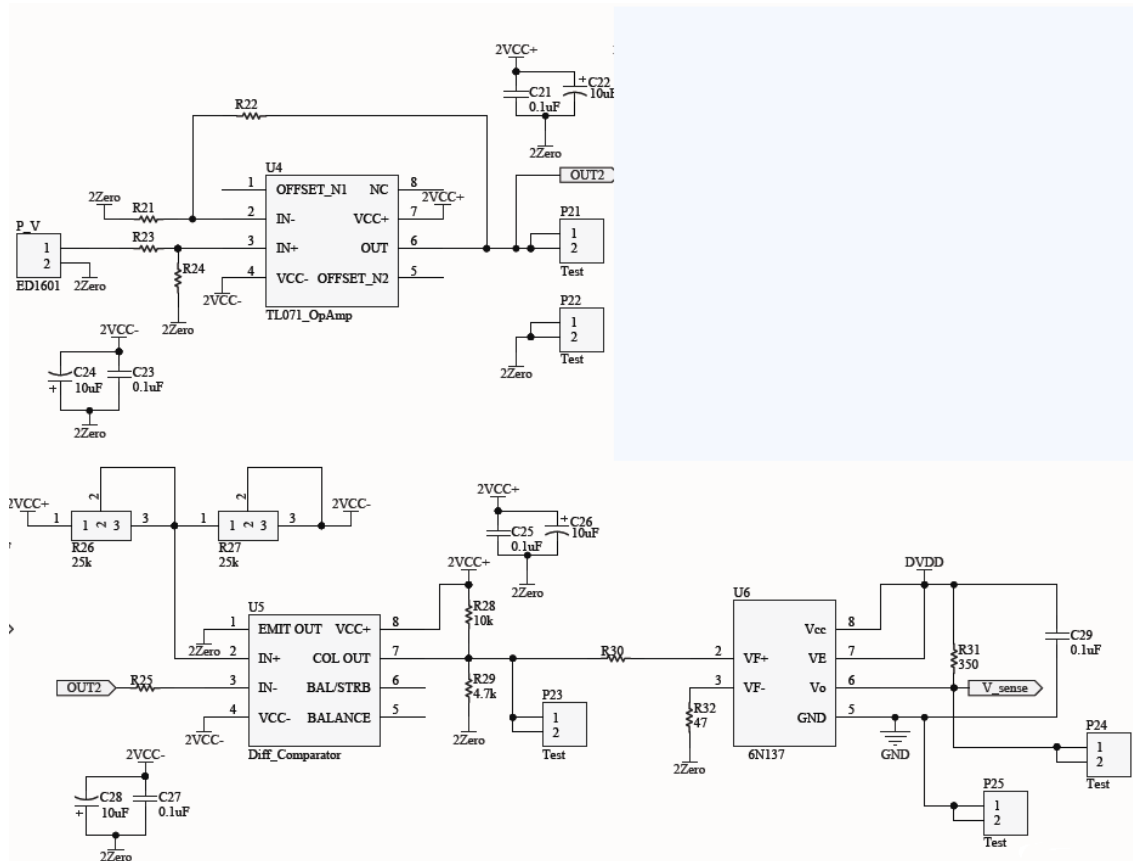
Fig. C.8. Signal-transformation module in the schematic of control system.

152

power section and digital section.

The part of the logic circuit is shown in Fig. C.9. An OR-Gate IC (SN74LS86) and NAND-Gate IC (SN74LS00) are used to achieve the logic calculation. For free choice of the logic relation, all the input and output pins of logic ICs are left without connections. The power supply DVDD of the logic circuit is in the digital section.
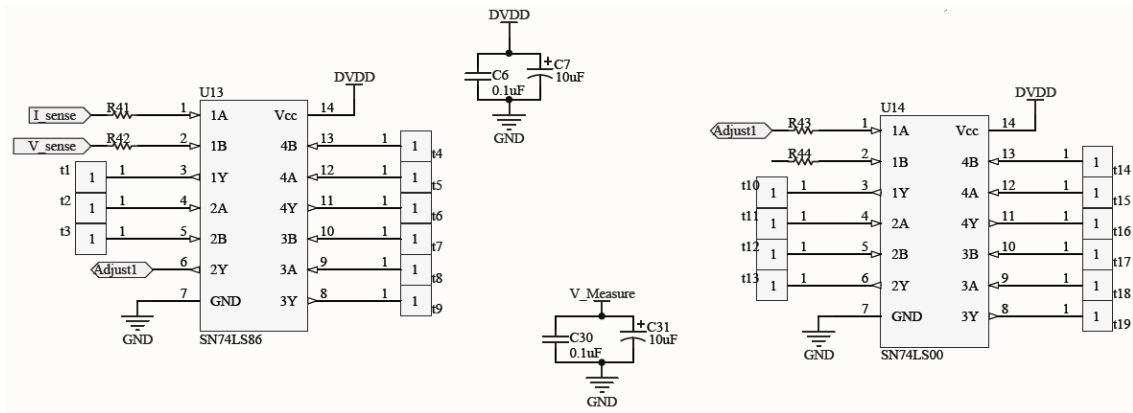
Fig. C.9. The logic circuit in the schematic of control system.

The PCB layout of the DC-AC inverter is shown in Fig. C.10.
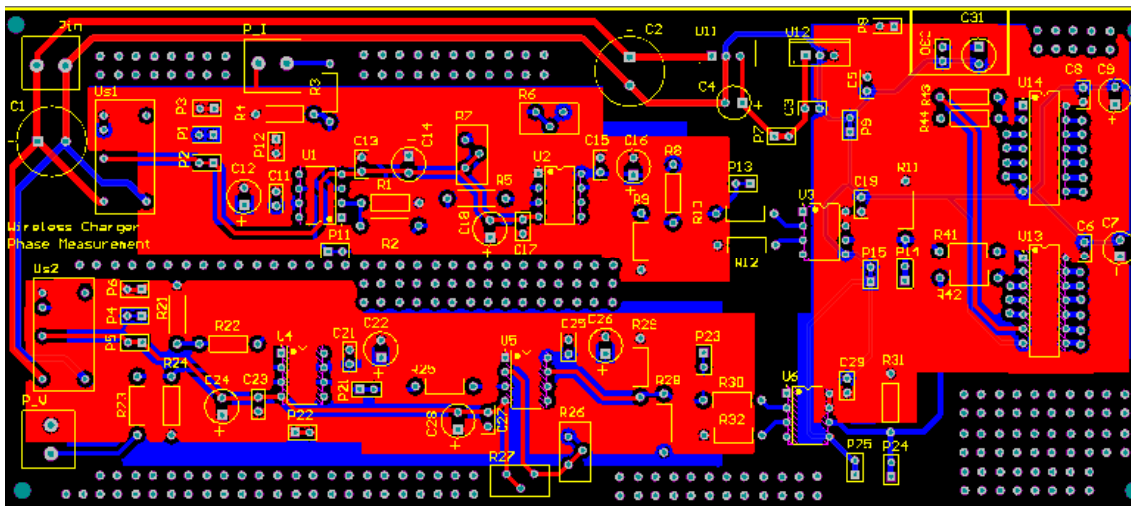
Fig. C.10. PCB layout the load-phase-detecting loop.

The bill of main materials used in load-phase-detecting system is listed in Table A.2.

Table A.2. Bill of Materials of Load-Phase-Detecting

Item #	Designator	Part Number	Description	Quality
1	U1, U4	TL071	Low-Noise JFET-Input Op-Amp	2
2	U2, U5	LM393	Low-Offset Voltage, Dual Comparators	2
3	U3, U6	6N137	OptoCoupler	2
4	U13	SN74LS86	Quad 2-Input Exclusive OR Gate	1
5	U14	SN74LS00	Quad 2-Input positive-NAND Gate	1
6	Us1, Us2	NMA1215	Isolated 1W Dual Output DC/DC Converters	2

A video recording operation of the load-phase-detecting system is online: https://www.youtube.com/watch?v=8TL2hLWf0lM .

C.3   Design of MCU Board

A FPGA interfacing board and a DSP evaluation kit are used as the MCUs of the charger. The prototype of the on-board charger applies the same MCU to do the dual-mode control. The FPGA and DSP boards are originally designed by Dr. Jose Alex Restrepo and Dr. Siwei Cheng.

C.3.1   FPGA

The PCB layout of the FPGA board is shown in Fig. C.11. The The structure of the PCB mainly include 3 PWM output channels that are connected to the input ports of the DC-AC inverter board, 8 fiber optic transmitters and receivers for information transmission between FPGA and DSP, JTAG programming circuit, additional pins for testing the FPGA boards, etc.
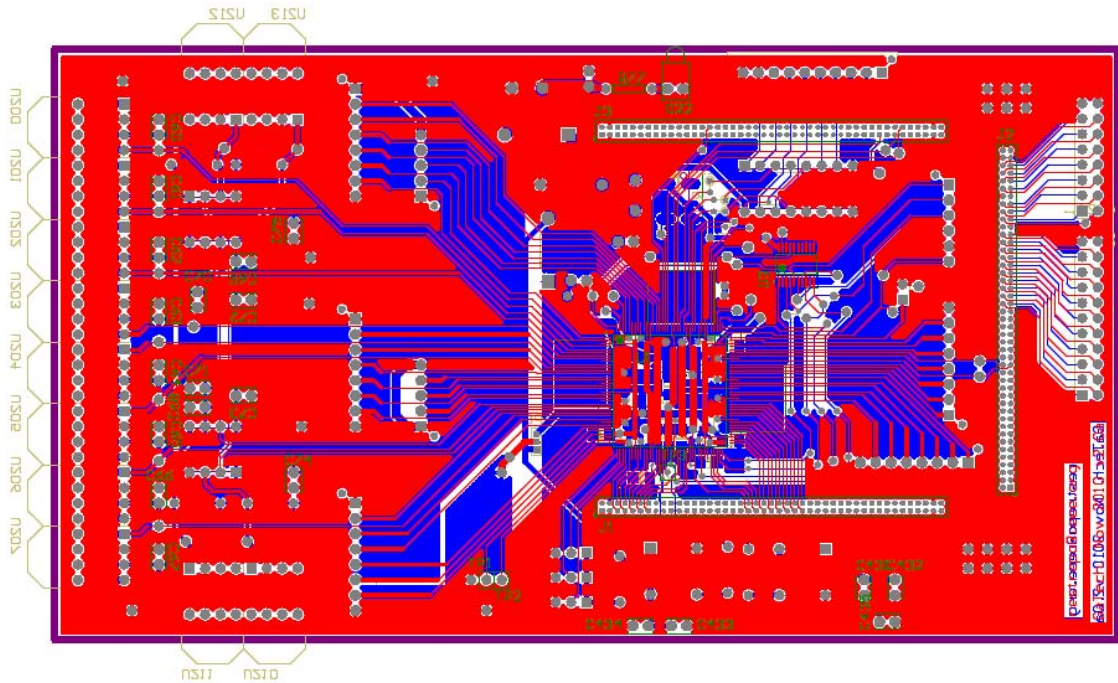
Fig. C.11. PCB layout the FPGA interface.

C.3.2 DSP

ADSP-21369 EZ-KIT from Analog Device is used in the prototype system. The more details of the DSP can be acquired by the user manual. The flowchart of the DSP codes is shown in Fig. C.12. The DSP codes are based on the frequency control used in the proposed UIC. Note that the FPGA board realizes the A/D conversion and finally generating PWM switching signals to the primary DC-AC inverter.

The DSP Codes used in the charger are:
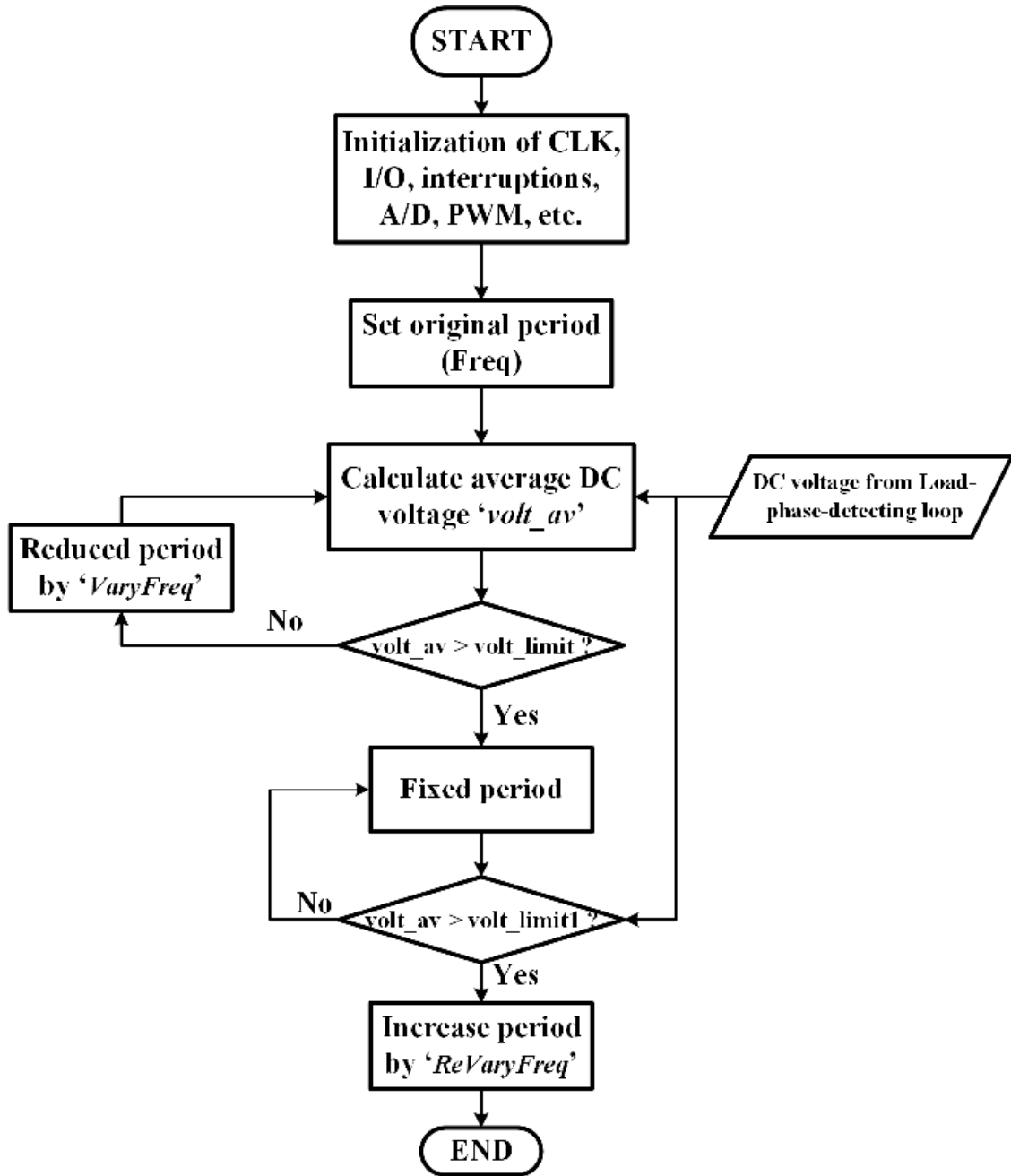
Fig. C.12. The flowchart of the DSP codes for frequency control in the proposed UIC.

"

```
#include<21369.h>
#include<cdef21369.h>
#include<def21369.h>
#include<math.h>
```

```c
#include<signal.h>
#include<stdio.h>
#include<sysreg.h>


#define  SetIOP1(addr, val)  (* (volatile int *) addr) = (val)
#define  GetIOP1(addr)       (* (volatile int *) addr)

#define M_SQRT3        1.73205080756887719317
#define  M_2PI              6.28318530717958647692528676559

#define PWM_RESET            0x0C000000
#define PWM_OFF              0x0C000001
#define PWM_ON               0x0C000002
#define  PWMDT               0x0C000005
#define  PWMPMIN             0x0C000006
#define  AD_IRQCNT           0x0C000008

#define PWM_A1               0x0C000010
#define PWM_B1               0x0C000011
#define PWM_C1               0x0C000012
#define PWM_A2               0x0C000013
#define PWM_B2               0x0C000014
#define PWM_C2               0x0C000015
#define PWM_A3               0x0C000016
#define PWM_B3               0x0C000017
#define PWM_C3               0x0C000018
#define  ADQ_PTRG            0x0C000019
#define  PWM_RDY1            0x0C00001A
#define  PWM_RDY2            0x0C00001B
#define  IGBT_2              0x0C00001E
#define  IGBT_3              0x0C00001F

#define  PWM_MAX             0x0C000050
#define  PWMMFLG             0x0C000051

#define  AD_CH0              0x0C000020
#define  AD_CH1              0x0C000021
#define  AD_CH2              0x0C000022
#define  AD_CH3              0x0C000023
#define  AD_CH4              0x0C000024
#define  AD_CH5              0x0C000025

#define  CLK_SEL             0x0C000030

//#defineSPEED0              0x0C000040
//#defineSPEED1              0x0C000041
#define  ROT_POS             0x0C000047
```

```c
#define  DT                              120// :  dead time = DT * (1/200 MHz) = DT*5 ns

#define TFINAL              9900 //3600.0// : total experiment time(sec)
#define  Fs                              1e5// : the PWM control frequency, 100 kHz

#define  GAIN_CH0           1.86    //0.03  the  gain  (you need to change those values for your
acquisition board)
#define  OFFSET0                        2048  // 2048 is the offset
#define  LEN                            2000

void InitPLL_SDRAM(void);
void InitSRU(void);

section ("seg_sdram")

float data1a[LEN];

int seed;
float vin;


//
void g_isr0 (int sig)
{

}

void g_isr1 (int sig)
{
int tmp;
float gain;

seed=2;
tmp=GetIOP1(AD_CH0)&0xFFF;
gain=GAIN_CH0;
//tmp1=tmp;
if(tmp<3000)
  gain=1.770;
if(tmp<2850)
  gain=1.700;
if(tmp<2750)
  gain=1.635;
if(tmp<2700)
  gain=1.600;
if(tmp<2600)
  gain=1.605;
if(tmp<2400)
```

```c
   gain=1.619;

 vin=(gain * (tmp - OFFSET0));


}

 void main(void)
 {
 int tmp,i,j,k;
 float Period, Da,Db,Dc;


 int VaryFreq;       //Test 07/08/2014, the variance of the period for each change.
 int No_measure;  //Test 08/10/2014, the times need for measurement of voltage before the final variance of
freq
 int count;         //times left for average calculation
 float volt_av;     //Test 08/10/2014, need to get the average value
 int unit;
 float volt_limit;  //the voltage when the phase_diff>0
 float volt_test;   //Test 08/10/2014, for observe the volt_av value


 VaryFreq = 4;     //Test 07/08/2014, if phase_diff<0, decrease the period by 4.
 No_measure = 5;  //Test 08/10/14, the voltage needs to be higher than a value by # times of measurement
 count = No_measure;
 volt_av = 0;
 unit = 1;
 volt_limit = 200.0;
 volt_test = 0.0;


 InitPLL_SDRAM();
 InitSRU();
 tmp=*((int *)SYSCTL);
 *((int *)SYSCTL)=tmp|0x0130000 |IRQ0EN | IRQ1EN;


 tmp=(*((int *)EPCTL))&0xFFFFFFE7;
 *((int *)EPCTL)=tmp|0x20;                         // Bank3 no sdram core high priority
 tmp=*((int *)AMICTL3);
 *((int *)AMICTL3)=AMIEN|
 BW32|
// PKDIS|
 WS4|
 HC1|
 IC1|
 AMIFLSH|
 RHC1|//;//|
 PREDIS;
 asm ("bit set mode2 IRQ0E;") ;
 asm ("bit set mode2 IRQ1E;") ;
```

```c
//interrupt(SIG_IRQ0, g_isr0);    // enable high priority timer interrupt
 interrupt(SIG_IRQ1, g_isr1);
 //sysreg_bit_set(sysreg_MODE2,IRQ0E);

SetIOP1(PWM_RESET,00);
asm("nop;");
asm("nop;");
SetIOP1(PWM_OFF,00);
asm("nop;");
SetIOP1(PWM_MAX,2000);          //
asm("nop;");
SetIOP1(AD_IRQCNT,3);
asm("nop;");
//SetIOP1(PWMDT,104);
SetIOP1(PWMDT,80);               // Dead time must be between 16 and 992
asm("nop;");
SetIOP1(PWMPMIN,50); // PMIN is between 0 and 255 (there is no checking agianst PWMMAX
asm("nop;");
SetIOP1(PWM_ON,00);
asm("nop;");
SetIOP1(CLK_SEL,00);

asm("nop;");
SetIOP1(PWM_MAX,600); // 500< PWMMAX < 40000  //Period of PWM, 1000 leads to 100kHz
asm("nop;");
SetIOP1(PWM_A1,300);//Duty cycle must be in the range (PMIN+DT/2) =< DUTY < PWMMAX-
(PMIN+DT/2)
SetIOP1(PWM_B1,300);//to have switching in the output
SetIOP1(PWM_C1,300);
SetIOP1(PWM_RDY1,0);
asm("nop;");
asm("nop;");
//SetIOP1(ADQ_PTRG,20);

//tmp=0;

seed=0;

k=0;
j=0;

Period = 1000;  //test control 07/08

for(i=0;i<TFINAL*Fs;i++)
{

        //waiting for interrupt coming from FPGA
```

```
 do{
         asm("nop;");
  }while(seed!=2);


//Test Control 08/10/2014, calculate average volt,
  volt_av = volt_av + vin;
         count = count - unit;

if(count<1)  //Test Control 08/10/2014, collected enough values of volt
{
         volt_av = volt_av/No_measure;
         volt_test = volt_av;      //for observing the volt_av value
}
         ////////////

//Test Control 07/08, determine measured voltage
if((volt_test<volt_limit)&&(count<1))   // tried revising: 'volt_test<volt_limit'
         Period = Period - VaryFreq;

////

do{

         //Test, delete//Period = 1000;
         Da = Period/2;
         Db = Period/2;
         Dc = Period/2;

         SetIOP1(PWM_MAX,Period);

         SetIOP1(PWM_A1,(int)Da);
         SetIOP1(PWM_B1,(int)Db);
         SetIOP1(PWM_C1,(int)Dc);

         //SetIOP1(PWM_A3,(int)Da);
         //SetIOP1(PWM_B3,(int)Db);
         //SetIOP1(PWM_C3,(int)Dc);

         SetIOP1(PWM_RDY1,0);
         //SetIOP1(PWM_RDY3,0);

                 asm("nop;");
          }while(seed!=2);


         //Test control 07/08, delay for a while
         for(j=0;j<70*Fs;j++)
```

```
                {
                        asm("nop;");
                        asm("nop;");
                        asm("nop;");
                        asm("nop;");
                        asm("nop;");
                        asm("nop;");
                }
                //////////////////////////////


//Test Control 07/08&09/10, this sentence will change the control as:
//if the voltage is higher than a limit, the frequency is finally fixed and cannot be adjusted anymore
if((volt_av>volt_limit)&&(count<1))
                VaryFreq = 0;

if(count<1)
{
                count = No_measure;      //reset the count after each variance of the freq or average calculation
                volt_av = 0;
}
/////////////

 seed=0;

}

//}    //Testing repeat, END

for(i=0;i<2100000;i++)
{
 set_flag(15,1);  // meaning?
 do{
                        asm("nop;");
                }while(seed!=2);
 seed=0;
 set_flag(15,0);

 if(i<LEN)
  data1a[i]=vin;


}

SetIOP1(PWM_OFF,00);

for(;;)
 {
```

```
 asm("nop;");
 asm("nop;");
 asm("nop;");
 asm("nop;");
 asm("nop;");
 asm("nop;");
 }

 }
//FINISH MAIN
 ”
```

C.4 Design of Sensor Board

The sensor board is originally designed by Dr. Jose Alex Restrepo. The sensor board is used in the control system of the proposed UIC and the control system of the on-board charger. For the primary charger, the sensor board is mainly used to capture the DC output voltage of the load-phase-detecting system. For the on-board charger, the sensor board is used to capture the DC input current and DC output voltage of the DC-DC converter.

The board has 4 channels: 2 current-measurement channels, 1 voltage-measurement channel, and 1 additional channel for either voltage or current measurement (according to the sensor used). As shown in Fig. C.13, a typical channel consists of a hall-effect sensor, an amplifier, a voltage-offset part, and an A/D converter. Hall-effect sensors are used for isolation between the power circuit and digital circuit. The signal "*Clk*" and "*Cnvst*" are received from the FPGA board as clock signal and start of A/D conversion. The signal "*DATA_3*" is the value by A/D conversion and will be transmitted to the FPGA for further analysis. The PCB layout of the sensor board is shown in Fig. C.14.
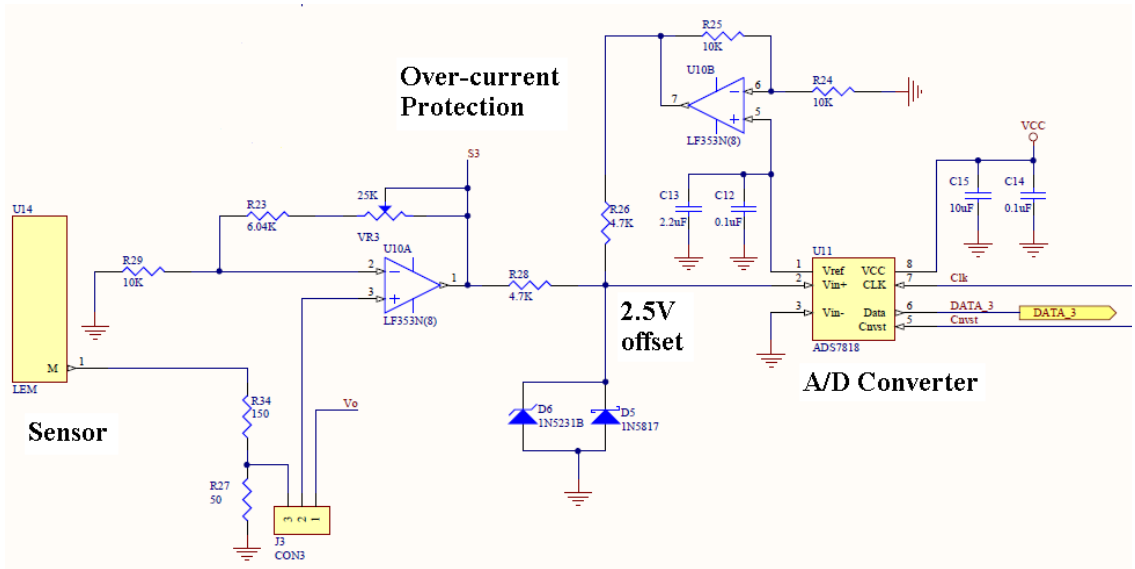
Fig. C.13. Schematic of one channel used in the sensor board.
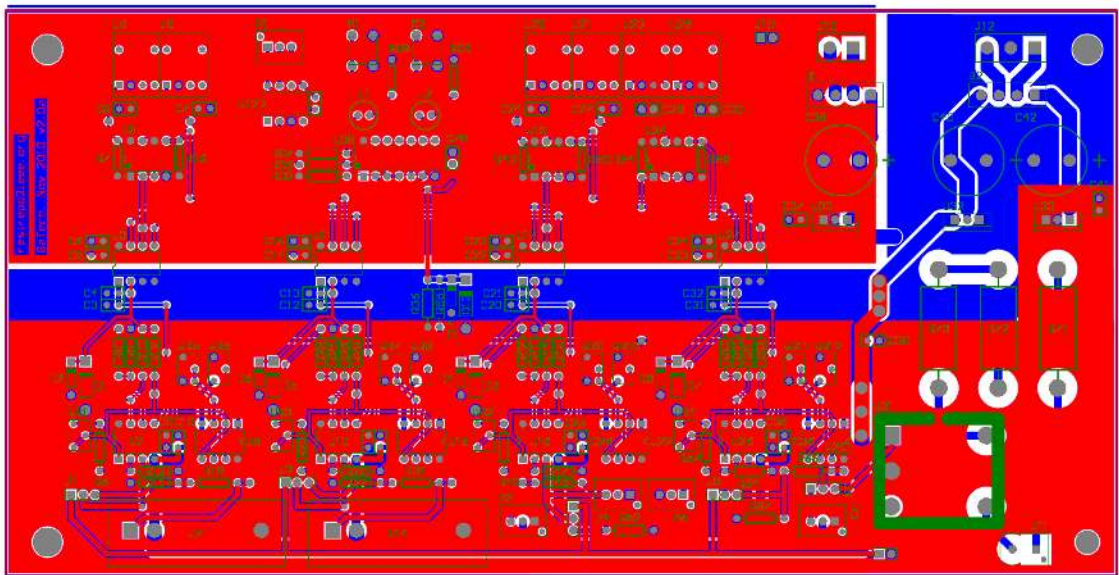
Fig. C.14. PCB layout of the sensor board.

164

C.5   Design of On-board Charger

For the on-board chargers are different with 2 different *LC* circuits: the on-board charger with an S-connected *LC* circuit applies a boost converter, and the on-board charger with a P-connected *LC* circuit applies a buck converter. For system simplification, the components used in the 2 DC-DC converters are same. The bill of material of the DC-DC converter is listed in Table C.3.

Table C.3. Bill of Materials of On-board DC-DC Converters

Item #	Part	Description	Quality
1	MOSFET	FCH072N60-ND, N-Channel MOSFET, 600V, 52A	1
2	Diode	APT20SCD65K, SiC Schottky Diode, 650V, 32A	1
3	DC Inductor	550 µH, T400-60D Core, 72 coil turn#	1
4	Output DC Capacitor	944U141K102ACM, 140 µF, 10%, 1KVDC	1
5	Diode bridge	STTH3006, ultrafast, 600V, 30A	4
6	Input DC Capacitor	300µF, 1000V, Aluminum capacitor	1

The main function of the DSP codes used in the on-board charger is as following, with the same initialization as the codes used in the DSP of the primary charger:

"

```
void main(void)
{
 int tmp,i,j,k;          // parameters for adjustment
 float Period, Da,Db,Dc;  // period and duty cycle
 float Kp, Ki;           // PI control parameters
 int Vref;               // Output Voltage reference
 float Ts =25e-6;        // 40kHz
 float err, err_i, err1;      // error and integrated error
```

```c
InitPLL_SDRAM();
InitSRU();
tmp=*((int *)SYSCTL);
*((int *)SYSCTL)=tmp|0x0130000 |IRQ0EN | IRQ1EN;

tmp=(*((int *)EPCTL))&0xFFFFFFE7;
*((int *)EPCTL)=tmp|0x20;                       // Bank3 no sdram core high priority
tmp=*((int *)AMICTL3);
*((int *)AMICTL3)=AMIEN|
BW32|
// PKDIS|
WS4|
HC1|
IC1|
AMIFLSH|
RHC1|//;//|
PREDIS;
asm ("bit set mode2 IRQ0E;") ;
asm ("bit set mode2 IRQ1E;") ;

//interrupt(SIG_IRQ0, g_isr0);    // enable high priority timer interrupt
interrupt(SIG_IRQ1, g_isr1);
//sysreg_bit_set(sysreg_MODE2,IRQ0E);


SetIOP1(PWM_RESET,00);
asm("nop;");
asm("nop;");
SetIOP1(PWM_OFF,00);
asm("nop;");
SetIOP1(PWM_MAX,2000);          //
asm("nop;");
SetIOP1(AD_IRQCNT,3);
asm("nop;");
//SetIOP1(PWMDT,104);
SetIOP1(PWMDT,80);              // Dead time must be between 16 and 992
asm("nop;");
SetIOP1(PWMPMIN,50); // PMIN is between 0 and 255 (there is no checking agianst PWMMAX
asm("nop;");
SetIOP1(PWM_ON,00);
asm("nop;");
SetIOP1(CLK_SEL,00);

asm("nop;");
SetIOP1(PWM_MAX,600); // 500< PWMMAX < 40000  //Period of PWM, 1000 leads to 100kHz
asm("nop;");
```

```
SetIOP1(PWM_A1,300);//Duty cycle must be in the range (PMIN+DT/2) =< DUTY < PWMMAX-
(PMIN+DT/2)

SetIOP1(PWM_B1,300);//to have switching in the output

SetIOP1(PWM_C1,300);

SetIOP1(PWM_RDY1,0);

asm("nop;");
asm("nop;");
//SetIOP1(ADQ_PTRG,20);

//tmp=0;

/////////////////////// SETTINGs for DC-DC control, April, 2015

SetIOP1(PWM_MAX,2500);    //frequency=40kHz, Apr,2015
err = 0;
err_i = 0;
err1 = 0;
Ki = 3*2500*Ts*0.1;      //'2500': DutyCycle=1 => Da=2500, '/40000'=> '*Ts'
Kp = 0.001*2500;
Vref = 40;

seed=0;

k=0;
j=0;

set_flag(15,1);  //added Apr.12, 2015

SetIOP1(PWM_A1,(int)(2500*0.7)); // set duty cycle during the frequency-tracking process
SetIOP1(PWM_B1,(int)(2500*0.7));
SetIOP1(PWM_C1,(int)(2500*0.7));

do{
        asm("nop;");
   }while(v_m<100);

for(i=0;i<TFINAL*Fs;i++)
{

        //waiting for interrupt coming from FPGA
 do{
        asm("nop;");
   }while(seed!=2);
```

```
    set_flag(15,0); //added Apr.12, 2015

do{

        err = Vref - v_m;
        err1 = fclip(err_i + Ki*err, 1250);
        err_i = err1;
        Da = 1200 + fclipf(Kp*err + err_i, 1050); //reduce the limit to 1200;
        Db = Da;
        Dc = Da;

        SetIOP1(PWM_A1,(int)Da);
        SetIOP1(PWM_B1,(int)Db);
        SetIOP1(PWM_C1,(int)Dc);


        SetIOP1(PWM_RDY1,0);


                asm("nop;");
          }while(seed!=2);

    seed=0;


    set_flag(15,1); //added Apr.12, 2015

////////////////////////////////////////////
//for(j=0;j<70*Fs/2;j++)   //added Apr.12, 2015, observe 'seed'
//         {
//                 asm("nop;");
//                 asm("nop;");
//                 asm("nop;");
//                 asm("nop;");
//                 asm("nop;");
//                 asm("nop;");
//         }

}



for(i=0;i<2100000;i++)
{
 set_flag(15,1); // meaning?
 do{
        asm("nop;");
          }while(seed!=2);
```

```
  seed=0;
 set_flag(15,0);

 if(i<LEN)
  data1a[i]=v_m;


}


SetIOP1(PWM_OFF,00);

for(;;)
 {
 asm("nop;");
 asm("nop;");
 asm("nop;");
 asm("nop;");
 asm("nop;");
 asm("nop;");
 }

}
"
```

BIBLIOGRAPHY

[1]   M. Yilmaz and P. T. Krein, "Review of Battery Charger Topologies, Charging Power Levels, and Infrastructure for Plug-In Electric and Hybrid Vehicles," *Power Electronics, IEEE Transactions on,* vol. 28, pp. 2151-2169, 2013.

[2]   S. Haghbin, S. Lundmark, M. Alakula, and O. Carlson, "Grid-Connected Integrated Battery Chargers in Vehicle Applications: Review and New Solution," *Industrial Electronics, IEEE Transactions on,* vol. 60, pp. 459-473, 2013.

[3]   D. Aggeler, F. Canales, H. Zelaya-De La Parra, A. Coccia, N. Butcher, and O. Apeldoorn, "Ultra-fast DC-charge infrastructures for EV-mobility and future smart grids," in *Innovative Smart Grid Technologies Conference Europe (ISGT Europe), 2010 IEEE PES*, 2010, pp. 1-8.

[4]   L. Nan and T. G. Habetler, "Design of a Universal Inductive Charger for Multiple Electric Vehicle Models," *Power Electronics, IEEE Transactions on,* vol. 30, pp. 6378-6390, 2015.

[5]   J. T. Boys, G. A. Covic, and A. W. Green, "Stability and control of inductively coupled power transfer systems," *Electric Power Applications, IEE Proceedings -,* vol. 147, pp. 37-43, 2000.

[6]   SAE, "SAE Electric Vehicle and Plug-in Hybrid Electric Vehicle Conductive Charge Coupler," ed: SAE, 2010.

[7]   M. Grenier, M. G. Hosseini Aghdam, and T. Thiringer, "Design of on-board charger for plug-in hybrid electric vehicle," in *Power Electronics, Machines and Drives (PEMD 2010), 5th IET International Conference on*, 2010, pp. 1-6.

[8]   L. Nan and T. G. Habetler, "A study of designing a universal inductive charger for Electric Vehicles," in *Industrial Electronics Society, IECON 2013 - 39th Annual Conference of the IEEE*, 2013, pp. 4528-4533.

[9]   H. Ming-Shi, Y. Po-Yi, H. Jia-Rong, and L. Chang-Hung, "Novel bi-directional AC-DC converter for electrical vehicle battery testing," in *IECON 2011 - 37th Annual Conference on IEEE Industrial Electronics Society*, 2011, pp. 1480-1485.

[10]   H. H. Wu, A. Gilchrist, K. Sealy, P. Israelsen, and J. Muhs, "A review on inductive charging for electric vehicles," in *Electric Machines & Drives Conference (IEMDC), 2011 IEEE International*, 2011, pp. 143-147.

[11]   Z. Y. Sitthisak Kiratipongvoot, Chi Kwan Lee, Siu Shing Ho, "Design a High-Frequency-Fed Unity Power-Factor AC–DC Power Converter for Wireless Power

Transfer Application," presented at the Energy Conversion Congress and Exposition (ECCE), 2015 IEEE.

[12]   P. Sung-Yeul, H. Miwa, B. T. Clark, D. Ditzler, G. Malone, N. S. D'Souza, *et al.*, "A universal battery charging algorithm for Ni-Cd, Ni-MH, SLA, and Li-Ion for wide range voltage in portable applications," in *Power Electronics Specialists Conference, 2008. PESC 2008. IEEE*, 2008, pp. 4689-4694.

[13]   O. H. Stielau and G. A. Covic, "Design of loosely coupled inductive power transfer systems," in *Power System Technology, 2000. Proceedings. PowerCon 2000. International Conference on*, 2000, pp. 85-90 vol.1.

[14]   Z. Cong, C. Rui, E. Faraci, Z. U. Zahid, M. Senesky, D. Anderson, *et al.*, "High efficiency contactless power transfer system for electric vehicle battery charging," in *Energy Conversion Congress and Exposition (ECCE), 2013 IEEE*, 2013, pp. 3243-3249.

[15]   H. H. Wu, A. Gilchrist, K. Sealy, and D. Bronson, "A 90 percent efficient 5kW inductive charger for EVs," in *Energy Conversion Congress and Exposition (ECCE), 2012 IEEE*, 2012, pp. 275-282.

[16]   H. Ishihara, F. Moritsuka, H. Kudo, S. Obayashi, T. Itakura, A. Matsushita, *et al.*, "A voltage ratio-based efficiency control method for 3 kW wireless power transmission," in *Applied Power Electronics Conference and Exposition (APEC), 2014 Twenty-Ninth Annual IEEE*, 2014, pp. 1312-1316.

[17]   A. Khaligh and S. Dusmez, "Comprehensive Topological Analysis of Conductive and Inductive Charging Solutions for Plug-In Electric Vehicles," *Vehicular Technology, IEEE Transactions on,* vol. 61, pp. 3475-3489, 2012.

[18]   L. Xun and S. Y. Hui, "Optimal Design of a Hybrid Winding Structure for Planar Contactless Battery Charging Platform," in *Industry Applications Conference, 2006. 41st IAS Annual Meeting. Conference Record of the 2006 IEEE*, 2006, pp. 2568-2575.

[19]   G. Elliott, S. Raabe, G. A. Covic, and J. T. Boys, "Multiphase Pickups for Large Lateral Tolerance Contactless Power-Transfer Systems," *Industrial Electronics, IEEE Transactions on,* vol. 57, pp. 1590-1598, 2010.

[20]   S. Boyune, S. Jaegue, C. Sanghoon, S. Seungyong, L. Seokhwan, K. Yangsu, *et al.*, "Design of a pickup with compensation winding for on-line electric vehicle (OLEV)," in *Wireless Power Transfer (WPT), 2013 IEEE*, 2013, pp. 60-62.

[21]   GREENSTARCONCEPTS. (2013). *Dangers with Electric Vehicle Charging Stations*. Available: http://chargingstationsafety.blogspot.com/

[22]   S. Y. Choi, B. W. Gu, S. Y. Jeong, and C. T. Rim, "Advances in Wireless Power Transfer Systems for Roadway-Powered Electric Vehicles," *Emerging and Selected Topics in Power Electronics, IEEE Journal of,* vol. 3, pp. 18-36, 2015.

[23] J. Hai, P. Brazis, M. Tabaddor, and J. Bablo, "Safety considerations of wireless charger for electric vehicles - A review paper," in *Product Compliance Engineering (ISPCE), 2012 IEEE Symposium on*, 2012, pp. 1-6.

[24] W. Chwei-Sen, O. H. Stielau, and G. A. Covic, "Design considerations for a contactless electric vehicle battery charger," *Industrial Electronics, IEEE Transactions on,* vol. 52, pp. 1308-1314, 2005.

[25] M. G. Egan, D. L. O'Sullivan, J. G. Hayes, M. J. Willers, and C. P. Henze, "Power-Factor-Corrected Single-Stage Inductive Charger for Electric Vehicle Batteries," *Industrial Electronics, IEEE Transactions on,* vol. 54, pp. 1217-1226, 2007.

[26] J. Sallan, J. L. Villa, A. Llombart, and J. F. Sanz, "Optimal Design of ICPT Systems Applied to Electric Vehicle Battery Charge," *Industrial Electronics, IEEE Transactions on,* vol. 56, pp. 2140-2149, 2009.

[27] S. Krishnan, S. Bhuyan, V. P. Kumar, W. Wenjiang, J. A. Afif, and L. Khoon Seong, "Frequency agile resonance-based wireless charging system for Electric Vehicles," in *Electric Vehicle Conference (IEVC), 2012 IEEE International*, 2012, pp. 1-4.

[28] J. G. Hayes, M. G. Egan, J. M. D. Murphy, S. E. Schulz, and J. T. Hall, "Wide-load-range resonant converter supplying the SAE J-1773 electric vehicle inductive charging interface," *Industry Applications, IEEE Transactions on,* vol. 35, pp. 884-895, 1999.

[29] C. Rui, Z. Cong, Z. U. Zahid, E. Faraci, Y. Wengsong, L. Jih-Sheng*, et al.*, "Analysis and parameters optimization of a contactless IPT system for EV charger," in *Applied Power Electronics Conference and Exposition (APEC), 2014 Twenty-Ninth Annual IEEE*, 2014, pp. 1654-1661.

[30] Z. Pantic, B. Sanzhong, and S. M. Lukic, "Inductively coupled power transfer for continuously powered electric vehicles," in *Vehicle Power and Propulsion Conference, 2009. VPPC '09. IEEE*, 2009, pp. 1271-1278.

[31] W. Shuo and D. G. Dorrell, "Loss Analysis of Circular Wireless EV Charging Coupler," *Magnetics, IEEE Transactions on,* vol. 50, pp. 1-4, 2014.

[32] Z. Qingwei, W. Lifang, and L. Chenglin, "Compensate Capacitor Optimization for Kilowatt-Level Magnetically Resonant Wireless Charging System," *Industrial Electronics, IEEE Transactions on,* vol. 61, pp. 6758-6768, 2014.

[33] Z. Pantic, K. Lee, and S. Lukic, "Inductive power transfer by means of multiple frequencies in the magnetic link," in *Energy Conversion Congress and Exposition (ECCE), 2013 IEEE*, 2013, pp. 2912-2919.

[34] S. Y. R. Hui and W. W. C. Ho, "A new generation of universal contactless Battery Charging platform for portable Consumer Electronic equipment," *Power Electronics, IEEE Transactions on,* vol. 20, pp. 620-627, 2005.

[35] Z. Cong, C. Baifeng, Z. Lanhua, C. Rui, and L. Jih-Sheng, "Design considerations of LLC resonant converter for contactless laptop charger," in *Applied Power Electronics Conference and Exposition (APEC), 2015 IEEE*, 2015, pp. 3341-3347.

[36] L. Kibok, Z. Pantic, and S. M. Lukic, "Reflexive Field Containment in Dynamic Inductive Power Transfer Systems," *Power Electronics, IEEE Transactions on,* vol. 29, pp. 4592-4602, 2014.

[37] Z. Pantic, B. Sanzhong, and S. Lukic, "ZCS-Compensated Resonant Inverter for Inductive-Power-Transfer Application," *Industrial Electronics, IEEE Transactions on,* vol. 58, pp. 3500-3510, 2011.

[38] G. A. Covic, J. T. Boys, A. M. W. Tam, and J. C. H. Peng, "Self tuning pick-ups for inductive power transfer," in *Power Electronics Specialists Conference, 2008. PESC 2008. IEEE*, 2008, pp. 3489-3494.

[39] W. Chwei-Sen, G. A. Covic, and O. H. Stielau, "Investigating an LCL load resonant inverter for inductive power transfer applications," *Power Electronics, IEEE Transactions on,* vol. 19, pp. 995-1002, 2004.

[40] B. Esteban, M. Sid-Ahmed, and N. C. Kar, "A Comparative Study of Power Supply Architectures in Wireless EV Charging Systems," *Power Electronics, IEEE Transactions on,* vol. 30, pp. 6408-6422, 2015.

[41] M. Al Sakka, J. Van Mierlo, and H. Gualous, "DC/DC Converters for Electric Vehicles," *Electric Vehicles–Modelling and Simulations,* vol. 309, 2011.

[42] N. Mohan and T. M. Undeland, *Power electronics: converters, applications, and design*: John Wiley & Sons, 2007.

[43] C. Woo-Young, Y. Min-Kwon, and C. Hyoung-Sup, "High-Frequency-Link Soft-Switching PWM DC/DC Converter for EV On-Board Battery Chargers," *Power Electronics, IEEE Transactions on,* vol. 29, pp. 4136-4145, 2014.

[44] Z. Pantic and S. M. Lukic, "Framework and Topology for Active Tuning of Parallel Compensated Receivers in Power Transfer Systems," *Power Electronics, IEEE Transactions on,* vol. 27, pp. 4503-4513, 2012.

[45] Z. Pantic, B. Sanzhong, and S. Lukic, "ZCS LCC-Compensated Resonant Inverter for Inductive-Power-Transfer Application," *Industrial Electronics, IEEE Transactions on,* vol. 58, pp. 3500-3510, 2011.

[46] L. Nan and W. Bingnan, "An LLC-based planar wireless power transfer system for multiple devices," in *Applied Power Electronics Conference and Exposition (APEC), 2014 Twenty-Ninth Annual IEEE*, 2014, pp. 3411-3417.

[47] H. Jia, C. Qianhong, W. Siu-Chung, R. Xiaoyong, and R. Xinbo, "Output current characterization of parallel-series/series compensated resonant converter for contactless power transfer," in *Applied Power Electronics Conference and Exposition (APEC), 2015 IEEE*, 2015, pp. 1625-1629.

[48] D. Junjun, L. Fei, L. Weihan, M. Ruiqing, and C. Mi, "ZVS double-side LCC compensated resonant inverter with magnetic integration for electric vehicle wireless charger," in *Applied Power Electronics Conference and Exposition (APEC), 2015 IEEE*, 2015, pp. 1131-1136.

[49] J. W. S. Chaohui Liu, Kalhana Colombage, Chris Gould, Bhaskar Sen, Dave Stone, "Current Ripple Reduction in 4kW LLC Resonant Converter Based Battery Charger for Electric Vehicles," presented at the Energy Conversion Congress and Exposition (ECCE), 2015 IEEE, 2015.

[50] M. Budhia, J. T. Boys, G. A. Covic, and H. Chang-Yu, "Development of a Single-Sided Flux Magnetic Coupler for Electric Vehicle IPT Charging Systems," *Industrial Electronics, IEEE Transactions on,* vol. 60, pp. 318-328, 2013.

[51] J. G. Hayes and M. G. Egan, "A comparative study of phase-shift, frequency, and hybrid control of the series resonant converter supplying the electric vehicle inductive charging interface," in *Applied Power Electronics Conference and Exposition, 1999. APEC '99. Fourteenth Annual*, 1999, pp. 450-457 vol.1.

[52] Z. Wei, W. Siu-Chung, C. K. Tse, and C. Qianhong, "Design for Efficiency Optimization and Voltage Controllability of Series-Series Compensated Inductive Power Transfer Systems," *Power Electronics, IEEE Transactions on,* vol. 29, pp. 191-200, 2014.

[53] I. Nam, R. Dougal, and E. Santi, "Novel control approach to achieving efficient wireless battery charging for portable electronic devices," in *Energy Conversion Congress and Exposition (ECCE), 2012 IEEE*, 2012, pp. 2482-2491.

[54] Z. Chongwen, W. Zhibo, D. Jin, W. Jiande, Z. Sheng, and H. Xiangning, "Active resonance wireless power transfer system using phase shift control strategy," in *Applied Power Electronics Conference and Exposition (APEC), 2014 Twenty-Ninth Annual IEEE*, 2014, pp. 1336-1341.

[55] D. J. Thrimawithana, U. K. Madawala, and M. Neath, "A Synchronization Technique for Bidirectional IPT Systems," *Industrial Electronics, IEEE Transactions on,* vol. 60, pp. 301-309, 2013.

[56] J. G. Meins and J. D. Sinsley, "Method and apparatus for supplying contactless power," ed: Google Patents, 2003.

[57] Z. Cong, M. Hongbo, L. Jih-sheng, and Z. Lanhua, "Design Considerations to Reduce Gap Variation and Misalignment Effects for the Inductive Power Transfer System," *Power Electronics, IEEE Transactions on,* vol. 30, pp. 6108-6119, 2015.

[58] Z. Yiming, L. Ting, Z. Zhengming, H. Fanbo, C. Kainan, and Y. Liqiang, "Selective Wireless Power Transfer to Multiple Loads Using Receivers of Different Resonant Frequencies," *Power Electronics, IEEE Transactions on,* vol. 30, pp. 6001-6005, 2015.

[59] N. Hoang and J. I. Agbinya, "Splitting Frequency Diversity in Wireless Power Transmission," *Power Electronics, IEEE Transactions on,* vol. 30, pp. 6088-6096, 2015.

[60] S. L. Ho, W. Junhua, W. N. Fu, and S. Mingui, "A Comparative Study Between Novel Witricity and Traditional Inductive Magnetic Coupling in Wireless Charging," *Magnetics, IEEE Transactions on,* vol. 47, pp. 1522-1525, 2011.

[61] H. Jia, C. Qianhong, Y. Kaiqin, R. Xiaoyong, W. Siu-Chung, and C. K. Tse, "Analysis and control of S/SP compensation contactless resonant converter with constant voltage gain," in *Energy Conversion Congress and Exposition (ECCE), 2013 IEEE,* 2013, pp. 2552-2558.

[62] D. P. Kar, P. P. Nayak, S. Bhuyan, and S. K. Panda, "Automatic frequency tuning wireless charging system for enhancement of efficiency," *Electronics Letters,* vol. 50, pp. 1868-1870, 2014.

[63] E. Gati, G. Kampitsis, I. Stavropoulos, S. Papathanassiou, and S. Manias, "Wireless Phase - Locked Loop control for inductive Power Transfer Systems," in *Applied Power Electronics Conference and Exposition (APEC), 2015 IEEE,* 2015, pp. 1601-1607.

[64] G. K. Eleni Gati, Ioannis Stavropoulos, Stavros Papathanassiou and Stefanos Manias, "Wireless Phase – Locked Loop Control for Inductive Power Transfer Systems," presented at the Applied Power Electronics Conference and Exposition (APEC), 2015 IEEE, 2015.

[65] G. A. Covic, M. L. G. Kissin, D. Kacprzak, N. Clausen, and H. Hao, "A bipolar primary pad topology for EV stationary charging and highway power by inductive coupling," in *Energy Conversion Congress and Exposition (ECCE), 2011 IEEE,* 2011, pp. 1832-1838.

[66] U. K. Madawala, M. Neath, and D. J. Thrimawithana, "A Power–Frequency Controller for Bidirectional Inductive Power Transfer Systems," *Industrial Electronics, IEEE Transactions on,* vol. 60, pp. 310-317, 2013.

[67] Z. Biao, S. Qiang, L. Wenhua, and S. Yandong, "Overview of Dual-Active-Bridge Isolated Bidirectional DC-DC Converter for High-Frequency-Link Power-Conversion System," *Power Electronics, IEEE Transactions on,* vol. 29, pp. 4091-4106, 2014.

[68] O. C. Onar, J. M. Miller, S. L. Campbell, C. Coomer, C. P. White, and L. E. Seiber, "Oak Ridge National Laboratory Wireless Power Transfer Development

for Sustainable Campus Initiative," in *Transportation Electrification Conference and Expo (ITEC), 2013 IEEE*, 2013, pp. 1-8.

[69] L. Jun-Young and H. Byung-Moon, "A Bidirectional Wireless Power Transfer EV Charger Using Self-Resonant PWM," *Power Electronics, IEEE Transactions on,* vol. 30, pp. 1784-1787, 2015.

[70] Q. Phu Ho Van, H. Thanh Tien, and L. Jong-Wook, "A Fully Integrated Multimode Wireless Power Charger IC With Adaptive Supply Control and Built-In Resistance Compensation," *Industrial Electronics, IEEE Transactions on,* vol. 62, pp. 1251-1261, 2015.

[71] S. Aldhaher, P. C. K. Luk, and J. F. Whidborne, "Electronic Tuning of Misaligned Coils in Wireless Power Transfer Systems," *Power Electronics, IEEE Transactions on,* vol. 29, pp. 5975-5982, 2014.

[72] S. Ping, A. P. Hu, S. Malpas, and D. Budgett, "Switching Frequency Analysis of Dynamically Detuned ICPT Power Pick-ups," in *Power System Technology, 2006. PowerCon 2006. International Conference on*, 2006, pp. 1-8.

[73] K. Kobayashi, N. Yoshida, Y. Kamiya, Y. Daisho, and S. Takahashi, "Development of a non-contact rapid charging inductive power supply system for electric-driven vehicles," in *Vehicle Power and Propulsion Conference (VPPC), 2010 IEEE*, 2010, pp. 1-6.

[74] L. Sungwoo, H. Jin, P. Changbyung, C. Nam-Sup, C. Gyu-Hyeoung, and R. Chun-Taek, "On-Line Electric Vehicle using inductive power transfer system," in *Energy Conversion Congress and Exposition (ECCE), 2010 IEEE*, 2010, pp. 1598-1601.

[75] N. Liu and T. G. Habetler, "Design of a universal inductive charger for electric vehicles," in *Transportation Electrification Conference and Expo (ITEC), 2014 IEEE*, 2014, pp. 1-6.

[76] W. Junhua, S. L. Ho, W. N. Fu, and S. Mingui, "Analytical Design Study of a Novel Witricity Charger With Lateral and Angular Misalignments for Efficient Wireless Energy Transmission," *Magnetics, IEEE Transactions on,* vol. 47, pp. 2616-2619, 2011.

[77] D. Kurschner, C. Rathge, and U. Jumar, "Design Methodology for High Efficient Inductive Power Transfer Systems With High Coil Positioning Flexibility," *Industrial Electronics, IEEE Transactions on,* vol. 60, pp. 372-381, 2013.

[78] S. Y. Choi, S. Y. Jeong, E. S. Lee, B. W. Gu, S. W. Lee, and C. T. Rim, "Generalized Models on Self-Decoupled Dual Pick-up Coils for Large Lateral Tolerance," *Power Electronics, IEEE Transactions on,* vol. 30, pp. 6434-6445, 2015.

[79] P. Chan-Bae, L. Byung-Song, and L. Hyung-Woo, "Magnetic and thermal characteristics analysis of inductive power transfer module for railway applications," in *Vehicle Power and Propulsion Conference (VPPC), 2012 IEEE*, 2012, pp. 576-579.

[80] S. Y. Choi, J. Huh, W. Y. Lee, and C. T. Rim, "Asymmetric Coil Sets for Wireless Stationary EV Chargers With Large Lateral Tolerance by Dominant Field Analysis," *Power Electronics, IEEE Transactions on,* vol. 29, pp. 6406-6420, 2014.

[81] R. Bosshard, J. W. Kolar, J. Muehlethaler, I. Stevanovic, B. Wunsch, and F. Canales, "Modeling and η-α-Pareto Optimization of Inductive Power Transfer Coils for Electric Vehicles," *Emerging and Selected Topics in Power Electronics, IEEE Journal of,* vol. PP, pp. 1-1, 2014.

[82] J. M. Miller, P. T. Jones, L. Jan-Mou, and O. C. Onar, "ORNL Experience and Challenges Facing Dynamic Wireless Power Charging of EV's," *Circuits and Systems Magazine, IEEE,* vol. 15, pp. 40-53, 2015.

[83] O. C. Onar, J. M. Miller, S. L. Campbell, C. Coomer, C. P. White, and L. E. Seiber, "A novel wireless power transfer for in-motion EV/PHEV charging," in *Applied Power Electronics Conference and Exposition (APEC), 2013 Twenty-Eighth Annual IEEE*, 2013, pp. 3073-3080.

[84] G. A. Covic, J. T. Boys, M. L. G. Kissin, and H. G. Lu, "A Three-Phase Inductive Power Transfer System for Roadway-Powered Vehicles," *Industrial Electronics, IEEE Transactions on,* vol. 54, pp. 3370-3378, 2007.

[85] Z. Wei, J. C. White, A. M. Abraham, and C. C. Mi, "Loosely Coupled Transformer Structure and Interoperability Study for EV Wireless Charging Systems," *Power Electronics, IEEE Transactions on,* vol. 30, pp. 6356-6367, 2015.

[86] L. Jia-You, S. Hung-Yu, and L. Kun-Wei, "Design and implementation of weaving-type pad for contactless EV inductive charging system," *Power Electronics, IET,* vol. 7, pp. 2533-2542, 2014.

[87] A. Zaheer, D. Kacprzak, and G. A. Covic, "A bipolar receiver pad in a lumped IPT system for electric vehicle charging applications," in *Energy Conversion Congress and Exposition (ECCE), 2012 IEEE*, 2012, pp. 283-290.

[88] D. W. Baarman, S. T. Eurich, W. T. Stoner, J. B. Taylor, R. J. Weber, J. J. Lord*, et al.*, "Inductive charging system for electric vehicle," ed: Google Patents, 2015.

[89] C. Joffe, S. Ditze, and A. Rosskopf, "A novel positioning tolerant inductive power transfer system," in *Electric Drives Production Conference (EDPC), 2013 3rd International*, 2013, pp. 1-7.

[90]   M. Rawson and S. Kateley, "Electric vehicle charging equipment design and health and safety codes," SAE Technical Paper1999.

[91]   S. International, "SAE's J1772 'combo connector' for ac and dc charging advances with IEEE's help," *[Online]. Available: http://ev.sae.org/article/10128, Sep. 8, 2011.*

[92]   T. Motors, "Tesla roadster spec sheet," 2009.

[93]   W. Haoyu, S. Dusmez, and A. Khaligh, "Design considerations for a level-2 on-board PEV charger based on interleaved boost PFC and LLC resonant converters," in *Transportation Electrification Conference and Expo (ITEC), 2013 IEEE*, 2013, pp. 1-8.

[94]   P. C. K. Luk and S. Aldhaher, "Analysis and design of a Class D rectifier for a Class E driven wireless power transfer system," in *Energy Conversion Congress and Exposition (ECCE), 2014 IEEE*, 2014, pp. 851-857.

[95]   K. Minho, A. Seungyoung, and K. Hongseok, "Magnetic design of a three-phase wireless power transfer system for EMF reduction," in *Wireless Power Transfer Conference (WPTC), 2014 IEEE*, 2014, pp. 17-20.

[96]   S. Chiuk, K. Hongseok, D. H. Jung, K. Yoon, C. Yeonje, K. Sunkyu*, et al.*, "Three-phase magnetic field design for low EMI and EMF automated resonant wireless power transfer charger for UAV," in *Wireless Power Transfer Conference (WPTC), 2015 IEEE*, 2015, pp. 1-4.

[97]   R. Arnold and P. Gratzfeld, "Automatic tuning concept for a three-phase inductive power transfer system," in *Electric Drives Production Conference (EDPC), 2014 4th International*, 2014, pp. 1-7.

[98]   R. Arnold and P. Gratzfeld, "Modeling of a three-phase inductive power transfer system in phasor domain for fast simulation," in *Electric Drives Production Conference (EDPC), 2013 3rd International*, 2013, pp. 1-6.

[99]   S. Abdel-Rahman, "CCM PFC Boost Converter Design," 2013.

[100]   L. Balogh, "Design and application guide for high speed MOSFET gate drive circuits," 2001.

[101]   M. Pahlevaninezhad, J. Drobnik, P. K. Jain, and A. Bakhshai, "A Load Adaptive Control Approach for a Zero-Voltage-Switching DC/DC Converter Used for Electric Vehicles," *Industrial Electronics, IEEE Transactions on,* vol. 59, pp. 920-933, 2012.

[102]   Rohm, "SiC Application Note: SiC Power Devices " 2014.

[103]   J. Tritschler, S. Reichert, and B. Goeldi, "A practical investigation of a high power, bidirectional charging system for electric vehicles," in *Power Electronics*

and Applications (EPE'14-ECCE Europe), 2014 16th European Conference on, 2014, pp. 1-7.

[104] A. Rosskopf, E. Bar, and C. Joffe, "Influence of Inner Skin- and Proximity Effects on Conduction in Litz Wires," *Power Electronics, IEEE Transactions on,* vol. 29, pp. 5454-5461, 2014.

[105] S. Wang and D. Dorrell, "Copper Loss Analysis of EV Charging Coupler," *Magnetics, IEEE Transactions on,* vol. PP, pp. 1-1, 2015.

[106] B. Yang, F. C. Lee, A. J. Zhang, and G. Huang, "LLC resonant converter for front end DC/DC conversion," in *Applied Power Electronics Conference and Exposition, 2002. APEC 2002. Seventeenth Annual IEEE*, 2002, pp. 1108-1112.

[107] N. S. Bayindir, O. Kukrer, and M. Yakup, "DSP-based PLL-controlled 50-100 kHz 20 kW high-frequency induction heating system for surface hardening and welding applications," *Electric Power Applications, IEE Proceedings -,* vol. 150, pp. 365-371, 2003.

[108] D. Xiaoming and A. Q. Huang, "Current-mode variable-frequency control architecture for high-current low-voltage DC-DC converters," *Power Electronics, IEEE Transactions on,* vol. 21, pp. 1133-1137, 2006.

[109] F. Semiconductor, "Induction Heating System Topology Review," 2000.

[110] R. Beiranvand, B. Rashidian, M. R. Zolghadri, and S. M. H. Alavi, "Using LLC Resonant Converter for Designing Wide-Range Voltage Source," *Industrial Electronics, IEEE Transactions on,* vol. 58, pp. 1746-1756, 2011.

[111] H. M. Greenhouse, "Design of Planar Rectangular Microelectronic Inductors," *Parts, Hybrids, and Packaging, IEEE Transactions on,* vol. 10, pp. 101-109, 1974.

[112] A. Zaheer, H. Hao, G. A. Covic, and D. Kacprzak, "Investigation of Multiple Decoupled Coil Primary Pad Topologies in Lumped IPT Systems for Interoperable Electric Vehicle Charging," *Power Electronics, IEEE Transactions on,* vol. 30, pp. 1937-1955, 2015.

[113] S. Raju, W. Rongxiang, C. Mansun, and C. P. Yue, "Modeling of Mutual Coupling Between Planar Inductors in Wireless Power Applications," *Power Electronics, IEEE Transactions on,* vol. 29, pp. 481-490, 2014.

[114] K. Colak, M. Bojarski, E. Asa, and D. Czarkowski, "A constant resistance analysis and control of cascaded buck and boost converter for wireless EV chargers," in *Applied Power Electronics Conference and Exposition (APEC), 2015 IEEE*, 2015, pp. 3157-3161.

[115] N. A. Keeling, G. A. Covic, and J. T. Boys, "A Unity-Power-Factor IPT Pickup for High-Power Applications," *Industrial Electronics, IEEE Transactions on,* vol. 57, pp. 744-751, 2010.

[116] R. Haldi, K. Schenk, I. Nam, and E. Santi, "Finite-element-simulation-assisted optimized design of an asymmetrical high-power inductive coupler with a large air gap for EV charging," in *Energy Conversion Congress and Exposition (ECCE), 2013 IEEE,* 2013, pp. 3635-3642.

[117] J. Seungmin, J. Young Jae, and K. Dongsuk, "Economic Analysis of the Dynamic Charging Electric Vehicle," *Power Electronics, IEEE Transactions on,* vol. 30, pp. 6368-6377, 2015.

VITA

Nan Liu was born in Tianjin, China in 1989. He obtained his Bachelor's Degree in Electrical Engineering from Zhejiang University in Hangzhou, China in 2011. He then joined Georgia Institute of Technology in Atlanta, GA, USA in August 2011. He originally studied for his Master's Degree in Electrical Engineering, and began working towards his Ph.D. degree in January 2012.

Since January 2012, Nan has been with ECE Power group, where he is currently a Ph.D. candidate and completing the Ph.D. degree in electrical engineering. After he joined ECE Power group, Nan has been a graduate research assistant working on inductive charging and on-board charging of electric vehicles. During his study at Georgia Tech, he worked as teaching assistant of various undergraduate and graduate classes, in power electronics, machine drive, and fundamental electrical principles. In summer 2012, he worked as an internship in the load identification used in smart building, at Eaton Corporation Innovation Center, Milwaukee. In summer 2013, he worked as an R&D internship in wireless charging of portable electronic devices, at Mitsubishi Electric Research Labs, Boston. In summer 2015, he worked as an R&D internship at Apple, Inc.

Nan Liu is an IEEE student member since 2010. He has authored two IEEE Transactions papers, and five IEEE conference papers.